Synthesis and characterization of Titanium Nitride Nanowires for neural-electrode coatings for improving electrode/neuron interface in the brain

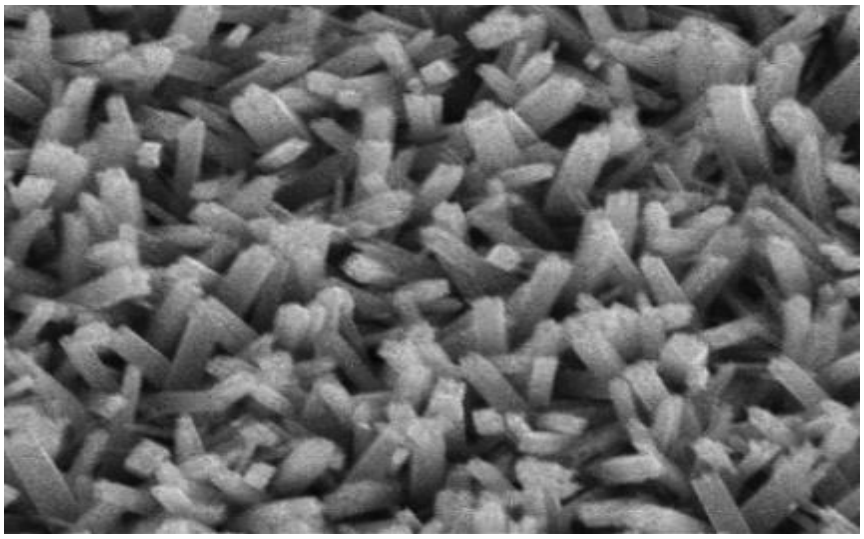

ROAA ADNAN SAIT

June 2019

THESIS SUBMITTED TO DE MONTRORT UNIVERISTY IN THE PARTIAL FULFILMENT OF THE REQUIREMENT FOR THE DEGREE OF

DOCTOR OF PHILOSOPHY

Emerging Technologies Research Centre. School of Engineering and Sustainable Development, De Montfort University, The Gateway, Leicester, United Kingdom, LE1 9BH

Synthesis and characterization of Titanium Nitride Nanowires as a neural-electrode material for improving electrode/neuron interface in the brain

Roaa Adnan Sait

June 2019

PhD supervisors:

Dr. Richard Cross – 1st supervisor

Dr. Yong Sun – 2nd supervisor

Dr. Sridhar Govindarajan – 3rd supervisor

Publications:

(1) Synthesis and characterization of sputtered titanium nitride as a nucleation layer for novel neural electrode coatings.

(2) Nitridation of optimised TiO_2 nanorods through PECVD towards neural electrode application.

Oral presentations:

(1) Synthesis and characterisation of TiN-NWs towards neural electrode application. *Asian Pacific Nano Congress 2017 / World Congress on Nanoscience and Nanotechnology*. Dubai, UAE. Oct/2017

(2) Synthesis and characterization of titanium nitride nanowires for neural electrode coatings for improving electrode/neurons interface. *The 11th International Conference on Physics of Advanced Materials.* Cluj-Napoca. Sep/2016.

Declaration

I declare that this thesis is a presentation of my original research work for a research degree at De Montfort university and it has not been submitted to any other institution. Furthermore, I ensure that the work is original, and, to the best of my knowledge, does not break copyright law, and has not been taken from other sources except where such work has been cited and acknowledged within the text. The thesis is based on work done by myself and jointly with other's contribution; wherever contributions of others are involved, every effort is made to indicate this clearly. And so I declare that I have acknowledged all main sources of help. I confirm that part of this work have been published and it is mentioned where applicable.

Acknowledgment

I would like to express my deep gratitude to my mother without whom I would not got this scholarship opportunity and conduct this research. She has provided all the comfort environment I needed to finish this piece of work.

I would like to offer my special thanks to my supervisor Dr. Richard Cross for his great support and valuable constructive suggestions throughout the project. His positive and encouraging words at the time of struggle has helped me to move forward. My grateful thanks are also extended to Dr. Yong and Sridhar for proving the cyclic voltammetry tool. A great thanks to Dr. Sridhar for his patient guidance in CV and impedance analysis.

I would like to thank the following people for their contribution with the collection of my data:

Dr. Ahmed Al Zhrani at Nanotechnology and Research Centre - King AbdulAziz University.

Dr. Deema Husain at Neurooncology Translational Group, King Fahd Medical Research Center (KFMRC)- King Abdulaziz University.

Dr. Mohamed Nejib Hedhili at Nanotechnology Core Lab - King Abdullah University of Science and Technology.

Finally, thanks to my small family; my father and my three youngest brothers for standing by my side during this hard working period. My friends and colleagues for cheering me up at the hard times.

Glossary

Term	Definition
Action potentials	A rapid rise and subsequent fall in membrane potential across the intercellular and extracellular space. Sufficient current is required to initiate a voltage response in a cell membrane; if the current is insufficient to depolarize the membrane to the threshold level, an action potential will not fire.
Anomalous diffusion	is a type of ion diffusion towards the interface when the electrode exhibits rough or porous surface.
Backscattered electron	is generated when electrons undergo large-angle elastic collisions, leaving the sample with the same energy as the incident electrons
Binding energy	is the energy required to free electrons from their atomic orbits.
Biocompatibility	The property of a material being compatible with living tissue in which it should not be toxic to the cells, or corrode with time and it should function what it supposed to do
Cell viability	The ability of cells to survive and grow.
Charge injection	The amount of charges, e.g ions such as potassium and sodium, that can be delivered to the tissue to cause action potential.
Depolarisation	is when the membrane potential becomes less negative with respect to the extracellular space (more positive), opening ion channels and allowing ions flux into the membrane, hence depolarisation of the membrane and propagation of action potential.

Diffusion layer	is the region in which the concentration of ions are different from that in the bulk solution where it becomes closer to the bulk value as distance increase from the interface.
Double layer	Consists of two layers, one at the electrode interface and the other at the electrolyte interface having an opposite polarity to that on the electrode
Electrolysis of water	is the decomposition of water into oxygen and hydrogen gas due to the passage of an electric current.
Finite diffusion	Applies at a situation where the diffusion is confined between the electrode (x = 0) and a boundary at x = l.
Free radicals	are produced when a free electron interacts with a molecule, breaking its chemical bond, or when thermal energy cause the separation of molecules into its elements. Those elements are highly active and prone to make chemical bonds to reduce its energy.
Hyperpolarisation	Due to the slow kinetics of deactivating K^+ ions channels, the membrane potential can be driven to a value more negative than its rest potential, this is hyperpolarisation, before returning to its rest state.
Mechanical mismatch	refers to the stiffness between the metal electrode and the tissues it interfaces with. Young module is a measure of stiffness of a material. The electrode material should exhibit young module that is close to that of the tissue to reduce the mechanical mismatch.
Neurophysiology	A neuroscience that is concerned with the study of the functioning of the nervous system.

Polarisation of an electrode	when an electrode is driven away from its potential is it said to be polarised.
Polycrystalline material	a material consisting of many crystalline parts that are randomly oriented with respect to each other.
Refractory period	is the period when the membrane tries to rebalance the ionic charges across the intercellular and extracellular space to reach the resting potential again after the firing of action potential.
Secondary electron	is produced when the primary electron beam interacts with the nuclei of the specimen losing energy to a loosely bounded electrons causing ejection from the sample atoms (ionisation).
Seed layer	A seed layer is used for nucleation process to induce preferential direction growth.
Semi-infinite diffusion	Semi-infinite diffusion applies at a situation where no oscillations of concentrations of chemical species or concentrations of ions are not affecting the electrode surface
Stoichiometry	The ratio of two elements or more in a unit cell.
Water window	is the potential region, between two potential limits, where no electrolysis of water or irreversible reaction occur.

Table of Contents

List of figures

Abstract

In neurophysiological measurements, a neural-electrode interface material plays a critical role in delivering adequate charge to elicit action potentials without damaging the tissue of interest. However, the need to minimise electrode dimensions to reduce invasiveness and increase selectivity, demands the use of materials that are able to handle larger current and charge densities than traditional noble electrodes such as platinum. Since charge density is directly affected by the surface area of the electrode, nanoscale materials have shown a great deal of potential for not just improving the electrochemical properties, but the biocompatibility at reduced electrode dimensions.

Titanium Nitride thin film (TiN) has been implemented previously in neural-electrode application due to its apposite properties. The work described here is aimed towards the synthesis of a novel TiN Nanowire interface (TiN-NW) as a potential neural-electrode material. The synthesis of the nanowires involved a three-step approach: (1) sputter of TiN thin film onto a substrate to act as a seed layer for the growth of NWs, (2) the growth of titanium dioxide nanowires (TiO_2-NWs) of high aspect ratio and crystallinity followed by (3) a novel plasma nitridation step using Plasma Enhanced Chemical Vapour Deposition (PECVD) which offered a lower synthesis temperature than the conventional processing temperature reported in the literature.

An optimised TiN thin film, grown through Radio Frequency (RF) non-reactive magnetron sputtering, was used as a seeding layer for the growth of NWs. The properties of the seed layer and the grown NWs were studied by scanning electron microscopy (SEM), atomic force microscopy (AFM), X-Ray diffraction (XRD), Raman spectroscopy, X-Ray photoelectron spectroscopy (XPS), and transmission electron microscopy (TEM) while the suitability of the grown TiN-NWs as an electrode material was tested by studying their electrochemical performance through cyclic voltammetry (CV) and electrochemical impedance spectroscopy (EIS). In addition, the biocompatibility of both structures were tested by culturing glioblastoma cells (GBM) *in vitro,* and cell viability and behaviour were studied and compared to that on TiN thin film.

XPS and TEM results showed that TiO_2-NWs were converted to TiN-NWs at a temperature of 600 °C. Electrochemical results showed 5-fold of capacitance enhancement of the synthesised TiN-NWs as compared to that of the optimised TiN film. Additionally, TiN-NWs have shown greater cyclic stability, with capacitance retention of almost 99%, and lowered susceptibility to oxidation compared to TiN thin films. The impedance of TiN-NWs electrode at low frequencies, corresponding to ion diffusion, was noticeably lower than that of the film electrode. The *in vitro* test showed that cells were viable and attached to both structures and the cells on NWs formed dense 3D structures and had a greater spatial distribution than those cultured on the thin film layer. These findings not only highlighted the potential use of TiN-NWs as a neural-electrode interface material but also suggested a way of reducing the nitridation temperature to obtain TiN through PECVD process, which can improve existing electrodes or be integrated into next-generation neural-electrode structures.

Chapter 1. Introduction

1.1 Motivation for undertaking the work

In a healthy functional neural system, the electrical signals' pathway that neurons propagate are usually intact, however, in a traumatised system, this flow of signals or information is broken at some point causing neurological disorder, such as epilepsy, Alzheimer's, Parkinson's disease, dystonia and stroke [1] [2]. Electrical stimulation of nerve tissue and recording of neural electrical activity using implantable electrodes have been proposed to address such medical conditions. The electrodes' objective is to create a link between the outside world and the nervous system by injecting electrical signal into neurons to stimulate or record from neural tissue to improve our understanding of the nervous system and be able to assist those people with neurological disabilities [3]. Since neural-electrodes serve as a critical interface with body tissue and are used for long-term implants, they are preferred to be smaller in size to minimise tissue trauma/invasiveness and, most importantly, to increase selectivity (recording individual neurons), i.e. the ability of the electrode to activate a small population of neurons without causing excitation outside the area of study [1].

Ideally, such devices should be biocompatible to the tissue environment and be able to chronically interface safely as well as facilitate high levels of charge injection within a safe limit to elicit action potential [4]. Existing neural-electrodes use conventional interface materials such as platinum (Pt) [5], gold [6] and iridium oxide (IrOx) [7]. Pt is preferable over other metals because of its electrochemical stability, oxidation resistance and its high biocompatibility [4]. However, with the need to reduce the dimensions of conventional electrodes, their electrochemical, mechanical performance and biocompatibility become limited, preventing their applications [4]. The reduced surface area limits the transfer of charge for recording application, and hence reduces the charge injection to the tissue needed for stimulation [4]. In addition, decreasing the size of electrodes increases impedance and the charge density per unit area, which can damage the electrode and the tissues prior to reaching the threshold required to elicit action potential [1]. Moreover, it has been shown that the reduced surface area, due to the reduced dimension of the electrode, might not enhance neural tissue integration due to reduced contact adhesion, which consequently allow the immune cells to access the interface causing a loss of recording or stimulation of the targeted tissues [7, 4].

To enhance the efficiency of a neural-electrode interface, while keeping the electrode dimensions small, the geometrical surface area of the electrode can be increased. There are three methods by which the geometrical surface area can be modified;

(1) Roughening the surface by altering the existing metallic surface and creating a defined microstructure on the electrode surface using methods such as sputter etching, reactive ion etching, laser ablation or focused ion beam [8].

(2) Thin film surface coating of organic materials such as conductive polymers and hydrogels, or inorganic materials such as platinum black, IrOx and TiN films [9]. The coating techniques of these materials were accomplished using composite electrodeposition [10], DC reactive sputtering [7] and DC reactive magnetron sputtering [11] respectively;

(3) Surface coating of nanostructured materials on the electrode surface [12, 13].

This last option holds enormous promise for developing enhanced electrode/neuron interfaces and increasing activity in this area has been reported in the literature [14, 4]. Nanostructured materials such as nanostructured Pt-coating [12], IrOx nanowires [15], Carbon nanotubes (CNTs) [16] and 3,4-ethyleneddioxythiophene (PEDOT) nanotubes [6] have been investigated previously as interface materials. The nanostructured Pt reported by Boehler, C [12] showed a reduction in the electrode impedance by two orders of magnitude compared to its thin form. In addition, an increase in charge injection limit from 0.05 to 0.4 mC/cm^2 was found. The improved electrochemical properties is owed to the increased in surface area, thus facilitating increased charge transfer and a reduction in the impedance of the electrodes [12, 16, 6]. Moreover, having nanostructured material coated on the electrode, such as nanowires or nanotubes, can enhance the mechanical properties of the electrode by reducing the stress at the cellular interface [4]. This is due to the fact that long nanowires/nanotubes have a degree of flexibility which can undertake deformation, facilitating a better tethering to the tissues [1]. These improvements are considered key components for safe stimulation and recording over a long period of time. The safe stimulation and recording of neurons is demonstrated when there is no irreversible reactions, such as electrolysis of water taking place at the interface. If the charge injection through the interface material is sustained between two voltage limits, called the water window, no electrolysis of water can occur. However, beyond this electrochemical restrain, tissues around the electrode can be harmed and the electrode can degrade in function and corrode over time [4].

In this study, we report the synthesis and characterisation of TiN-NWs through nitridation of optimised TiO_2-NWs in PECVD offering lower synthesis temperature as compared to conventional methods [17, 18, 19, 20, 21]. TiN-NWs are suggested here as an alternative material with controllable morphology and structural properties to enhance the electrochemical behaviour and biocompatibility towards their usage, for the first time, as a neural-electrode interface material. Thin film TiN has a comparable charge injection limit (0.04 - 4.66 mC/cm^2) [22, 23] to that of IrOx (5 mC/cm^2) [7], and higher than the nanostructured Pt reported by Boehler, C [12]. TiN has served as a coating for several decades in a variety of areas and has been regarded as a potential material for application in dental prosthesis [24], hip joint replacement [25], microelectrodes for biosensors [26], supercapacitors [27] and neural-electrodes for stimulation and recording [11]. Focus has been placed on TiN due to its chemical, mechanical and electrical properties, such as excellent chemical stability, good corrosion resistance, low friction coefficient (~0.4), good electrical conductivity (p=21.7 mΩ cm) and high melting temperature (2,927 °C) [4]. When compared to bulk TiN, TiN nanostructures/roughness at the nanoscale provides increased surface area which may offer a larger number of active sites, leading to more charge densities being delivered to the tissue, consequently not just enhancing the electrochemical, but mechanical and biocompatible properties as well, making such structure an attractive interface in the neural-technologies [1, 28].

1.2 Research Aim and objectives

The work is aimed at growing TiN-NWs through a novel approach to be used as a potential electrode interface material. In addition, the work is aimed at improving the material properties by synthesising controlled morphology, structural and electrochemical properties to enhance functionality as an electrode material and so to increase its life time (stability).

The synthesis involves a two-step methods; **(1)** *hydrothermal growth of TiO_2-NWs*, from an optimised TiN sputtered layer deposited, for the first time, by non-reactive RF sputtering which offers a simpler approach by only optimising RF power and Ar flow rate, **(2)** *a novel nitridation process in PECVD* at lower temperature (600°C) that has not been reported to date.

Since the TiN seed layer would be part of the stimulus path between the electrode and nanowires, its structural and electrochemical properties was optimised. Firstly, the sputtering parameters of RF power and Argon (Ar) flow rate were varied in order to investigate their effects on the structural and electrochemical properties of deposited TiN films. The structural and electrochemical properties were investigated by SEM, XRD, AFM and CV. Secondly, the grown TiO_2-NWs have been optimised towards having relatively high aspect ratio and polycrystalline structure by controlling the nucleation layer thickness, growth temperature and time. The effects of the hydrothermal growth parameters on the properties of the TiO_2-NWs were investigated using SEM and XRD for morphological and structural studies respectively. Thirdly, nitridation parameters, such as the applied power, chamber pressure and nitridation time were optimised towards effective nitridation. The nitrided nanowires were characterised by SEM and XRD to observe any changes in morphology and structural properties. Raman, XPS and TEM were conducted to analyse their composition. To test the material suitability as an electrode interface material, electrochemical properties were studied using CV and EIS. Finally, *in vitro* cell culture was utilised with TiN-NWs as well as TiN thin films to compare and contrast their biocompatibility.

Chapter outlines:

Chapter 1 provides the motivation to undertake this work and the contribution to the field of material science and neural interfaces. In addition, it states the research aim and objectives.

Chapter 2 reviews the theory behind the working principle of electrical stimulation of neurons and the electrochemical process occurring between the electrode and electrolyte interface. It explains the challenges in developing a chronical neural-electrode interface material and the main criteria that neural-electrode materials must meet. It also highlights the potential capability of nanostructured materials to improve the neural-electrode interface.

Chapter 3 explains the fabrication methods used to synthesis TiN-NWs which includes: sputtering, hydrothermal solution growth and plasma enhanced chemical vapour deposition. In addition, the chapter reports the various characterisation tools used to investigate structural and electrothermal properties of the materials.

Chapter 4 reports the synthesis of the TiN nucleation layer and the optimisation of the sputtering parameters. This is followed by extended analysis of the material properties to investigate its suitability as a nucleation layer for the growth of nanowires as well as its suitability as a potential neural-electrode material.

Chapter 5 reports the synthesis of TiN nanowires and the process of optimising the growth conditions and the nitridation process towards obtaining high aspect ratio, polycrystalline structure and their subsequent nitridation. The optimisation is supported by compositional, structural and electrochemical analyses.

Chapter 6 compares and contrasts the biocompatibility of the TiN film and TiN-NWs by culturing Glioblastoma (GBM) cells onto the substrates and test their viability, adherence and behaviour.

Chapter 7 summarieses the main outcomes from this work and suggests future opportunities for exploration and development.

Chapter 2. Background theory

2.1 Introduction

Implanted electrodes are considered life-sustaining devices since they are the foundations of emerging protheses and treatments for spinal cord injury, stroke, cortical visual protheses, epilepsy, Parkinson's disease (PD) and other neurological disorders [29]. In recent years, neurotechnology has experienced exponential growth towards the design of electrode devices that chronically interface directly with neural tissue for recording and/or stimulation. In demonstrating long-term performance, electrodes have found application in cardiac pacemaker electrodes [30], cochlear implants [31] and deep brain stimulators (DBS) [32]. However, more advanced neural interface devices require higher resolution for single unit recording and selected stimulated neurons still face significant challenges in reliability and long-term performance [33]. The most significant challenge lies in optimising the properties of the electrode material that is brought into contact with biological neural tissue while electrical pulses are continuously and chronically applied across the interface. While many other stimulation devices exist to treat neurological disorders, these neurostimulation devices have shown some success, but they are still unable to restore natural function in all patients. In fact, some neural-electrode devices have shown failure after chronic implantation ranging from weeks to months to a few years [34, 35, 36]. The main causes of such failure have been attributed to the poor material mechanical properties, corrosion, surface structural change, development of unstable films, and metal ion dissolution into the nearby environments, eventually causing toxicity to the biological environment and so failure of the device.

In order to understand the functional limitations of those stimulator electrodes, it is important to first appreciate the basic principles behind electrical signals in neurons and how electrical stimulations induce activation of neurons. It is essential to examine the basic electrochemical mechanism of charge transfer and charge storage occurring between electrode/electrolyte interface. In addition, TiN mechanical, electrochemical and structural properties are discussed. Thus, this chapter lays out the current knowledge of these areas. Further moreover, the chapter highlights some of the previous work on potential neural-electrode materials and discusses the current limitation of some interface materials and the main criteria that an ideal interface material should exhibit; for example, low mechanical mismatch, high charge injection/capacitance and low impedance. This chapter also highlights the potential for using nanostructured surfaces as an interface material to overcome some of the above limitations.

2.1.1 Principles of electrical signals in neurons

Within a single neuron, information is transmitted via electrochemical signaling. When a neuron is stimulated an electrical impulse propagates down the neuron's axon to its neighboring neurons, this is the so called *action potential*. Action potential results from the flow of ions across the neuronal cell membrane. Neurons, like all cells, have a *resting membrane potential* of the order of -60 to -95 mV, depending on the cell type [1]. This electrical potential across the cell membrane is due to the distribution of positively-charged potassium ions (K^+) in the intercellular space and positively-charged sodium ions (Na^+) in the extracellular space of the cell [37]. The fact that there are relatively more Na^+ ions outside the cell and more K^+ ions inside the cell, this makes the membrane potential more negative inside than outside the cell. The cell always maintain this distribution of atoms by pumping out $Na^+$and pumping in K^+ through ion channels in response to any change of membrane potential. If the membrane has a negative potential it is said to be *polarised* [37].

When neurotransmitters enter the receptor site, ion channels open and Na^+ ions rush into the cell, making the intercellular less negative relative to the extracellular space. When enough ions flow into the cell, passing the threshold of around -50 mV, many Na^+ ions channel open allowing further influx of Na^+ ions which depolarise adjacent channels [37]. If sufficient Na^+ ion channels were activated then the spike of action potential is generated, *depolarisation* of the cell. After sending this signal along the axon, Na^+ ions channel quickly inactivate and block inward sodium ions flow. The K^+ ions channel then open to send K^+ ions to the extracellular space to attempt to rebalance the charges, *refractory period* [37]. The refractory period usually last on the order of 1 ms. Due to the slow kinetics of deactivating K^+ ions channels, the membrane potential can be driven to a value more negative than its rest potential, this is *hyperpolarisation,* before returning to its rest state. Action potential is said to be "all-or-one" phenomena since the amplitude and duration of the action potential is independent of the stimuli. Figure 2.1 illustrates the change in the membrane potential during an action potential [37].

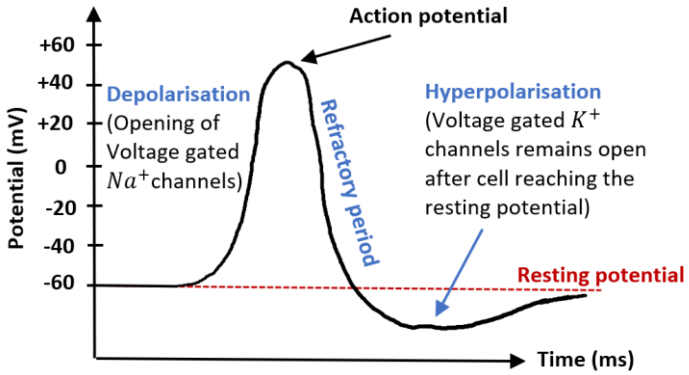

Figure 2.1: Stimulation of an axon results in changes in sodium and potassium ions following action potential then hyperpolarization (Adapted from [37]).

2.1.2 Principles of electrical stimulation of neurons

In order to artificially generate neural activity using electrical stimulations, electrodes should be able to deliver an adequate amount of charge through cathodic (negative) and anodic (positive) current pulses. Cathodic electrical stimulation is used to produce action potentials to induce a specific function in an impaired neurons. Similarly, the goal of anodic stimulation is to inhibit unwanted neural activity by hyperpolarisation of targeted neurons [1]. Therefore, electrical stimulation is accomplished by placing a stimulation electrode near the targeted tissues and deliver adequate charges to elicit action potential.

During cathodal stimulation, negative charges flow into the cell, making the extracellular space around the cell and near the electrode more negative as compared to the intercellular space of the cell, hence altering the potential across the membrane [1], see Figure 2.2**.** In fact, the potential across the membrane decreases (e.g. -70 to -55 eV), or in other word, making the intracellular space less negative than the outside. This causes Na^+ ions channels to open (as they usually open at potential value of -55 eV), and if enough flux is flowing into the cell, further channels are open leading to depolarisation of the cell membrane. Similarly, in anodic stimulation, positive charges flow into the cell making the extracellular space more positive as compared to the rest state of the membrane, resulting in hyperpolarisation and blockage of action potential [1]**.**

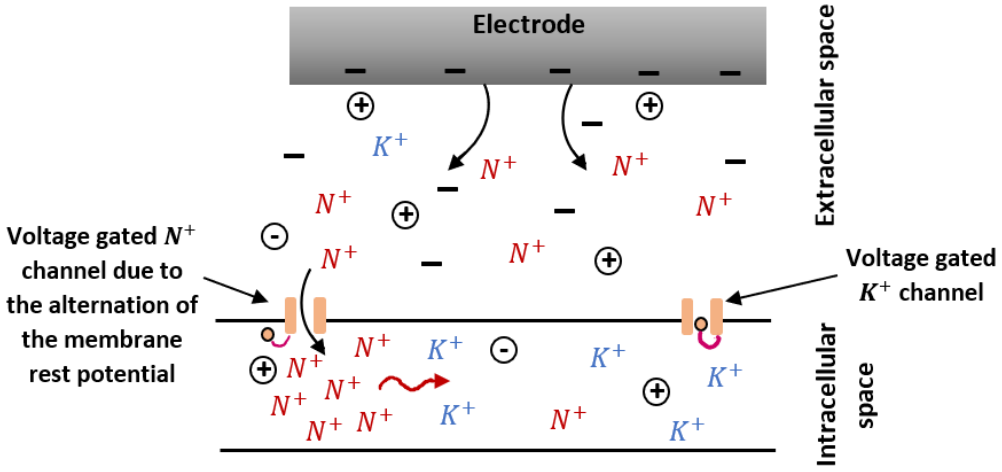

Figure 2.2: Cathodic electrical stimulation drives the extracellular space to become more negative, causing depolarisation of the cell (adapted from [1]).

2.1.1 Electrical stimulation for safe charge injection

The main challenge in designing electrodes and effectively deliver electrical stimulation for a long time without damaging the nearby tissues is to eliminate irreversible reactions over the lifetime of the application [1]. This is because if the electrode potential exceeds a threshold potential, this will result in the diffusion of molecules away from the electrode surface before they are reverted by the opposite polarity. The electrode potential must also not exceed the threshold where the electrolysis of water into gases occurs [1]. Therefore, the electrode should stimulate the tissue within a certain range of potentials, *water window*, in which the electrical stimulation can be delivered safely.

To assure safe performance of electrode stimulation, the charge injection limit must also be considered. The charge injection limit is the maximum charge that can be injected into the electrode during cathodic and anodic pulses without the electrode potential ever reaching an electrochemical potential that could cause irreversible redox reactions. This charge injection depends on the capacitance of the material and/or charge storage, which is mainly dependent on the material composition and surface structure. Therefore, extensive tests of the electrode material must be carried out to identify its suitability for such application.

2.1.2 Electrochemical process at the electrode/electrolyte interface

When an electrode is implanted, it comes into contact with the cell's extracellular electrolyte which contains ions and salts. An electric field is established at the electrode/electrolyte interface. This is due to a build-up of a double layer of charge, one at the electrode interface and the other at the electrolyte interface having an opposite polarity to that on the electrode. Once charge equilibrium is reached at the interface, charge movement due to a stimulus pulse can occur through two mechanisms: faradaic and non-faradaic processes.

2.1.2.1 Faradaic process

Faradaic reaction involves the transfer of electrons between the electrode and electrolyte via reduction-oxidation (redox) of chemical species in the electrolyte [38]. *Reduction*, the addition of an electron, occurs when a negative (cathodic) pulse is applied to the electrode in which electrons are ejected out from the electrode and accepted by metal ions in the electrolyte, hence the reduction of species in the electrolyte near the electrode surface [38]. *Oxidation,* the loss of an electron, occurs when a positive (anodic) pulse is applied to the electrode in which electrons are removed from the species (which have been previously reduced) and transferred to the electrode [38]. It can be noted that faradaic charge transfer can form products in solution that cannot be reversed if they were diffused away from the electrode surface, unlike in a capacitive system, discussed in the next section.

Figure 2.3 explains the electrochemical reaction that is happening at the electrode surface during a cycle. The current produced by the redox reaction is plotted against the scanned potential. Initially, when the potential is swept negatively the current is still very low [39]**.** According to the Nernst equation, which states that reduction will not occur until potential on an electrode is sufficiently reduced. When a threshold potential is reached [39], the driving force for the redox reaction is great enough to initiate the reaction [39]. This causes an increase in electrical current due to species being reduced near the electrode surface. The current continues until it reaches a maximum point called the *peak cathodic current*. Then the current drops off slightly as the potential is further decreased. This drop occurs due to the depletion of species available to be reduced near the electrode surface [39]. The analyte must diffuse into the electrode surface before it can react, which therefore can limit the current of the reaction. Consequently, a concentration gradient of analyte builds up as the sample molecules are consumed near the electrode surface. As a result, the current is limited by the rate of transport of analyte to the electrode surface [39]. When the potential is now reversed,

oxidation will not occur until the potential is sufficiently high. The oxidation peak starts to occur at higher voltages until a maximum current is reached, called the *peak anodic current* [39]. The current subsequently reduces as potential increases further as all species are oxidised near the electrode surface.

It can be noted that the current never goes to zero when potential is swept forward and then reversed. This is due to the accumulation of charges at the electrode surface which attracts the opposite polarity of charges in the electrolyte to the electrode surface, resulting in non-faradaic current. When the applied potential is too high or too low, this can generate some oxidant/reductant compounds which can also contribute to the current [39].

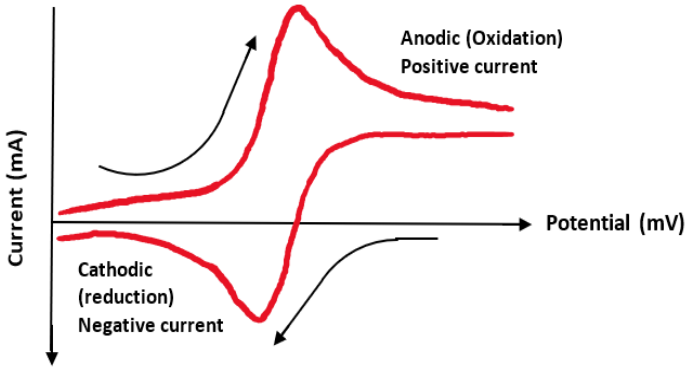

Figure 2.3: Typical cyclic voltammetry curve for reversible reaction showing anodic and cathodic peaks (Adapted from [39]).

2.1.2.2 Non-faradaic process

In *non-faradaic process*, there is no charge transfer as there is no chemical reaction occurring at the interface, instead an electrical double layer is formed at the electrode/electrolyte interface that act as a capacitor. When an electrode is first dipped into an electrolyte solution, for electroneutrality the excess charges on the electrode are exactly balanced by equal charges of opposite polarity in the solution due to electrostatic attraction. When ions are attracted towards the electrode surface, solvation sheaths are generated, which are formed from water molecules (in case of electrolyte based on water), called *solvated ions* [40], see Figure 2.4. It is known that water molecules are dipolar, the oxygen end of a water molecule forms a negative sheath, while hydrogen forms a positive sheath. When solvated ions approach the electrode surface, they do so at a distance allowed by their solvation sheath, therefore, the solvated ions are separated from the electrode surface by a distance equal to their solvation sheath plus the ion radius; the line drawn through the centre of

those ions at this distance of closest approach marks a boundary known as the *outer Helmholtz plane* (OHP) [40].

The *inner layer of Helmholtz plane* (IHP) contains anions that are specifically adsorbed in the water molecules and solvent molecules which are attracted to the metal due to their charged sheaths; such species are said to be *specifically adsorbed* and the line drawn through the centre of those ions at this distance of closes approach marks the boundary of the inner Helmholtz plane, also called the *compact Helmholtz* or *stern layer* [40].

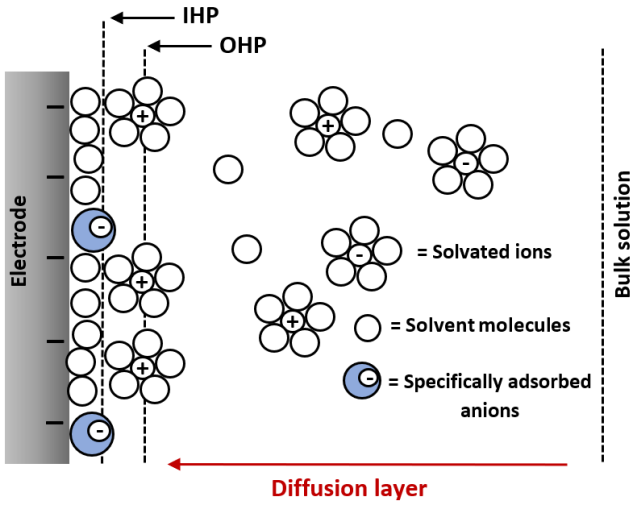

Figure 2.4: Structure of the double layer forming between metal/solution interface (Adapted from [40]).

Because the number of ions needed to neutralise the charges on the electrode cannot all be lined up at the OHP, the remaining ions are held at increased distance from the electrode surface, where electrostatic forces become weaker and ion dispersion is mostly controlled by thermal motion of the solution [40]. Due to this, solvated ions become distributed into a region called the diffusion layer, which starts from the OHP and extends into the bulk of the solution. Therefore, all the charge needed to neutralise the charge on the electrode surface are held between the OHP and bulk solution. The potential variation with distance from the electrode to bulk solution is illustrated in Figure 2.5. Due to the accumulation of charge of opposite polarity near the electrode, there is a linear potential drop between OHP and the electrode surface which extends through the double layer where ions are less concentrated and more distributed throughout the solution.

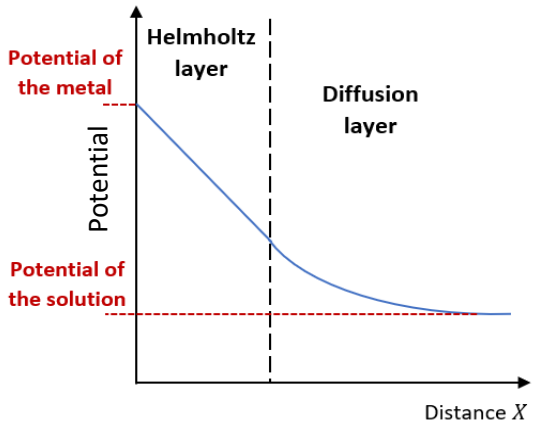

Figure 2.5: Variation of potential with distance from the electrode surface.

When the potential across the double layer is disturbed by the application of external voltage, ions arrangement or charge density in the double layer is redistributed to reach the electrical neutrality again. The redistribution of ions involves their diffusion from the bulk solution to OHP or the removal of ions from OHP to bulk solution, which consequently results in current flow between the interface. Therefore, the double layer capacitance is highly dependent on ion diffusion (especially their mass transfer kinetics), the diffusion layer thickness, the applied voltage and the scan or sweep rate. In capacitive system, there is no electron transfer, hence no chemical reactions, and in an ideal system the stimulation is completely reversible.

2.1.3 TiN properties

2.1.3.1 Structural and mechanical properties

Transition metal nitrides, such as TiN, is known for its high hardness, corrosion resistance and adhesion strength, hence it exhibits mechanical strength and stability, therefore, it has been an excellent candidate for protective coatings for metals and ceramics, such as coatings of biocompatible surgical tools and implants [41]. In addition, TiN has been extensively used in neural-electrode application, not just due to its mechanical stability but also due to its high conductivity and electrochemical stability. Since electrodes are used for chronical stimulation of tissues by the application of continues potential, the electrode material must exhibit high hardness to resist cracking and failure of the electrode. Therefore, current experimental and theoretical studies focus on improving its mechanical properties by tuning its structure and chemical composition.

TiN has a cubic structure with a bulk lattice parameter $a = b = c = 0.4240$ nm (PDF Card No: 038-1420). A single unit cell of TiN consists of two face-centred cubic (fcc) sublattices of titanium and nitrogen with 6 and 12 atoms, respectively, see Figure 2.6 [42]. In XRD patterns, TiN films usually exhibits different crystallographic orientation in which the most intense peaks are at 2θ ~ 36.7°, ~42.6°, ~61.8°, and ~74.5° (PDF Card No: 038-1420).

Previous studies of mechanical properties of TiN have reported that the mechanical strength of transition metal nitride comes from the material's structure and crystal orientation [41]. It was reported that TiN films with preferred orientation of (111) plane exhibited the highest wear resistance. This was attributed to the lower degree of misorientation across grain boundaries, which make it easier for the material to deform over the grain boundaries without formation of cracks, thereby increasing the materials mechanical strength [43]. Lim. JW, et.al [44] stated that the high hardness and Young's modules of TiN originated from the dense structure of the coating with a high compressive residual stress. Another study indicated that the presence of structural defects can either decrease or increase the material's hardness [41]. This was correlated to the effect of local mechanical softening and mechanisms involving the absorption of crack propagation energy at vacancy sites [41]. Therefore, TiN mechanical properties can be controlled by tuning the atomic structure, defects, vacancies and composition.

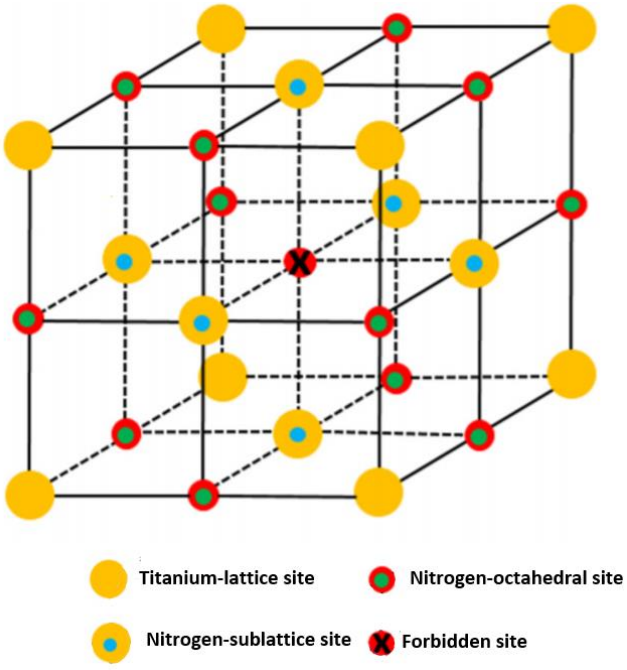

Figure 2.6: TiN crystal structure [42].

2.1.3.2 Electrochemical properties

Due to the excellent electrochemical properties of TiN, such as high electrical conductivity, cycling stability and corrosion resistance, it has been used in electronic devices, recharging power tools and electrochemical capacitors also called supercapacitors. TiN relies on storing charges in a thin double layer of anions and cations that develop at the electrode-electrolyte interface [27]. Considering the extremely high conductivity of TiN material, TiN nanostructure can well act as a potential electrode material for charge storage and delivering of high current density [19]. Many researches have studied the electrochemical properties of TiN through cyclic voltammetry and studied its effect upon varying surface area, grain size and surface roughness towards achieving the highest capacitance/charge storage values. The following research work are discussed to highlight the electrochemical properties of TiN of different structural properties.

A work has investigated the electrochemical properties of synthesis TiN powder at different temperatures [45]. The synthesised TiN powder exhibited different crystallite sizes and surface area. It was found that the highest capacitance was exhibited by TiN synthesised at 400 °C, while the lowest capacitance was exhibited at the highest temperature of 1000 °C. The increase of capacitance with decrease of synthesis temperature was correlated to the higher specific surface area and electrical double layer formation. The high specific surface area exhibited at lower synthesis temperature was related to the small crystallite sizes of the nitride. Therefore, although the powder synthesised at high temperature exhibited higher crystalline nature, the surface area had the greater effect in reducing the capacitance [45]. However, when the cycling stability of TiN powder synthesised at 400 °C and higher were tested by cycling up to 400 cycles, the capacitance of TiN powder synthesised at 400 °C reduced by 72%, while TiN synthesised at higher temperature were stable. The reduction in capacitance was referred to the growth of oxide layer thickness on the small crystallites, since the oxidation mechanisms are irreversible because Ti^{4+} is the stable ionic state in the oxide phase [45]. Therefore, it would be of an importance to synthesise a controlled morphology to avoid surface oxidation.

2.2 Literature review: neural electrode materials

A recent study investigated a time-related degradation of the external layer of DBS electrodes (the external layer which interfaces with the targeted tissues) by analysing the morphological and chemical alternations of three explanted electrodes under SEM and compared them with a new device [46]. The DBS electrodes system consisted of an outer jacket tubing, which was composed of polyurethane, and an internal insulating jacket made of fluoropolymer. The fluoropolymer acts as a coating material which isolates each single coil of the electrode that is made of platinum and iridium. The electrodes were explanted from three patients due to different reasons. Patient 1 had his device removed, after 4 years of implantation, for a malfunctioning reason; patient 2 had her device removed, after 6 years of implantation, due to the loss of efficiency (high impedance) without multifunction; patient 3 had his device removed, after 10 years of implantation due to a DBS infection (but without malfunction) [46].

The results showed that the electrode's degradation was not because of hardware malfunction or the parameters used during the therapy, but due to long-term usage [46]. SEM images revealed cracks on the outer jacket of all the electrodes and these cracks were worse in the patient who had the implantation for 10 years. It was concluded that the most probable factor in polyurethane and coil degradation was the biological response of monocyte-mediated macrophages and foreign body giant cells, which induce enzymatic activation causing degradation of the surface of the electrode. It is worth noting that the degradation only affected the superficial part of the outer jacket tubing. However, this indicates that if the implantation period was longer than 10 years, the polymer degradation could deepen and cause disconnection between the external biological spaces and the internal part of the electrode, hence, exposing the DBS system to a higher threat of causing malfunction [46]. Therefore, the choice of material is not only essential to minimize activation of the immune cells but also important to deliver the required amount of charge to tissue within the safe limits without losing its efficiency over time.

There is a recurring theme in the literature which suggests that in order to have a long-lasting functional neural interface, the electrode has to meet certain criteria to allow effective communication with the human nervous system. In this regard, the electrode material must have (1) small electrode geometry for selectivity of neurons area, (2) comparative mechanical tension with the tissue it interfaces with to reduce activation of immune cells [4], (3) high charge injection limit, (4) low impedance for effective charge injection, (5) long-term electrochemical stability and corrosion resistance. The next sections will explain those criteria in some detail.

2.2.1 Mechanical mismatch

Mechanical mismatch at the interface between the implanted device and adjutant neurons is one of the main reasons that leads to chronic inflammation [47]. Brain micromotion which arises from physiological, behavioural and mechanical sources such as cardiac rhythm, head movements and implanted device disturbances, respectively, could impose mechanical stress and strains on the adjacent tissues from the electrode, resulting in tearing of tissues [47]. Therefore, the electrode material has to be soft and its stiffness should be comparative to the tissues' (elastic modulus of 100 kPa). The effect of mechanical mismatch has been studied over several brain cell types by B. Morrison [48].

It was reported that astrocytes cells (star-shaped glial cells) sense mechanical stress and convert that information into mechanical messages. This causes activation of potent astrocyte antigens near the implant which has an implication for the generation of glial cells. The continuous micromotion at the electrode-tissue interface could increase the probability of glial scar formation [48]. According to Baek, S, et.al [49], the accumulation of active astrocytosis in the damaged area or at the interface generates a layer of activated microglia, which eventually encapsulates the implant and results in an increase in the neural interface impedance, hence reducing the possibility of recording single unit activity due to the increase of signal to noise ratio (SNR) or loss of stimulating the targeted tissues. This issue has been addressed by coating the metallic electrodes with polymeric films such as conductive polymers or hydrogels.

2.2.1.1 Coating electrodes with conductive polymers

Conductive Polymers (CPs) are largely claimed to produce a softer electrode interface, reducing the mechanical mismatch and stiffness between the metal electrode and the tissues with which it interfaces [13, 49]. Many papers have reported the elastic modulus of CPs to be between 10 MPa to 4 GPa which is much lower than the elasticity of metals (50 to 400 GPa) [13, 50]. According to Yang. J, et.al [13], dry CPs films based on PEDOT has shown elastic modulus in the rage of 1-3 GPa when it is in the dry form; in more recent research PEDOT in the hydrated form could reach an elastic module of 40 MPa [51, 4]. Although electrodes coated with PEDOT showed improved mechanical properties [51, 50], they are still two orders of magnitude higher than neural tissue's elasticity [4]. It was reported that the stability of PEDOT during *in vivo* stimulation, is critical, as it might suffer from electrochemical breakdown and conductivity loss after chronic stimulation [1, 49, 52]. This might be due to the fact that CPs are quite brittle and they their mechanical properties deteriorate over time [4].

2.2.1.2 Coating electrodes with conductive hydrogels

Alternatively, coating the metallic electrode with Conductive Hydrogels (CHs) has shown a greater improvement as compared to CPs. According to Baek, S, et.al [51], a gold electrode was coated with hydrophilic brushes fabricated from polyhydroxyethylmethacry (pHEMA) which resulted in a reduction of elastic modulus of the electrode from 70 GPa to 143 MPa. A similar study [49] coated a Pt electrode with biosynthetic co-hydrogel polyvinyl alcohol-heparin (PVA-Hep) and showed a reduction to around 100 kPa which is comparable to the stiffness of the tissues. Moreover, a comparison between Platinum (Pt), Conductive polymer and Conductive hydrogel in terms of their mechanical performance *in vivo* has been reported [53]. Results showed that Pt did not adhere well to the tissue resulting in a gap between the Pt and the tissue. CPs showed regions of delamination at the interface, while CHs was well integrated with the tissues and also demonstrated very minimal inflammatory response [53].

2.2.1.3 Coating electrodes with inorganic nanostructure materials

Coating the electrode with inorganic material, on the other hand, such as Pt-black, TiN and IrOx, is one way to increase charge injection capacity and decrease the electrode impedance, especially for those applications which require high density charge injection, such as cortical vision [4]. This was supported by further work reported by Marrese, C [5], and Boehler, C [12] where Pt black was introduced for electrode surface modification. However, the need to reduce the electrode dimension to improve selectivity can, for example, produce poor electrochemical behaviour in terms of cycling stability and corrosion. This is often referred to as the trade-off between selectivity (the ability to interact with small number of neurons) and sensitivity (signal-to-noise ratio). Therefore, the current limitations of implantable microelectrodes rely on the need for small geometrical surface area and high stimulus pulse or charge injection capacity.

Whilst the above work focused on coating the electrode with contiguous films and/or hydrogels and polymers, the high demand for increased current densities and solutions for chronic applications with improved mechanical properties, has led to the incorporation of nanostructured materials being coated on to electrodes. This has led to significant improvements in electrochemical, mechanical, and biocompatibility when compared to other coating materials, aiding the establishment of a chronically-stable neural interface [4]. These improvements result from the high surface area of the nanoscale materials which facilitates low impedance, high charge transfer or double layer capacitance and greater attachment to neural tissues, allowing for the fabrication of smaller electrodes and a potential concomitant reduction in problems associated with trauma within the brain tissue due to dimensional disparities [12].

Surface coating of high aspect ratio nanostructures such as nanowires (NWs), nanorods (NWs) and nanotube (NTs) on the electrode surface has been implemented to this end [12, 13]. In the literature, numerous interface materials have been studied in which the foremost predominant are platinum (Pt) [12], iridium oxide (IrOx) [7], 3,4-ethyleneddioxythiophene (PEDOT) [54] and titanium nitride (TiN) [20]. It has been reported that by growing a nanostructured Pt surface, the charge storage capacity (CSC) increased from 0.05 to 0.4 mC/cm^2 as compared to its film form [12]. In fact, sputtered TiN thin film showed a higher charge storage (0.2 - 4.66 mC/cm^2) as compared to thin film of Pt [22, 12] and as compared to CNTs electrode (1-1.6 mC/cm^2) [55].

The charge storage capacity can also be evaluated as specific capacitance (mF/cm^2). Studies showed that TiN sputtered thin film can exhibit capacitance ranging between 0.047 to 0.37 mF/cm^2 [56], while TiN-NWs used in the application of hydrogen evolution shown an enhanced capacitance up to 4.3 mF/cm^2 [20].

Therefore, the enhanced electrochemical properties are due, at least in part, to the increase in surface area of the electrode subsequently facilitating increased charge storage, a reduction in impedance and an improvement in cell survival.

2.2.2 Charge injection/capacitance and water window

In order to cause action potential in neuronal tissue, threshold stimulus pulse must be applied. It has been shown that in order to electrically stimulate the retina in visually impaired patients, a charge density between 0.048 and 0.35 mC/cm^2 or current density of 0.024 to 0.70 mA/cm^2 is needed to cause action potential and stimulate the retina [57]. Ideally, an electrode must be able to deliver high charge density that is capable of trigging action potential and stimulate for a long period of time without generating irreversible electrochemical reactions such as metal corrosions, gas evolution and/or transferring of toxic chemical produces into the electrode/tissue interface [58]. TiN material is capable of delivering high charge densities into the interface through a capacitive mechanism which involves the charging and discharging of the electrode double layer. Ions in the biological environment are accumulated or repelled by an applied voltage onto the electrode to produce pulses of ionic current. Charging and discharging of the double layer capacitance is an ideal mechanism of charge injection into the interface because no electrochemical reactions can be involved at the interface [58]. The applied voltages are however restricted to a range defined by hydrogen evolution at cathode and oxygen evolution or surface oxidation at anode. Those are considered irreversible reactions which degrade the electrode with further charge and discharge cycling [59]. This voltage limit is usually determined by the so called *water window* in which it is individually defined for each material Vs an electrolyte solution (-1 V to +1.2 V in phosphate buffered solution (PBS) for TiN material was recorded [58]). The water window are defined by the boundaries of inflection points or sharp increase in current beyond which the hydrolysis of water occurs [58].

It has been reported that the limit for safe charge injection is always determined by the assumed water window range [60]. In other words, a wider water window enables a higher charge injection limit. For TiN thin film the largest water window recorded in the literature is -3.0 to +1.0 V with a cathodic charge injection limit of 4.45 mC/cm^2 [22]. Another study showed a water window of -1.0 to 1.2 V with a charge injection of 2.2 - 3.5 mC/cm^2 [58]. By comparing the two studies, it can be noted that the broader the water window, the higher the charge injection limit. The reason for the discrepancy in the water window is the different approaches in determining its value [60] as well as the degree of roughness of TiN on the electrode [22]. However, both of those works have not reported the study of long-term performance of the electrode under the stated water window range, nor they have they studied the electrode surface composition after voltage pulsing. This is because such a wide water window could have a higher chance of causing oxidation of the electrode surface and/or reduction of the material into metal ions, both of which could degrade the electrode with further cycling, eventually reducing the charge injection capacity. Table 2.1 below shows a comparison of the charge injection and capacitance values reported in the literature of TiN film and TiN nanostructures with other nobel metals.

Table 2.1: charge injection and capacitance values of TiN film and nanostructured compared to other interface material

	Film		**Nanostructures**	
Materials	**Charge Injection mC/cm²**	**Capacitance mF/cm²**	**Charge Injection mC/cm²**	**Capacitance mF/cm²**
Platinum	0.05 – 0.15 [61]	0.06 [62]	0.4 [12]	-
Iridium oxide	4 [63] 4.7 [7]	0.2 – 0.4 [63]	1.9 [15]	-
PEDOT	0.75 [64] 3.6 [65]	0.0075 [6]	1.5 [64] 4.9 [6]	0.0138 [6]
Carbon nanotube	1 – 1.6 [55, 61]	-	-	-
Titanium nitride	Smooth = 0.024 [23] Porous = 0.04 to 0.07 [23] 0.25 [61] 0.80 – 1.41 [66] 0.87 [63] 2.2 – 3.5 mC/cm^2 [58] 4.66 [22]	0.058 to 0.032 [66] 0.5 – 1 [58]	-	Nanowires: 4.52 [20] Nanotube: 3.14 [19] Nanopore: 83.6 [19]

2.2.3 Impedance

One of the essential criteria that the electrode material must exhibit is a low impedance characteristic with the electrolyte interface. Since stimulation pulses are high frequency signals (about 3000 Hz), whereas cardiac signals utilize relatively low frequency range (about 100 Hz), characterising the impedance behaviour is of vital importance for electrode performance [61]. Lowering the impedance is fundamental to improve the recording quality by reducing the background noise and therefore increasing the signal-to-noise ratio (SNR) [14]. In addition, low impedance allows for the injection of relatively large capacitive currents along with keeping the electrode potential low.

A study done by Boehler, C, et. al [12], in which nanostructured Pt was coated on a Pt micro-sized electrode for the purpose of reducing the electrode impedance. The results of their study showed a reduction in impedance by two orders of magnitude compared to that of the untreated Pt electrode. In addition, this result was even better compared to the impedance achieved with conventional electrode coatings, such as IrOx and PEDOT (coated on the same design to that of the nanostructured Pt) [12]. Another study [6] fabricated PEDOT nanotubes on the surface of gold microelectrodes. The results showed a significant reduction in impedance of the coated electrode as compared to the uncoated gold electrodes. The magnitude of the impedance was decreased from 800 ± 20 kΩ, for the uncoated electrodes, to 4 ± 2 kΩ for PEDOT nanotubes coated electrode. These low values of electrode impedance have demonstrated a significant enhancement in the performance of these electrodes *in vivo*. It can be seen that, although Abidian, M, et. al [6] and Boehler, C, et. al [12] studies used inorganic and organic nanostructured material as a coating material, both showed impedance reduction by two order of magnitude lower than their bare electrodes. This could suggest that the surface geometry has a greater effect on the impedance than the type of the material used. TiN nanoarrays used for hydrogen reduction application has shown superior low impedance of ~1Ω which ultimately contributed to a high electrochemical capacitance performance [19].

To conclude, neural-electrodes must exhibit low mechanical mismatch, high charge storage, a wide water window rage and low impedance. Finding the most appropriate biocompatible material and technology for building neural-electrodes to be used for long-term implants in humans is a challenging issue. A considerable improvement in device technology is required to accomplish greater control of physiological effects. It is believed here that TiN-NWs would give a further improvement to the electrochemical performance of electrode as well as mechanical and biocompatibility. Therefore, this work will study the properties of the grown TiN-NWs, in particularly their structural and electrochemical properties as well as their biocompatibility to cultured cells.

2.3 Summary

This chapter has discussed the basic principle of electrical signals in neurons and how they can be externality stimulated using an electrode under safe conditions. In addition, possible electrochemical processes occurring at the electrode-neuron interface has been discussed. Moreover, the structural, mechanical and electrochemical properties of TiN material have been reviewed. Furthermore, current limitations in the use of neural-electrodes for recording and stimulation of tissues has been discussed. The literature has highlighted the fact that electrode material is the crucial aspect in designing a well-functioning neural-electrode device. Due to the need of designing smaller devices, neural-electrode materials face significant challenge in maintaining its electrochemical, mechanical, performance and biocompatibility. In this regard, nanostructured materials provide a higher surface area, which enhances the material properties and performance needed for the application. Common interface materials such as conductive polymers and hydrogels have been implemented and they have been shown to reduce the mechanical match with the tissues. However, a few reports claimed that those materials can delaminate over time. Nanostructured materials, on the other hand, have shown enhanced capacitance and reduced the device impedance.

Nanostructure delamination has not been reported in the literature. Therefore, TiN-NWs are proposed here as a neural-electrode interface material. A novel synthesis step to obtain TiN-NWs is suggested and the material properties are studied to test their suitability for the application. The next chapter discusses the fabrication methods used to grow TiN film and TiN-NWs in this work and the characterisation tools needed to examine their structure, composition and electrochemical behaviour.

Chapter 3. Synthesis and characterisation methods

This chapter discusses the working principle of the fabrication techniques used to grow TiN-NWs which involves three main processes; (1) RF magnetron sputtering, (2) hydrothermal solution growth and (3) PECVD. This is followed by the characterisation methods used to study the material properties. A suggestion of a coating mechanism of nanostructure materials onto electrodes has been discussed.

3.1 Synthesis methods

3.1.1 Radio Frequency Magnetron sputtering deposition

Sputtering is a *Plasma Vapour Deposition* (PVD) process performed in a vacuum chamber at pressures in the mTorr range to deposit a thin film of the chosen target material onto a substrate. The concept of sputtering is based upon the bombardment of positively charged ions, created in a plasma, onto the target material (cathode) causing ejection of the target's atoms which are collected on all surfaces including the substrate surface (anode). A large negative voltage (typically -1 to -3 kV) is applied to the cathode while the anode is grounded. Free electrons will accelerate due to the electric field built up between the cathode and anode. When those electrons collide with a process gas, e.g. Argon (Ar), they strip an electron from the gas atoms (ionisation) and create positively charged ions, hence plasma is generated [67]. Those positively charged ions are then accelerated towards the target causing sputtering, see Figure 3.1.

The plasma is sustained by the generation of secondary electrons, due to ion/surface interaction, which are accelerated into the plasma causing further ionisation of the process gas. The glow of the plasma near the target space can be correlated to the excess of energy, in the form of light, that is generated when a free electron recombine into an argon ion to become neutral [67]. On the other hand, a dark space exists between the plasma and the anode because those energetic electrons/secondary electrodes coming from the cathode eventually lose most of their energy in ionisation collisions, consequently they do not have enough energy to ionise or excite the gas atoms, hence no glow of plasma exist in that area.

Commonly, there are two different ways to power the cathode: direct current (DC) or radio frequency (RF) power supply. DC sputtering has one major disadvantage because insulating targets cannot be used as electrons cannot go through them and the positive charges attracted to the cathode would build up and eventually neutralise the target, preventing the attraction of further ions, and leading to failure of sputtering and secession of the plasma. RF sputtering, on the other hand, allow the use of the insulating as well as metal targets as the polarity of the applied voltage changes quickly, preventing the accumulation of positive ions near the target.

Due to the rapidly changing of the electric field direction, electron distribution in the plasma shifts up in energy through "in-phase" collisions, causing increased in ionisation [68]. "In-phase" collisions refers to those electrons in the plasma, while being accelerated by the electric field, make collisions before the electric field switches direction [68]. RF sputtering uses high frequency power source, typically 13.56 MHz, in which electrons and ions have vastly different mobilities in the fluctuating field. At such high frequency, ions are immobilised (due to their heavy weight), while electrons can oscillate in the glow plasma to increase collisions and hence ionisation. This could also remove the need to rely on the secondary electrons to sustain the plasma.

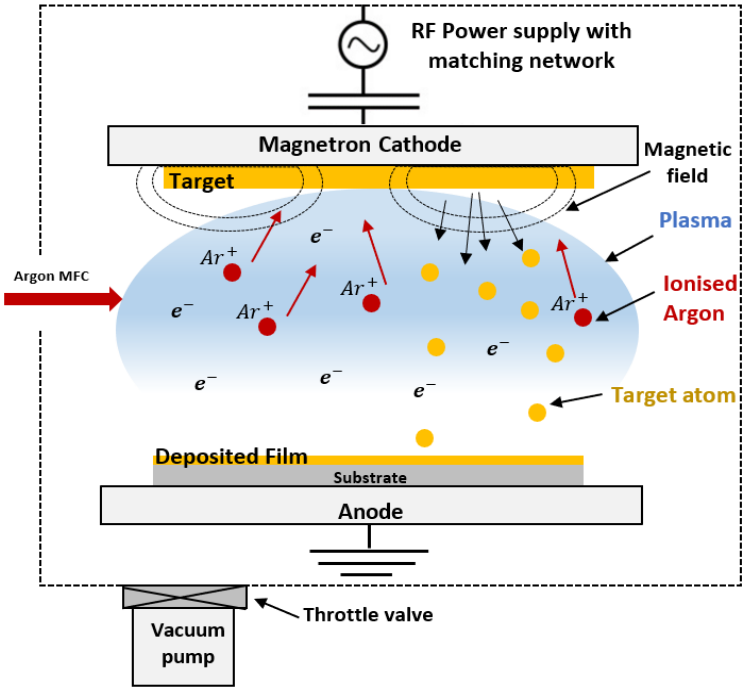

Figure 3.1: RF magnetron sputtering deposition diagram.

In order to further increase the efficiency of sputtering rate by increasing the number of collisions by electrons before they reach the anode, a *magnetron sputtering* is used by applying a magnetic field. Magnets are typically placed behind the negative cathode to trap the electrons in the plasma longer and, hence, produce more ions for the same electron density. This not only increases the plasma density but allow a reduction in the gas pressure since there would be no need to increase the gas pressure to increase the probability of collisions [68].

In this work, a magnetic RF sputtering system is used to deposit TiN thin layer from TiN target (8 inches in diameter) with Ar as the sputtering gas (its flow rate is controlled by Mass flow controller (MFC)).

3.1.2 Plasma Enhanced Chemical Vapour Deposition (PECVD)

Chemical vapour deposition (CVD) is a process in which a mixture of gases of the substance to be used are thermally decomposed to yield reaction products which are deposited onto a suitable substrate to form a grown film. PECVD has an additional advantage over CVD in which the activation energy for the reaction (e.g. decomposition reaction and gas/substrate reaction) to occur is not just achieved thermally but also by an energetic plasma which contains highly energised electrons that are able to dissociate and ionise the gaseous molecules to form chemically reactive radicals and ions, that can promote surface reaction [69]. This allow for the deposition of materials at lower temperatures (100 to 400 °C) as compared to the conventional (>800 °C) CVD [69].

Plasmas are, by definition, exhibit no net charge, i.e. the number of positive and negative ions are equal, hence their densities must balance in the overall plasma area. Although the plasma overall is neutral, there might be some local deviation from neutrality (quasi-neutral state). Those arise due to the externally applied electric field (or electromagnetic field) together with the different in mass of the ions and electrons, diffusion as well as the attractive and repulsive coulomb fields between the ions and the electrons.

When RF power (with a frequency of 13.56 MHz) is applied between the cathode and anode electrodes, potential differences is created between them resulting into an electric field which rapidly switches in direction. When the reactant gases are introduced, e.g. SiH_4 or NH_4, into the chamber through MFC, electrons, produced by background radiation or other process such as local field emission, accelerated by the electric field gain sufficient kinetic energy (of the order of 10 eV) to cause dissociation, ionisation and excitation of the gas molecules by collision, resulting into plasma formation. Hence, plasma contains chemically reactive radicals, e.g. NH_3, NH_2, neutral

atoms, molecules, as well as ions, and electrons. This process can be arranged by controlling the applied RF power, gas pressure (typically ~ 500 mTorr) and reactor geometry to yield a controlled plasma. A typical PECVD schematic diagram, and the one used in this work, is shown in Figure 3.2.

Ions and neutral molecules in the plasma have different mean kinetic energies; the kinetic energies of neutral molecules, relative to energy of any electron in the plasma, is much smaller (few hundreds of an eV less) [70]. This difference arises due to the energy acquired by electrons through collision, (driven by the applied field), since they are much smaller in mass. On the other hand, ions experience much smaller accelerations than electrons under the applied field due to their larger mass, and so between collisions they gain less kinetic energy. Therefore, since most of the mass in the plasma exhibits low mean kinetic energy, associated to those ions, the plasma can be called as 'cold' gas [70].

Since those electrons gain sufficient energy together by accelerating through the applied electric field and collision, they are sometimes quantified as 'hot' electrons, having temperature of the order of 50,000 K, while ions only have temperatures of the order of a few hundred K [70]. Due to this, the 'hot' electrons promote dissociation reactions of the gas molecules, generating high reaction rates at low substrate temperature, which would not be possible under the conventional thermal processes using similar chemistry.

There are two routes in which those species in the plasma leave the plasma: (1) by diffusing out of the plasma, (2) by the additional force imparted onto them either by collisions or by the applied RF field [71]. When the plasma contacts a substrate surface, even if that substrate is grounded, the substrate has a negative potential with respect to the plasma (the plasma is positive). Hence, positive ions would tend to bombard the surface with an energy dependent on the potential difference between the plasma and the substrate. Due to fast mobility of electrons with respect to ions, the positively charged electrode would receive a large electron flux, while the negatively biased electrode would receive slowing flux of positive ions on the first half-cycle of the field. Therefore, electrons would be depleted from the plasma, making the plasma positive in potential [71]. On the second half-cycle, the polarity of the electrodes reverse, and electrons attracts towards the electrode which previously received small flux of positive ions. On each subsequent half-cycle, negative charges continue to build on both electrodes and other surfaces (hence, leaving the plasma positive in charge), repelling further negative flux and attracting positive ions to the substrate surface [71]. The distribution of charges, and hence the relative electric field, between the plasma and the surrounding surface creates a thin sheath on both electrodes. However, the potential distribution

across those sheath are asymmetric because the electrode areas are different. The potential falls at the powered (cathode) electrode with respect to that of the ground electrode (anode) since the cathode electrode area is made smaller compared to the anode electrode area. Therefore, ion bombardment on the substrate surface would be minimised [70].

Since different gas species have different ionisation and dissociation energies, RF power, temperature, gasses flow rates as well as processing pressure can be monitored to insure high ionisation rate of gas species and generation of free radicals. Electron impact with the reactant gas can result in a number of different reactions depending on its energy: ionisation, excitation-relaxation and dissociation collisions in which all create highly reactive chemical species. Those reactions are discussed in the next sub-section.

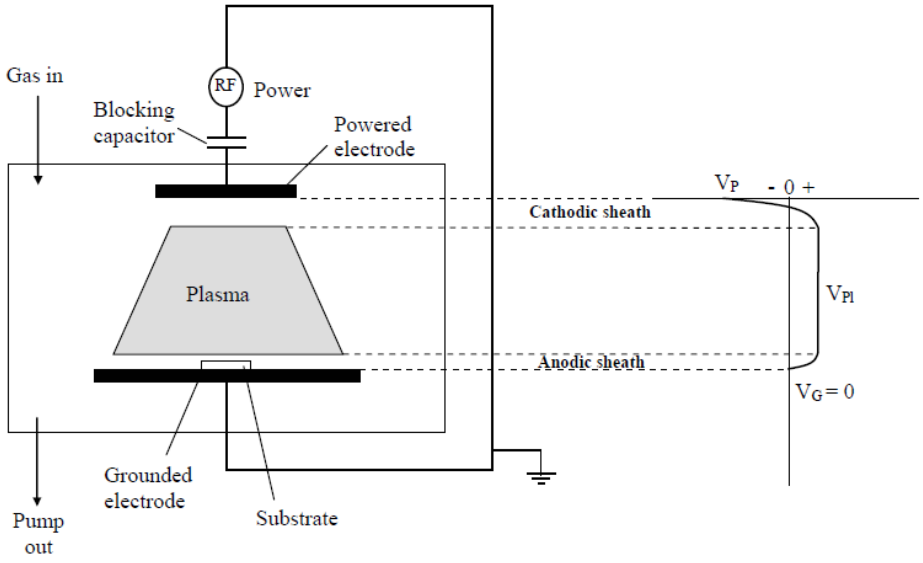

Figure 3.2: PECVD schematic diagram, showing potential distribution across the cathodic and anodic sheath where V_{PI} is plasma potential, V_P is potential of powered electrode and V_G is voltage on grounded electrode [70].

3.1.2.1 Plasma/Surface interaction

Due to the diffusion of free radicals, atoms, molecules and the bombardment of positively charged ions from the plasma onto the substrate surface, different species/surface interaction occur which results into different physical process [71]:

1) Ion/surface interactions:
   (a) Neutralization of species on the surface.
   (b) Emission of secondary electrons.
   (c) Sputtering/etching.
2) Electron/surface interactions:
   (a) Emission of secondary electrons.
   (b) Atom excitation.
3) Radicals or atoms/surface interactions:
   (a) Surface etching.
   (b) Chemical reaction with the surface.
   (c) Film deposition.

Films on substrate are formed by adsorption of radicals and formation of chemical bonds with surface atoms in which these process are promoted with particle bombardment since bombardment can break surface bonds creating adsorption sites, and increasing surface energy along with substrate temperature. The crucial reactions are those ones due to electron/species collision which are discussed in some details below.

3.1.2.2 Ionisation

Ionisation is an important process because it sustains the glow discharge or the plasma. It occurs when an accelerated electron collides with an atom or molecule and transfers part of its energy to an electron orbiting the nucleus of that atom or molecule. If enough energy is transferred to the orbital electron, the electron can break free from the nucleus and become a free electron (see Figure 3.3), leaving a positive charge on the atom or molecule. This process is called *electron impact ionisation* and can be expressed as [72];

$$e^- + A \rightarrow A^+ + 2e^-$$

It can be noted that the free electron here, that starts the plasma, can be originated from a cosmic ray or heat (thermal electrons).

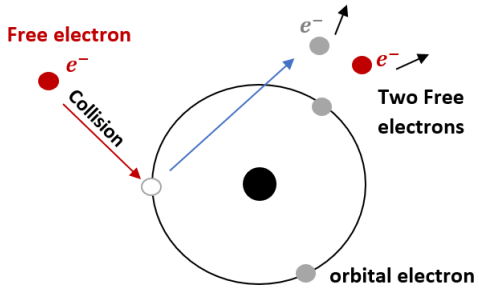

Figure 3.3: Ionisation collision process (Adapted from [72]).

3.1.2.3 Excitation-relaxation

When a free electron collides with an orbital electron in an atom or molecule with an energy less that the energy required for the orbital electron to break free from the nucleus confinement, the orbital electron jumps or get excited into a higher orbital energy level instead – this is called *excitation* and can be expressed as [72];

$$e^- + A \rightarrow A^* + e^-$$

Where A^* is the excited state of the atom A, indicating that it has an electron in a higher state. However, the excited electron falls back again to the lowest energy level possible to gain stability – this is called *relaxation* and can be expressed as followed [72];

$$A^* \rightarrow A + hv \quad \text{(photon energy)}$$

When the excited electron relaxes back to the lower energy level, it releases excess energy gained from the free electron impact, in the form of light (photon), see Figure 3.4. It can be noted here that this process is similar to Auger emission, but in Auger process, a free electron transfers enough energy to an orbital electron to break free from the atom, leaving a hole in that energy level, consequently and orbital electron from a higher level fall into the hole. The excess energy of this electron is emitted in the form of photon – this is Auger emission.

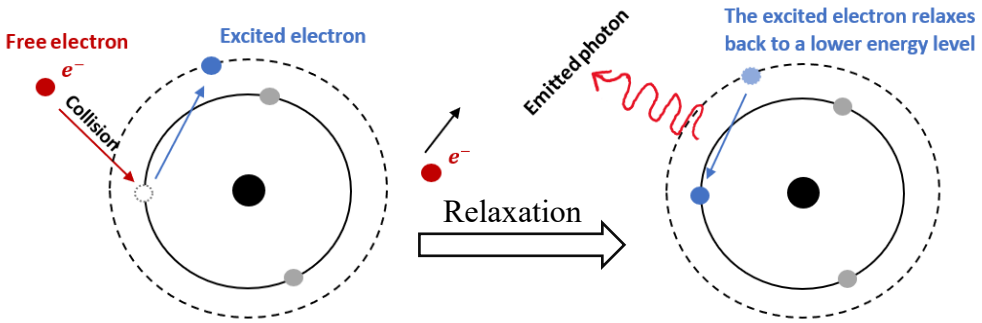

Figure 3.4: Excitation and Relaxation collision process (Adapted from [72]).

3.1.2.4 Dissociation

Dissociation occurs when a free electron impacts with a molecule, breaking its chemical bond and producing free radicals. This occur if the molecule absorbs an energy from the impacted electron that is higher than the molecule's binding energy. The reaction can be expressed as follow [72];

$$e^- + AB \rightarrow A + B + e^-$$

Where AB is a molecule, and A and B are the free radicals. The generated radicals are known to be chemically reactive because they have at least one unpaired electron and so they have high tendency to capture an electron from another atom or molecule to form a stable molecule.

3.1.3 Solution growth of nanostructured material

Solution growth methods are preferable over other synthesis methods due to their low cost, simple process, low temperature (<300 $^{\circ}$C), and high yield [73]. It is a powerful tool to produce nanostructured material with controllable morphology, structural properties and compositions. By optimising the synthesis conditions; temperature, reaction time, method of mixing, maintaining a pH value, concentration of the precursors and solvent [73], properties such as polycrystallite size, shape, surface area, such as nanowire length and diameter can be tuned. These are fundamental steps towards having better understanding of the nanoscale properties and essential towards their implementation in technological devices [73]. Solution growth such as sol gel solution chemistry [74], hydrothermal/solvothermal [75] [76], templating, such as electrochemical deposition [77], and biomimetic synthesis [78] have been extensively used to synthesise metal oxide nanostructures. These methods can be divided into two categories: seed layer based-solution growth and non-seeded solution growth, the two categories will be explained in the following sections. Since the growth of nanostructured material in solution is based on nucleation, precipitating and growth, it is essential to first understand the theory behind material growth.

3.1.3.1 Nucleation

First it is important to understand what nucleation is, when and why it occurs. Nucleation is a phase transition or the formation of a new phase from a bulk parent phase, e.g. the formation of ice (solid phase) in water (liquid phase). Before nucleation happens, the two phases are said to be at thermal equilibrium. Considering the phase diagram, in Figure 3.5, of a single molecule system with pressure (P) and temperature (T) axis.

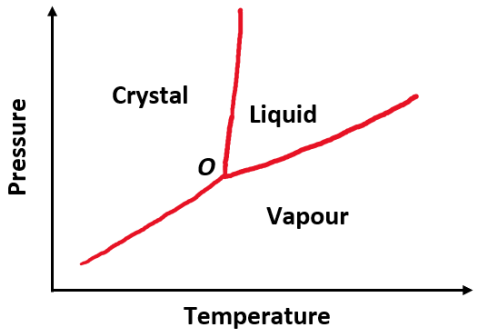

Figure 3.5: Phase diagram of a molecule.

According to the diagram, the crystal phase is said to be stable at high P and low T, while the liquid phase is stable at high P and high T, and the vapour phase is stable at high P and low T. If we consider a system with two phases, the two phases are said to be at equilibrium along the lines, while for three phases the equilibrium point lies at the triple point O. This is called the thermodynamic equilibrium of a system in which the system experience no gradients in temperature, concentration or other variables [79]. This is the state of lowest Gibbs free energy under the constraints imposed externally on the system. Now if the pressure of the gas phase is increased to a point above the equilibrium point (P_0), this will unstabilise the gas molecules with respect to its bulk and so there will be a difference in chemical potentials between the two phases in which the gas phase will have a higher chemical potential than that of the crystal [79]. This difference between the chemical potentials is also called the *thermodynamic driving force* for the phase transition (in this case crystallisation or nucleation of crystals) and it is known as the *supersaturation* [79]. This phenomenon can also be expressed in terms of Gibbs free energy (G).

At equilibrium, the net Gibbs free energy of any two phases is zero, however, when a fluctuation in the system occurs (e.g. increase in temperature), this leads to a difference in Gibbs free energy (ΔG) between the two phases. For example, at a temperature below the melting point of the solid phase, the Gibbs free energy of the solid is lower than that of liquid therefore there will be a driving force, leading to solidification (which is the lower free energy phase), to achieve the equilibrium state again [79]. At this stage, small nuclei form due to the driving force (because the system does not have the lowest possible free energy) but yet it cannot nucleate further due to interfacial energy (surface free energy), which results in a kinetic barrier for the phase transformation, this is called the metastable phase [80]. In other words, it is the early stage in which small crystallites, droplets or bubbles have large surface area to volume ratios and are unstable relative to their bulk phases. To make the system stable, work done on the system to allow the nuclei to grow in radius (r) [80]. When the nuclei exceed a critical radius (r^*), see Figure 3.6, the difference in Gibbs free energy will approach zero (ΔG_r) and nucleation initiates and growth occurs [80].

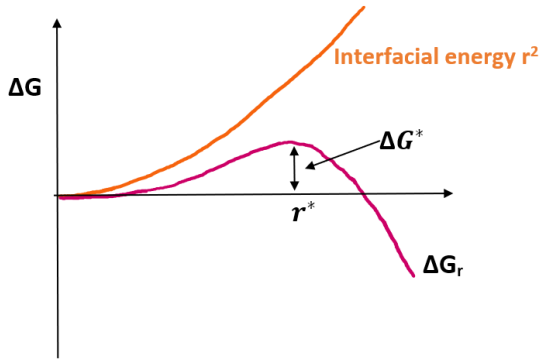

Figure 3.6: Gibbs free energy and the critical nucleus size and nucleation barrier (Adapted from [83]).

3.1.3.1.a Non-seeded solution growth: Homogenous nucleation

Homogeneous nucleation occurs when there is a thermodynamic fluctuation in the parent bulk phase which results in nucleation, crystallisation, forming droplets or bubbles [80]. The nucleation does not require the presence of a pre-existing particle to nucleate from, in other words nucleation occurs without preferential nucleation sites [80]. Hence it is more difficult to form a nuclei compared to heterogenous nucleation in which the energy barrier to overcome phase transition is higher in homogenous than heterogeneous.

There are few examples in the literature on solution growth based on homogenous nucleation in which no seed layer is presented. Such growth type often lead to randomly oriented nanostructured material. According to a work [81] which synthesised ZnO nanorods in solution, they have described the formation of a solid phase from a solution in two steps; nucleation and growth. When precursor concentration in the solution increases reaching the supersaturation stage (system is not under equilibrium), many nuclei form in the solution, and to minimise the surface free energy or Gibbs free energy, the nuclei grow in size passing the critical radius [81]. Due to the excess saturation of precursor, many nuclei aggregate together and individually grow along the *c*-axis, forming rod-like architectures [81]. Such a nucleation mechanism, can be assigned to homogenous nucleation.

3.1.3.1.b Growth from a seed layer: Heterogenous nucleation

Heterogeneous nucleation is favoured when there is a pre-existing particle (or a seed) to initiate the nucleation [79]. It is more common and much faster than homogeneous nucleation owing to the lower free energy barrier which comes from the surface free energy (or Gibbs free energy) [79] (see Figure 3.7). In heterogenous nucleation, unlike homogenous, the nucleus is not a complete sphere and so the contact angle or area of interface between the surface of the nucleus and the other phase (e.g. solid surface) decreases. The reduction in surface area (or interfacial energies) of the nucleus reduces the height of the barrier to nucleation. There are many examples in the literature for solution growth based on heterogenous nucleation [79].

The synthesis of titanium dioxide (TiO_2) nanowires through solvothermal method has been demonstrated previously [76]. It involved the decomposition of 1mL of tetrabutyl-titanate and titanium tetrachloride in a 1 M of toluene (an organic solvent). The mixture was transferred to a sealed Teflon autoclave (a typical solvothermal condition) with the pre-deposited seeding layers. The autoclave was then heated to 200 °C for two hours. The resultant nanowires were highly ordered and vertically aligned with respect to the surface [76].

The seed layer is expected to offer a large number of nucleation sites in which nucleation occur at the seed layer/ solution interface in particular at the grain boundaries. The seed particles promote the formation of critical crystal nuclei which can overcome the surface energy barrier. This is because the grain boundaries offer a reduced energy barrier for easier nucleation.

The advantage of using a seed layer for nucleation and growth of nanostructures is the ease of tuning of the nanostructure properties by tuning the seed layer properties. For example, polycrystalline seed layer can result in vertically aligned nanowires. Additionally, controlling the seed layer thickness can control the polycrystallite size and hence the diameter of the nanowire. Moreover, the growth of nanowires from a seed layer allow a control of the position of these nanowires.

Lithographic techniques are used to control positioning of the grown nanostructured material by pattering the seed layer. A paper reported the growth of ZnO-NWs by creating patterns of Au using a lithographic technique [82]. It was stated that it is possible to grow ZnO-NWs on the designed pattern since they grow vertically only from the region coated with Au.

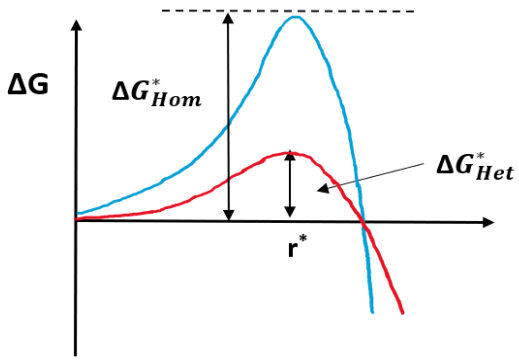

Figure 3.7: Homogeneous and Heterogeneous nucleation barriers (Adapted from [83]).

3.2 NWs coating of microelectrodes

Many different neural-electrode designs have been developed to enable the stimulation and recording of different type of tissues such as peripheral nerve and brain nerve system [4]. Neural interfacing electrodes can be generally classified into invasive electrodes, such as the conventional microwire electrodes, and non-invasive or surface sheet electrodes such as flexible electrodes [4].

Microwire electrodes are one of the earliest design of microelectrodes which compromise of thin wire made of stainless steel, tungsten and platinum/iridium, often insulated with polyimide and only exposing the tip [84]. The Michigan and Utah electrodes are some of the microwire electrodes design which are currently the most widely used electrodes. Microwire-types can be classified into single-wire and multi-wire electrode where the former is used for intercellular recording and the latter are used for extracellular recording [85]. Coating such electrode with nanostructure material can be done by growing the nanostructure material directly onto the electrode.

For example, a work has integrated zinc oxide (ZnO) nanowires on a tip of single microwire electrode with 75 μm in diameter through hydrothermal method [84]. First a seed layer of ZnO of 100 nm thickness was sputtered on the tip of the electrode followed by hydrothermal growth reaction in which the microwire was immersed into the growth solution which was maintained at temperature of 90˚C in a conventional oven. Only the exposed tip of the microwires had nanowires growth on while the rest of the body was insulated with polyimide. ZnO nanowires were then coated with IrOx films formed by electrodeposition to lower the impedance and increase charge capacity for neural stimulation [84]. Other penetrating electrodes have grown nanostructured material on the tip of the electrode using electron-beam-induced deposition (EBID) [86], Plasma Enhanced Chemical Vapour Deposition (PECVD) [87].

Flexible neural-electrode on the other hand are preferable over penetration electrodes because they reduce the possibility of damaging the tissue. These planner microelectrodes are thin film electrode arrays installed on flexible polymeric substrate, such as polyimide or C-perylene [88]. Usually the polyimide is spin coated onto a sacrificial layer such as a metal or a material that can be chemically etched [89]. A study has span coated polyimide onto a silicon substrate which at the end of the fabrication process was mechanically peeled off from the silicon substrate, keeping their original planar shape [89]. Gold circular electrodes were then patterned on the polyimide surface by photolithography followed by growth of carbon nanotubes (CNTs) PEDOT:PSS through electrochemical deposition [89]. Therefore, coating of nanostructure materials on different type of electrodes using different methods is possible.

3.3 Characterisation methods

This section explains the working principle of the characterisation tools used to characterise and study the properties of TiN films and nanowires. To characterise the material morphology, topography, crystalline structure, composition and electrochemical properties, electron microscopy, atomic force microscopy, X-Ray diffraction, X-ray photoelectron spectroscopy, Raman and Cyclic voltammetry are used respectively.

3.3.1 Electron Microscopy (EM)

When electrons bombard or interact with specimen atoms, they are significantly scattered by the specimen atoms either elastically or inelastically. Such interaction of electrons with sample surface can generate variety of emitted signals, and depending upon the energy of the accelerated electrons and sample density, those signals come from different penetration depths. Figure 3.8 shows the type of signals generated when an incident light of electrons interact with the sample and their corresponding detected technique. The generated signal due to elastic scattering is known as backscattered electron emission (BS), while the generated signals due to inelastic scattering include secondary electrons (SE), characteristic X-rays, auger and cathodoluminescence [90]. Origins of some of those signals are explained in the next sections.

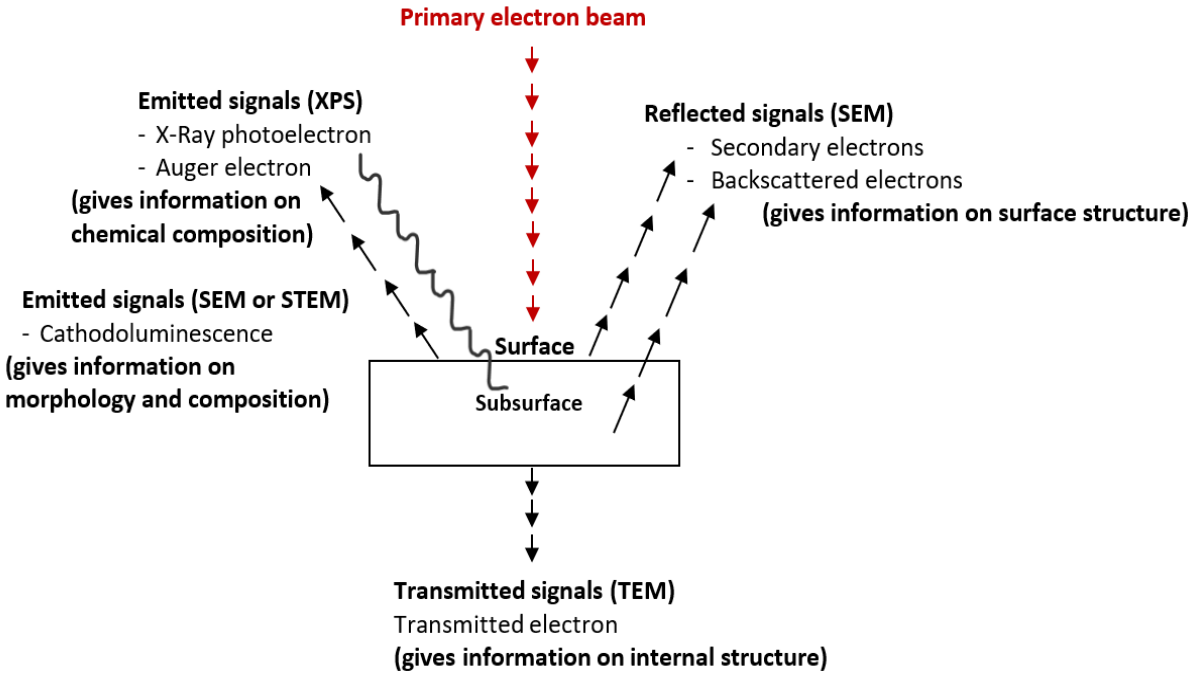

Figure 3.8: Electron beam interactions with a sample surface and subsurface and their characterisation techniques (Adapted from [90]).

Electron microscopy (EM) is a broadly utilised instrument for material investigation of microstructure morphology. *Scanning electron microscopy* (SEM) and *transmission electron microscopy* (TEM) are the two types of electron microscopy that use an electron beam to generate a magnified image of the test surface by detecting SE and BS signals [90], where high magnification images with a high resolution down to the nanoscale can be obtained. Typically, EM consists of an electron gun (e.g. tungsten), lens system, scanning coils and an electron collector, see Figure 3.9.

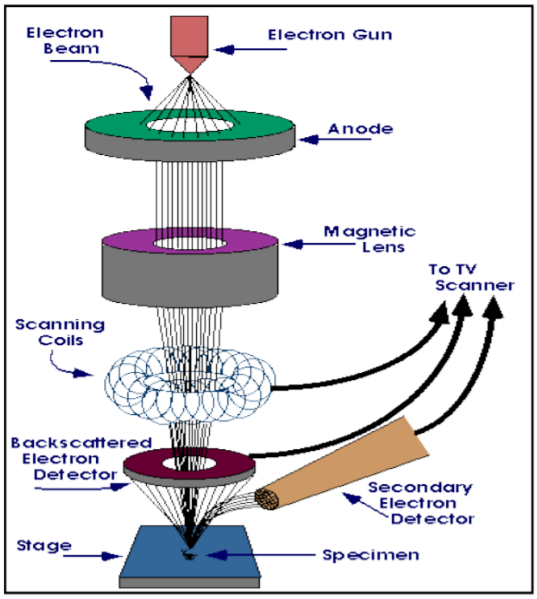

Figure 3.9: Scanning electron microscopy schematic diagram [91].

In SEM, electron energy is typically 10 - 30 keV. The *secondary electrons* (SE) signal is produced when the primary electron beam interacts with the nuclei of the specimen losing energy to a loosely bounded electrons causing ejection from the sample atoms (ionisation) [90], see Figure 3.10. SE signal results from low energy electrons, typically 50 V or less, due to the inelastic scattering that they experience (energy loss occur). It can be noted that SE propagates through the sample only several nanometer before they are reabsorbed by the sample, therefore they accurately define the position of the incident beam [90]. Consequently, SE signal produces high resolution image which in turns gives good topographic information.

Backscattering (BS) signal, on the other hand, can also be detected by SEM. The signal is generated when electrons undergo large-angle elastic collisions, leaving the sample with the same energy as the incident electrons, see Figure 3.10. BS electrons have the advantage in which it is sensitive to the atomic number (Z) of the atom. They are strongly scuttered off larger atoms compared to light atoms, thus the number of BS electrons is proportional to atomic number, hence producing higher signal (brighter image). This dependence can identify the sample's composition [90]. In addition, since BS electrons have higher energy than SE electrons, they can be scattered off from deeper subsurface layers of the specimen, giving information of the sub-layers.

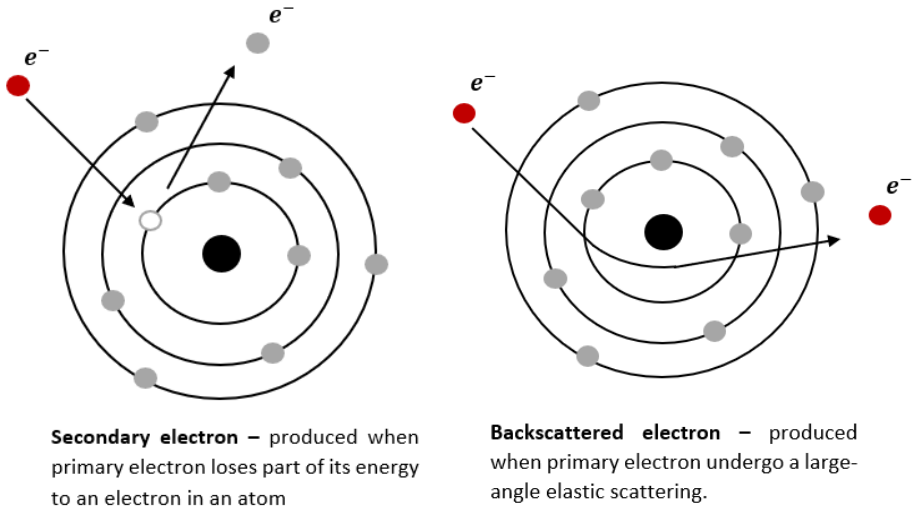

Figure 3.10: Electron-atom interactions.

TEM, on the other hand, uses electrons that are accelerated to higher voltages, typically 100 to 400 kV, and focused on the sample surface by lenses [90]. Due to the larger acceleration energy of electrons as compared to SEM, their wavelengths are much smaller, facilitating higher resolution. TEM uses electrons that are transmitted through the samples to acquire images before they are collected by the electron detector. In this case, the sample must be sufficiently thin (few tens to few hundreds of *nm*) to be transparent to electrons. Therefore, careful preparation of samples are needed before analysis. In TEM, the transmitted and forward scattered electrons (if any) can form a diffraction pattern which gives structural information. This is useful for crystalline samples, where selected area diffraction to identify crystal orientations, amorphous regions and defects. In *High resolution* TEM (HRTEM) the atomic size and spacing of the sample under investigation can be identified. This is useful when looking at interface analysis [90].

There are three primary imaging modes in TEM; *bright-field*, *dark-field* and the mentioned *high-resolution* microscopy. Bright-field images are generated only when transmitted electrons are detected, while dark-field images are generated when electrons are diffracted. Those species that cause electrons to be transmitted through usually have lighter atomic number, while those species that cause electrons to scatter or diffract usually have heavier atomic number. Hence, the heavier atoms do not appear on the screen and the image brightness is determined by the intensity of those electrons transmitted through [90]. The entire process of EM is conducted under high vacuum ($1x10^{-6}$ Torr) where electrons can freely travel with minimum collisions before striking the sample surface.

Different EM modes were used in this work to acquire images; SEM (model Leo S430) at De Montfort university and HRTEM, FEI Titan ST equipped with a field emission gun (FEG) working at 300 keV, at King Abdullah University for science and technology (KAUST).

3.3.2 Atomic Force Microscopy (AFM)

Atomic Force Microscopy (AFM) is a surface analytical technique which can be operated in air instead of vacuum. AFM uses a sharp microfabricated tip (typical tip radius of ~10 nm) attached to a cantilever which is raster-scanned over the sample surface. The advantage of using AFM is that it can image almost any type of material, including polymers, ceramic, glass, biomedical samples and insulator materials. In addition of acquiring topographical images of the sample, other physical properties of the sample such as average grain size and roughness can be identified.

AFM measures the displacement of the tip relative to the surface due to surface/tip interaction forces to acquire a high 3D spatial resolution image. When the tip is brought close to the surface (few 100 nm), attractive and repulsive forces, e.g. Van der Waals and coulomb forces respectively, cause a negative or positive bending to the cantilever. To be able to detect the motion of the cantilever, a laser is usually used which deflects off the back of the cantilever onto a photodiode detector, see Figure 3.11 [67]. Therefore, as the tip is scanned across the surface, it fluctuates up and down with the surface topography with accordance to tip/surface interaction forces. The displacement of the tip is then measured by detecting the laser deflection onto the detector and so a topographical image is obtained. There are three modes of AFM: contact mode, non-contact mode and tapping mode.

In *contact mode,* the tip is in a soft physical contact with the surface and is dragged across it under a constant force (using the feedback loop) so that the cantilever deflects at a constant order. However, both tip and sample can be subject to deformation as the tip can be dragged along the surface causing damage to the tip and surface [67]. *Tapping mode* is less destructive technique where it eliminates the frictional force between the tip and surface, and instead tip oscillates nearby its resonance frequency with sufficient amplitude to avoid the trapping of the adhesive forces. In *non-contact mode*, the tip does not touch the sample but oscillates vertically with respect to the surface. Due to the attractive forces between the tip and surface, such as Van der Waals forces, the oscillation amplitude, resonance frequency and phase of the cantilever changes accordingly. Those are utilised by a feedback loop to monitor the changes [67].

In this work, Park AFM XE100 (at DMU) with a non-contact mode is used to acquire images by repulsion of probe tip due to interatomic forces acting between the tip and the surface. However, due to the weak interaction forces between the tip and sample surface, a small AC signal (of an amplitude of 10 to 100 mV) is applied to the tip allowing it to oscillate, which then the change of its amplitude and phase due to surface interactions are measured and processed to construct a topographical image of the sample surface.

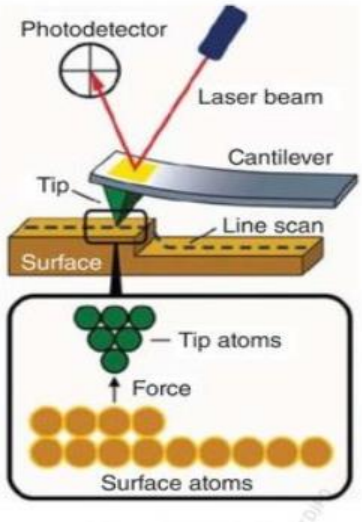

Figure 3.11: Schematic representation of AFM [67].

3.3.3 X-Ray Diffraction (XRD)

X-Ray Diffraction (XRD) is used to study the crystal structure of a specimens; it can identify whether a material has a regular (crystalline) or random arrangement of atoms (amorphous). This technique can also be used to identify other properties about the material, such as plane orientations, phase structure (e.g. cubic, tetragonal), crystallite size, stress and strain, atomic spacing or interplanar spacing.

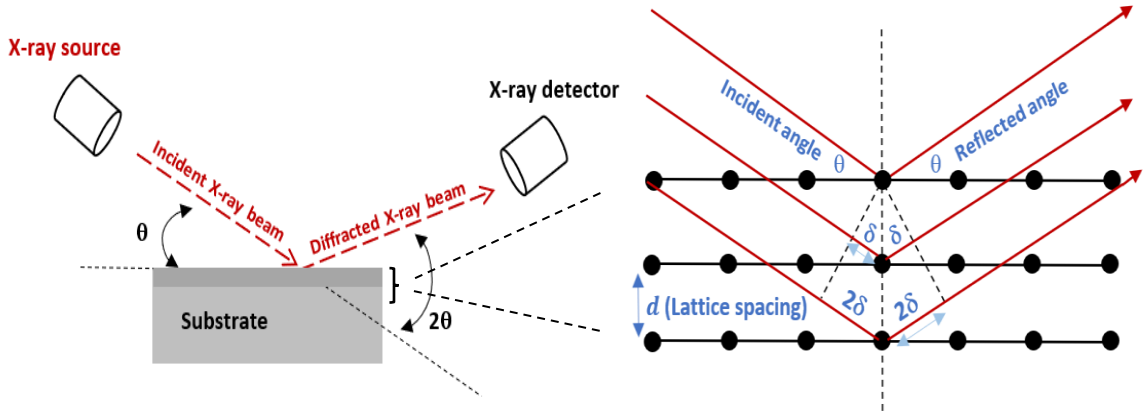

Figure 3.12: Basic geometry of X-ray diffraction (Adapted from [92]).

The X-rays are generated in a tube where an applied current heats up a tungsten filament which fires electrons. A high voltage accelerate those electrons onto a copper target where copper X-rays are produced. The X-rays exit the tube and incident on the test sample from which they are diffracted onto a detector, see Figure 3.12. The basic principles of diffraction on a three-dimensional lattice are shown in Figure 3.12 [92]. X-rays at angle theta (θ) are reflected from internal crystal plane separated by a distance d, the reflected X-ray form a spherical wave that carries the information about the arrangement of atoms in the lattice. When looking at the diffracted wave, a difference becomes apparent in the path length (δ) between the wave reflected from the zeroth lattice plane and the wave reflected from the first plane. The difference in the path length δ becomes a function of the interplanar spacing (d) (the distance between the lattice planes) and the angle of the reflected wave; $\delta = dsin\theta$ [92]. Consequently, the path difference between the zeroth and the second plane is exactly doubled; $\delta = 2dsin\theta$, if the reflected wave leaves the specimen under the same angle.

Therefore, for nth plane the total difference in path length is $2n\delta$. This leads to the condition for an interference maximum which is known as Bragg's equation [92]:

$$2dsin\theta = n\lambda, \quad n = 1,2,3, \ldots \tag{3.1}$$

where d is the interplanar spacing between two arbitrary planes in the lattice and n is the order of diffraction line. Once Bragg's equation is satisfied, this causes a single spike at specific detector angles. During the scan, the detector is rotated over a range of angles to detect bands of diffracted X-rays produced by the correctly aligned crystals within the samples.

In a cubic structure, such as TiN material, the interplanar spacing between two lattice planes with indices (hkl) and lattice constant a (noting that $a = b = c$ in cubic lattice) is given by [92]:

$$d_{hkl} = \frac{a}{\sqrt{h^2+k^2+l^2}} \tag{3.2}$$

In a tetragonal structure, such as TiO_2 material, the interplanar spacing between its lattice constants (noting that a =b ≠ c) is given by;

$$\frac{1}{d^2} = \frac{h^2 + k^2}{a^2} + \frac{l^2}{c^2} \tag{3.3}$$

Using the full-width at half-maximum (FWHM) of diffraction peak of the XRD patterns, crystallite size of the films can be calculated using the famous Scherrer formula [92]:

$$D = \frac{0.9\,\lambda}{\beta\, cos\theta} \tag{3.4}$$

where D is the crystallite size corresponding to the analyzed lattice plane with the miller indices (hkl), λ is the wavelength of the X-ray radiation, β is the FWHM of the peak (after subtraction of instrumental broadening) and θ is the Bragg angle.

In this work the crystallographic orientation of TiN films and TiN-NWs were characterised by X-ray diffraction (XRD), BrukerD8 with Cu-K_X-ray radiation having a characteristic wavelength of 1.5418˚A with 2◦/min scanning speed (at DMU). The samples were scanned through a range of 2θ angles (20 to 80°) where all the diffraction directions of the TiO_2 and TiN material lie.

3.3.4 X-ray Photoelectron Spectroscopy (XPS)

X-ray photoelectron spectroscopy (XPS), also known as *electron spectroscopy* for *chemical analysis*, is used to identify the chemical composition of specimen at the sample surface. It quantitatively characterises the elemental composition and chemical bonding states. One of the most common application of XPS is the determination of oxidation states of elements in inorganic compounds. XPS uses a high-energy X-ray radiation to eject core electrons from the specimen atoms (ionisation) in which their kinetic energies (KE) are related to the energy of radiation by [67];

$$KE = hv - BE - \phi \quad (3.5)$$

where hv is the energy of a photon (h is the Planck constant and v is the frequency of the radiation), BE is the *binding energy* of the ejected electron (also known as photoelectrons), and ϕ is the work function separating the Fermi level from the vacuum level, see Figure 3.13.

When a photon is incident into the sample, some of its energy is transferred to core electron, the energy transferred is equal to the energy needed to eject the photoelectron. In other words, the energy of the emitted photoelectron is equivalent to the energy loss of the inelastic scattered photon [92]. The kinetic energy or binding energy distribution of these emitted photoelectrons are then collected by electron energy analyser to be measured (Figure 3.13). Since the photoelectron binding energy is influenced by its chemical surrounding, BE becomes suitable for determining chemical states. This results in an energy spectrum exhibiting peaks characteristic of the sample. Each peak correspond to a specific KE or BE of a specific photoelectron which represent an atom. However, not all the peaks in the spectrum are due to emission of photoelectron, there are peaks that correspond to Auger emission, which are the result of electron relaxation to lower energy level to fill out vacant hole after being excited by X-ray radiation [90]. When the electron is relaxed, an excess energy in the form of photon is released which is then picked up by the analyser, resulting in an auger peak. The amount of photoelectrons recorded for a given transition is proportional to the concentration of that atom at the surface hence peak intensity varies. XPS is a surface sensitive because the ejected photoelectrons are originated from the first 10 nm of the sample surface [90].

In this work, an Axis Supra, Kratos analytical tool, with a monochromatic Al-K x-ray source and an energy of 1.4 x10^6 ev and a base pressure of $9x10^{-8}$ Torr was used. The CASA XPS software package was used for data analysis.

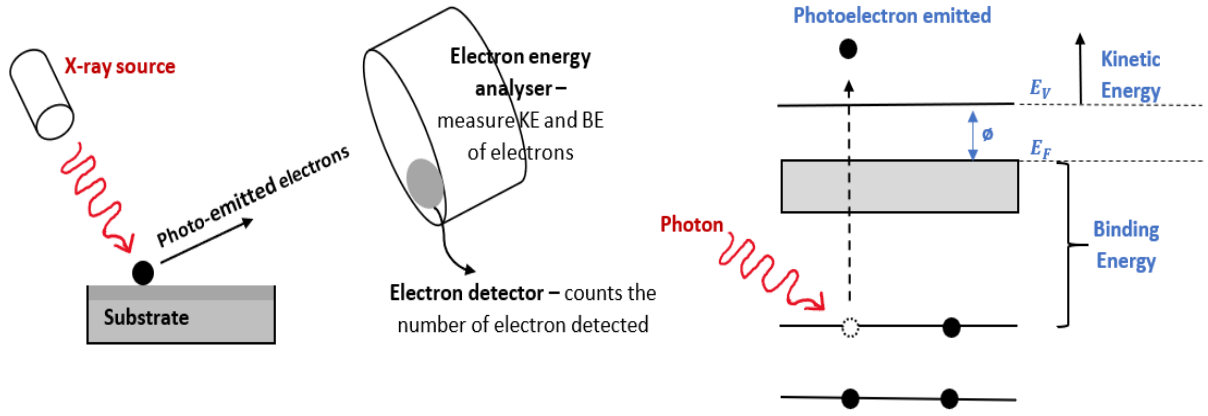

Figure 3.13: Working principle of XPS and Photoemission process (Adapted from [90]).

3.3.5 Raman Spectroscopy

Raman spectroscopy is a vibrational spectroscopic technique that uses scattered light from the surface of specimen to identify its chemical composition and crystalline nature. When light is scattered from an atom or molecule, the majority of the scattered light has the same frequency and wavelength to that of the incident light (elastic scattering), this scattered light is known as *Rayleigh scattering*. However, a small segment of the scattered light (around 1 in 10 million photons) has a different frequency to that of the incident (inelastic scattering), this is called *Raman scattering* [90]. Raman scattering is due to the interaction of the incident light (photons) with electrons in the ground electronic state of the molecule which cause either a loss or gain in energy of the scattered light. The incident photon excites an electron from the ground state to a higher state. This electron (or called *phonon*) relaxes back, either to a lower or higher vibrational state and emit a photon as form of energy. The difference in energy between the original vibrational state and the new state causes a shift in the emitted photon's frequency away from the excitation photon's frequency (the incident light) [90]. Therefore, Raman scattering detects the shifted frequency of the scattered light as compared to Rayleigh scattering due to the change in vibrational energy level of the molecule. Raman shifted photons can be either of lower (*Stokes shift*) or higher energy shift (*anti-stokes shift*) than the incident, depending upon the vibrational state of the molecule [90]. The resultant lower energy shift (or frequency) observed is because the excited electron relaxes back to a higher energetic state than the initial state, while a higher energy shift is observed due to the relaxation of the electron to a lower energetic state than the initial state. A schematic Raman spectrum is presented in Figure 3.14.

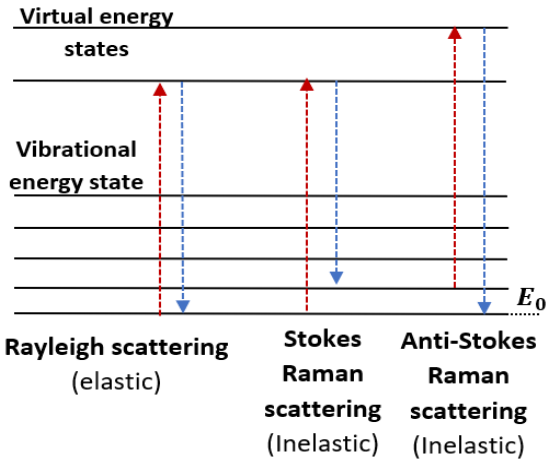

Figure 3.14: Energy level diagram showing Raman signals.

Since Raman scattering is very weak, Raman spectroscopy uses an intense monochromatic light source such as a laser. The laser light is shone over the test sample with wide range of wavelengths 4000–10 cm^{-1} to allow different absorption depth [90]. During Raman measurement, the scattered light from the sample surface goes through a double monochromator to block the Raleigh scattered light and allow the Raman-shifted wavelength to pass through and be detected by a photodetector [90]. The wavelength of the scattered light are then analyzed and matched to known wavelengths for identification.

In this work, Thermo Scientific DXR Raman spectroscope at King Abdul-Aziz university (KAU), was utilised to acquire spectra for all the nitrided samples using a green laser excitation (532 nm) with power of 10 mA and scan time of 96 seconds.

3.3.6 Cyclic Voltammetry (CV)

Cyclic voltammetry is an electrochemical technique that measures the current as a function of an applied potential. The voltage is linearly varied from an initial to a final potential and swept back at the same sweeping rate to the initial potential. CV provides information about the charge movement mechanism, capacitance value of the double layer, the reversibility of electrochemical reactions and the stability of its electrochemical property.

The capacitance of the electrode interfacing with electrolyte can be calculated using the following equation [19]:

$$C_s = \frac{i}{s \times v} = \frac{\left[\left(\int_{V_a}^{V_c} i(\upsilon) \times d\upsilon\right) / (V_c - V_a)\right]}{s \times v} \quad (3.6)$$

where Cs, s and v denote specific capacitance (mF cm^{-2}), the surface area of electrode material exposed to the electrolyte (cm^2), and the potential sweep rate (mVs^{-1}), respectively; i is the current response which can be obtained through integrating the area of the CV curves.

Charge injection (C_{inG}) is calculated using the charge on capacitor relationship;

$$C_{inG} = C_{capacirance}\, x\, V_{voltage} \quad (3.7)$$

CV usually consist of three electrodes; a working electrode (WE), a reference electrode (RE) and a counter electrode (CE). The WE is usually the material under investigation. The RE is usually made of Ag/AgCl which has a known potential, which is used to measure the potential difference between the working electrode and itself. CW is used to attract the countered ions near its surface while the opposite ions are being attracted at the WE. The schematic in Figure 3.15 is the experimental set up used in the present work. A known potential is applied to the working electrode, with respect to the reference electrode, and swept cyclically at a constant rate between two voltage limits. The resulting current, which is generated by the redox reaction (faradaic) or accumulation of species at the electrode surface (capacitive), is allowed to flow between the working electrode and the counter electrode [93]. The transfer of charge through those two reactions were explained in more details in section 2.1.2.1 and 2.1.2.2. As discussed previously, when a range of potentials is applied to the working electrode, rearrangement of the ions in the double layer will always occur, leading to a contribution of a capacitive current for each potential.

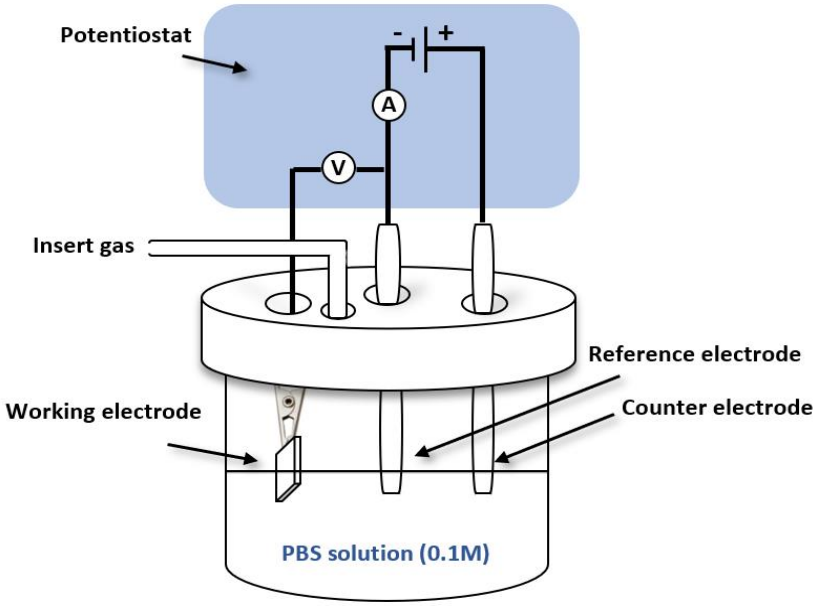

Figure 3.15: Schematic diagram of cyclic voltammetry experiment.

In the CV experiment, a capacitive current "envelope" can be obtained when the scan is performed in an electrolyte solution containing no faradaic species. The size of the capacitive current is a function of electrode surface area and the scan rate.

The stability of an electrode can be studied when sweeping the electrode potential over many cycles. In case of electrode having a capacitive behaviour, for example, the stability of its electrochemical performance is defined when the double layer capacitance maintain its capacitive behaviour over number of cycles (CV curve shape does not change as well as the integral area) and no/or minimum oxidation/reduction occur during cycling.

In this work, two cyclic voltammetry (at DMU) systems were used; (1) ACM GillAC CV, consisting of a three-body cell; a saturated calomel electrode (SCE) used as reference electrode, Pt mesh as counter electrode and TiN as the working electrode. (2) BioLogic VMP3 potentiostat, consisting of a three-body cell; Ag/AgCl used as reference electrode, carbon as a counter electrode and TiN-NWs as the working electrode. Initially results of CV behaviour of the sputtered TiN layer were obtained from ACM GillAC system. However, this system did not facilitate impedance measurement, hence the BioLogic VMP3 potentiostat was used to measure the impedance along with the CV behaviour. In addition, the latter provided higher measurement sensitivity (more data points were collected) as compared to the former.

3.3.7 Water electrolysis

Water electrolysis involves the breakdown of water molecules into oxygen and hydrogen gases. Reduction of water, occurring at the cathode electrode, results into hydrogen gas, while oxidation, occurring at the anode electrode, results into the evolution of oxygen, the following equations represent the half reactions of those processes [94];

Reduction $2H_2O + 4e^- \longrightarrow H_2 + 4OH^-$ (3.8)

Oxidation $4OH^- \longrightarrow 2H_2O + O_2 + 4e^-$ (3.9)

Electrolysis of water occur when sufficient potential difference is applied to an aqueous solution containing sodium hydroxide (NaOH) of 1 M (the standard condition) causing splitting of water molecules. Since the anode has a positive charge and cathode has a negative charge, an electric field is build up, causing Na^+ ions to attract towards the cathode and OH^- to attract towards the anode. OH^- ions give up their electron to the anode and oxidised to produce oxygen gas. The cell potential at the anode is -0.4 V (under standard condition). On the other hand, water molecules are reduced to hydrogen gas at the cathode by gaining electrons and the cell potential becomes -0.83 V. Hence, to drive the electrolysis of water a minimum potential difference between cathode and anode electrodes of – 1.23 V is required [94].

3.3.8 Electrochemical impdance spectroscopy (EIS)

Electrochemical impedance spectroscopy (EIS) is a tool to measure the electrical impedance of a system by applying a sinusoidal signal (voltage or current) at specified frequencies and analysing the resultant current or voltage response. The setup is similar to CV where three electrochemical cells are used; counter electrode, reference electrode and working electrode. The current flows between the working electrode and counter electrode, while the potential difference applied between the working electrode and counter electrode is such that the working electrode potential is at a set value with respect to reference electrode. So a constant potential difference is maintained between the working electrode and reference electrode.

EIS works by applying a small sinusoidal voltage (typically 10 mV) to measure the impedance over a broad frequency range, typically 1 Hz to 10^5 Hz [61]. In electrochemical cells, the relationship between voltage (V) and current (I) is highly non-linear and therefore, a small voltage is applied to get a current response that is linear.

The voltage applied can be of AC (frequency domain) or DC (time domain) signal. To avoid complexity, AC signal is often used and the resistance is replaced by impedance (Z) in ohm's law;

$$V = IZ \tag{3.10}$$

The applied voltage and the current response in AC signal are given by the relationship in equation (3.11) and (3.12) [95];

$$E_t = E_0 \sin \omega t \tag{3.11}$$

$$I_t = I_0 \sin(\omega t - \theta) \tag{3.12}$$

where E_t and I_t are the potential difference and current response at time t, respectively, E_0 *and* I_0 *are* the amplitude of the voltage and current signal at $t = 0$, respectively, ω is the angular frrequency ($\omega = 2\pi f$) and θ is the phase shift of current respond.

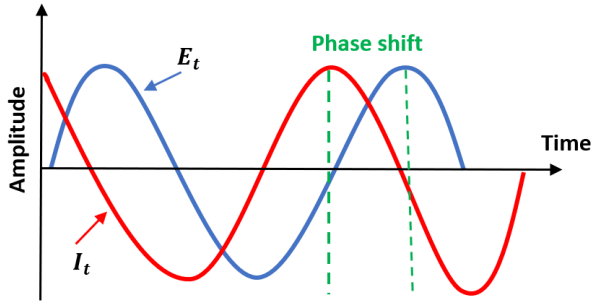

Figure 3.16: Phase shift in current as a response to excitation potential in a linear system.

It can be noted that both the applied voltage and current response are function of frequency in which both have phase and magnitude, see Figure 3.16. Therefore, the voltage is be applied over a wide range of frequency to allow impedance to be calculated by determining the phase shift and change in amplitude of the current response at different frequencies.

EIS data are commonly analyzed by fitting the data with equivalent electrical circuit model which consists of circuit elements that describes physical electrochemistry of the system. In a capacitive system, the impedance can be explained using Randles cell model which is one of the most common simplified cell model [95], see Figure 3.17. It consist of a solution resistance (R_s), a double layer capacitance (C_{dl}) and a polarization resistance (R_p) (polarization is due to a combination of kinetic and diffusion processes).

According to impedance and capacitance relationship in equation (3.13) [95], when the frequency is very low, the impedance of the capacitor is extremely high which force the electrical current to go through R_s and R_p, resulting in a total impedance of $R_s + R_p$. On the other hand, when the frequency is high, the impedance of the capacitance is low which allows the current to cross R_s, resulting in impedance due to R_s only [95].

$$z_C(w,t) = \frac{1}{jwC} \tag{3.13}$$

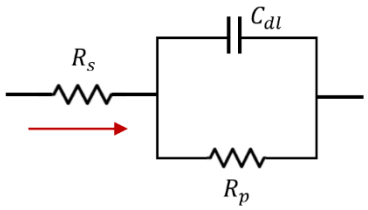

Figure 3.17: Randles Cell equivalent circuit.

IES data can be represented in two ways; Bode plot where it shows impedance value at different frequencies, whereas Nyquist plot shows the imaginary and real part of impedance (see Figure 3.18 (a)-(b)). In the Bode plot, the behaviour of capacitor performance can be realized from the spectrum by the indication of the decrease of impedance with the increase of frequency, while Nyquist plot usually indicate a semicircle at high frequency followed by inclined line at 45° at lower frequency [96]. In this work, BioLogic VMP3 Impedance was used to collect data. The measurements were made at the open circuit potential, with a frequency range of 4 MHz to 1 Hz and an applied AC voltage amplitude of 10 mV. The experiments were conducted at room temperature and atmospheric pressure in a 50 mL glass container where Phosphate-buffered saline (PBS) was used as electrolyte.

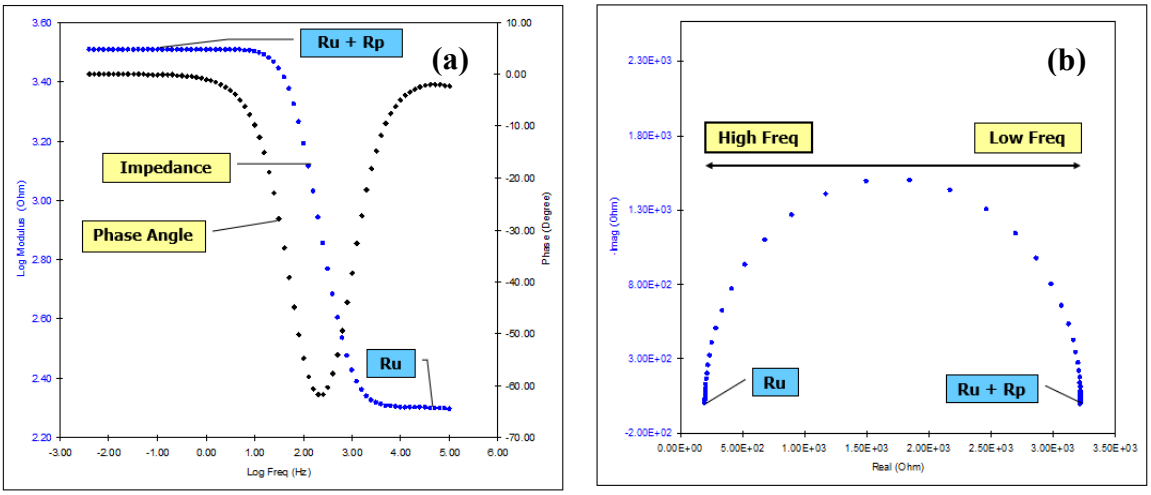

Figure 3.18: Impedance plot representation (a) Bode and (b) Nyquist plot [155].

3.3.9 In vitro assessment

There are different type of assessments to evaluate the biocompatibility of an interface material having cells cultured on its surface, those include proliferation assay, apoptosis assay and necrosis assay [97]. Proliferation assay is used to measure the cellular metabolism and that can be done by the use of 3-(4,5-Dimethylthiazol-2-yl)-2,5-diphenyltetrazolium bromide (MTT) to assess the metabolically active cells. The assay uses tetrazolium salt which react with the cell's enzyme (if the cell is alive) to create a purple colored compound (called formazan), illustrating that the cells are viable [97]. Another way to assess the proliferation of cells is to assess the rate of cell growth by measuring the number of cells exhibiting Ki-67 protein which appears as cells prepare to divide into new cells. Due to the limited resources, proliferation assessment of GBM cells used in this work was done through staining cells for Ki-67 protein.

Necrosis assessment, on the other hand, is commonly used to determine the viability of the cells by testing the integrity of the cell membrane [97]. The membrane integrity is measured by uptake of the dye such as Neutral Red (2-amino-3 methyl-7-dimethylaminophenazoniumchloride). If the cell membrane is intact by the influence of surface morphology of stress, then the Neutral Red can radially diffuse through the plasma membrane and bind with the lysosomes [97]. However, alternation of the cell membrane can result in a decrease of uptake and binding with neutral red dye, hence, it is possible to distinguish between viable and dead cells [97]. Another way to assess the viability of the cells, which is used in this work, is staining the nucleus of the cells with DAPI (4′,6-diamidino-2-phenylindole), a blue-fluorescent DNA stain. DAPI can diffuse through the plasma membrane of both live and dead cells. Since dead cells undergo fragmentation during apoptosis, by visualizing the cells through florescence microscopy, dead cells would have several pieces of nucleus (commonly 3), or the dye is leaked out of the nucleus while live cells will have one round nucleus.

In terms of cells morphological assessment and behaviour, this work has used Nestin marker to visualize the cells morphology and examine the change of their morphology upon culturing them on TiN films and NWs. In addition, cell distribution across both surfaces was assessed by taking images of cell nucleus across the sample and calculate the average nucleus distance.

Chapter 4. Results - Deposition of TiN nucleation layer

4.1 Introduction

Among all the deposition techniques to grow TiN film such as electron beam thermal evaporation [98], pulsed laser deposition [99], molecular beam epitaxy [100] and direct current sputtering [101], to our knowledge, *non-reactive* RF magnetron sputtering has not been used to deposit TiN film which can provide an easier optimisation and controllable of the film properties. This chapter explains the deposition process of TiN thin film through non-reactive RF magnetron sputtering and the film characterisation results. A design of experiment (DOE) to optimise the sputtering process has been established using two level approach. A TiN target was used to deposit the thin film. The sputtering parameters; RF power and Argon (Ar) flow rate were varied to optimise the structural properties, such as crystals orientations, polycrystallite sizes, and surface roughness. The optimised parameters were then used to further investigate the effect of varying film thickness on crystallite size and grain size. In addition, Ar flow rate was varied to study its influence on the electrochemical properties of the films. TiN film was acted as a nucleation layer for the growth of TiN-NWs, therefore, it was essential to optimise its properties towards polycrystalline structure, and stable electrochemical behaviour. polyrystalline structure could relatively help mediating the transduction of the action potential to the NWs, while producing highly aligned nanowires. The electrochemical behaviour of TiN nucleation layer was optimised as it would form part of device structure in future work, and further was compared to that of TiN-NWs. Some of the results in this chapter were reported previously [102].

4.2 Experimental work

TiN_X was sputtered through RF magnetron sputtering ultilising an eight-inch-high purity (99.99%) TiN target in an argon (Ar) gas atmosphere. All TiN films were deposited on glass substrates ($2x2\ cm^2$). For all depositions, the distance between the target and the substrate was kept constant at 7 cm, the reaction chamber was evacuated to a base pressure of $4x10^{-6}$ Torr and depositions were performed at room temperature. The Ar flow rate was controlled by MFC measured in standard cubic centimeters per minute (sccm). Prior to all depositions, glass substrates were ultrasonically cleaned sequentially with Deionised (DI) water, acetone and Isopropanol for 30 minutes each, followed by rinsing with DI water and drying under nitrogen gun. The samples were loaded into the vacuum chamber and a shatter was placed above the TiN target. Ar gas was then introduced into the chamber until a desired sputtering pressure was reached (~4 to 8 mTorr). Power was applied to TiN target to strike the plasma and ramped up slowly to the desired value, while the shatter was being shielded from the target.

The TiN target was pre-sputtered for 10 minutes to remove potential impurities from the target surface. The shatter was then opened and the deposition was timed to achieve the desired film thickness. After the process is over, the same steps were carried in reverse to close the plasma and vent the chamber. Samples were removed and taken for characterisations.

The structural properties of TiN film, in particularly, crystallographic orientations, polycrystallite size, Root Mean Square (RMS) roughness, thickness, grain size as well as electrochemical properties were investigated by varying the sputtering power and Ar flow rate from 100 to 300 W and 10 to 80 sccm, respectively [102].

Design of experiments (DoE) was used to initially optimise TiN film using two levels and one centre point resolution (see Table 4.1). To minimize thermal stress on the target while exploring a wide parameter range, the maximum RF power was set at 300 W with a power density of 0.24 W/cm^2, while the minimum level of RF power was set at 100 W for initial optimisation and 200 W as the center point. The maximum and minimum levels of Ar flow rate was chosen to be at 10 and 80 sccm as the broadest level within the MFC system and 45 sccm was set as the middle point. It can be noted that when the flow rate was set at 10 sccm, the sputtering pressure was around 4 mTorr, and as a result of applying higher flow rate of 80 sccm, the sputtering pressure reached 6.5 mTorr. Hence RF power and Ar flow rate were the only variable parameters.

These sputtering conditions resulted in deposition rates variation from 0.03 to 1.10 Å/sec as it will be seen in the next section [102].

Table 4.1: Experimental conditions for the DoE optimisation of TiN film [102].

	Level 1 (Min)	**Center point**	**Level 2 (Max)**
RF Power	100 W	200 W	300 W
Argon Flow rate	10 sccm	45 sccm	80 sccm

4.3 Deposition rate

By varying RF power and Ar flow rate, deposition rate could be controlled and the highest deposition rate could be achieved. Deposition rates were calculated by sputtering films at different sputtering conditions and measuring the film thicknesses (using AFM) and deposition times. Figure 4.1 shows an interaction plot illustrating the influence of RF power and Ar flow rate on the deposition rate of TiN film [102]. Initially, the deposition rate slightly increased when RF power increased from 100 to 170 W, followed by a rapid increase in the deposition rate from 0.1 to 1.1 Å/sec, when the power increased to 300 W. On the other hand, the increase of Ar flow rate from 10 to 80 sccm caused a slight reduction in the deposition rate by 0.02 Å/sec [102].

It can be observed that RF power had the prominent impact on the deposition rate as compared to Ar flow rate. This can be correlated to the increase of Ar ion flux and their kinetic energy (KE) upon striking the target [103]. The increase of Ar ion flux causes substantial ion bombardment onto the target while their increased KE promotes more sputtered atoms from the target material [103, 102]. This contributes to the increase in rate at which atoms strike the substrate, therefore, increasing the deposition rate. In addition, the quality of the film can be improved due to these sputtered atoms striking the substrates with greater energy, due to the momentum transfer from Ar ions, leading to increase in surface mobility [103, 102]. However, the slight decrease in deposition rate with increase in Ar flow rate is due to the fact that sputtered TiN atoms experience higher number of collisions in the plasma before reaching the substrate [103]. The reduced mean free path reduces the rate at which the sputtered atoms reach the substrate, thus when those sputtered atoms reach the surface, they do so with lower KE which result in a decrease of their surface mobility, hence lowering film quality [103]. Comparable dependence relationship of the effect of RF power and Ar flow rate on the properties of deposited films were reported elsewhere using this deposition technique of different materials [103, 104, 105].

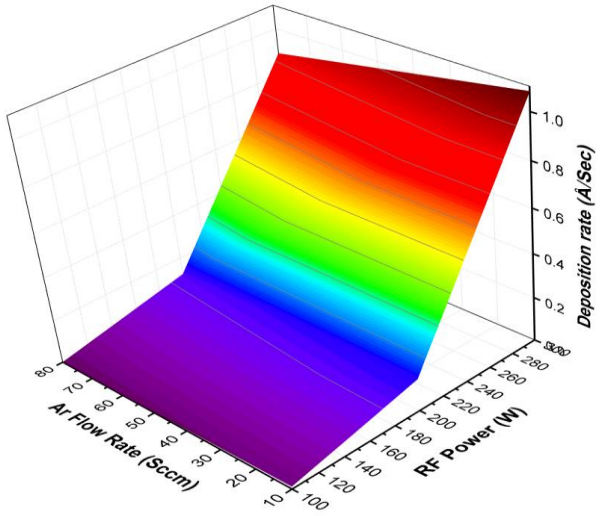

Figure 4.1: Effect of RF power (W) and Ar flow rate (sccm) on deposition rate (Å/sec) [102].

4.4 Structural properties

Figure 4.2 shows SEM image of a sputtered TiN film (300 nm thickness), at 300 W, 80 sccm, illustrating a columnar growth [102]. XRD of TiN films deposited at various sputtering powers and Ar flow rates are presented in Figure 4.3 (a)-(b), respectively, noting that the thickness of the film was kept constant at 300 nm in all the deposition conditions [102]. All the diffraction patterns correspond to the cubic structure of TiN (face centered cubic (FCC)) [106]. To investigate the influence of RF power on film crystallographic orientation, Ar flow rate was maintained at 80 sccm, and RF power was varied from 100 to 300 W. From Figure 4.3 (a), no appearance of diffraction peaks for the film deposited at 100 W, which could be due the insufficient energy of the sputtered atoms needed to form crystals that can be detected, therefore 100 W was excluded from further investigations [102]. However, an increase of RF power to 200 W, resulted into a sharp peak at ~43° with (200) plane orientation, while a further increase in power to 300 W resulted in peaks at 36°, 61°, and 78° with (111), (220) and (222) planes respectively, indicating polycrystallites forming in the material [102]. The increase in RF power could have improved the KE of the sputtered atoms arriving at the surface, allowing them to migrate and align in crystal forms [106]. Similar results were observed by [101, 107, 108].

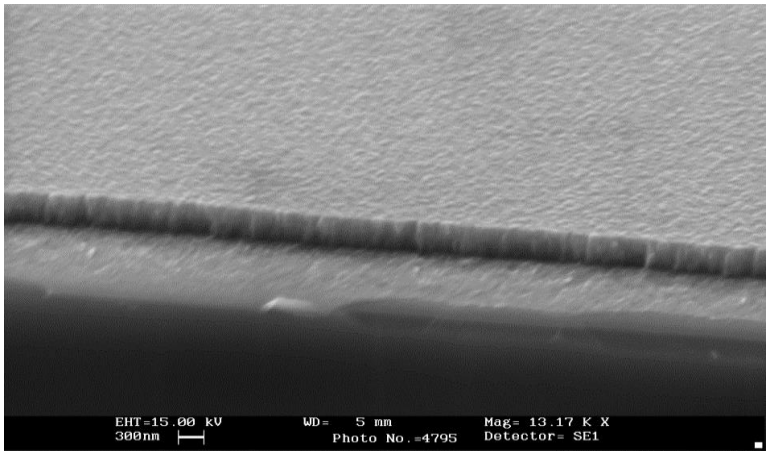

Figure 4.2: SEM Image of TiN deposited at 300 W, 80 sccm showing columnar growth structure [102].

TiN thin film was sputtered using the conditions in DoE, however, due to the different crystallographic orientations of the films, two Ar flow rate levels were added to further understand the orientation variation. Figure 4.3 (a)-(b) shows the effect of varying RF power and Ar flow rate on the crystallographic orientation of the films [102]. At 300 W, 10 sccm no diffraction patterns were evident, while at 65 sccm TiN film was polycrystalline exhibiting a plane at (200). At Ar flow of 80 sccm, it seems that the film exhibited different plane orientations, making (111) plane the preferred orientation. Further increase in Ar flow rate (95 sccm) lead to polycrystallites oriented in (200) plane with lower peak intensity compared to the other films [102]. Generally, the change in preferred orientations can be explained in terms of the overall energy of the films which is composed of surface energy and strain energy [109, 110]. The surface energy is dominant when the energy of the incident particles onto the substrate is relatively small, noting that (200) plane exhibit the lowest surface energy. This is because the number of broken bonds per unit area is minimum at (200) plane, making it the lowest surface energy. On the other hand, strain energy is dominant when the energy of the incident particles onto the substrate is relatively higher, and so, particles tend to find the plane with the lowest strain energy, e,g (111), hence the preferred orientation [109].

From the above, the change in preferential orientation from (200) to (111) and back to (200) with increase in Ar flow rate, could be because at 80 sccm, the sputtered particles have sufficient energy to crystallise into (111) plane due to the decrease in deposition rate, which as a consequence provides the advantages to those deposited atoms to have enough time to find optimum bonding sites [102]. However further increase in Ar flow rate, further reduces the deposition rate and so the energy of the impinging particles, which make them crystallise into the lower surface energy plane (200).

Therefore, it can be seen that the less energetically favourable orientation (111) only forms within a narrow band of Ar flow, with (200) more dominant elsewhere [102]. It was reported that (111) plane orientation can provide higher wear resistance for TiN films. This could be of advantage when the material is interfaced with the biological environment. Therefore, from the results above, the sputtering conditions of 300 W and 80 sccm might be a potential optimum condition in this work for the sputtering of well polycrystallite TiN film.

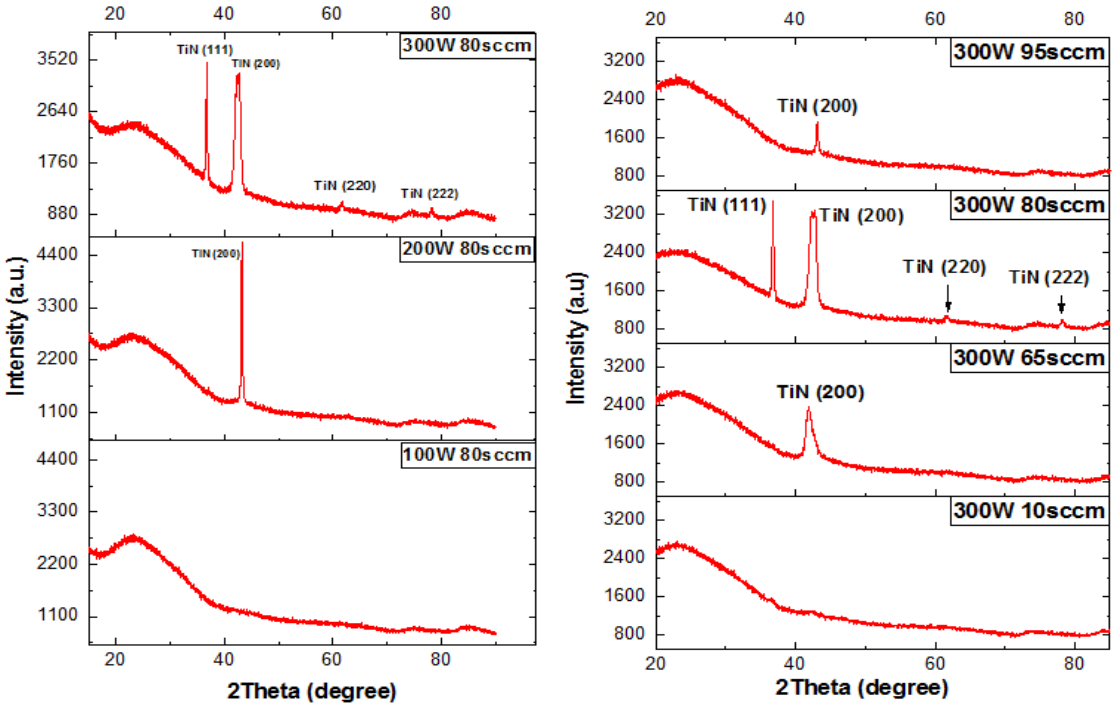

Figure 4.3: XRD data of TiN sputtered at (a) 80 sccm with varying RF powers, and (b) 300 W with varying Ar flow rates [102].

To confirm the composition of TiN film, XPS of TiN film grown at 300 W, 80 sccm was collected and is shown in Figure 4.4. The high resolution XPS spectra for Ti 2p region is presented in the binding energy range of 471-450 eV, where three overlapping peaks of Ti $2p_{3/2}$ forms a doublet with three overlapping Ti $2p_{1/2}$ lines. The binding energies at ~455 and 461 eV ($2p_{3/2}$ and $2p_{1/2}$ respectively) confirms the presence of TiN (Ti^{+3}), while those peaks located at 458.7 and 464.4 eV, are assigned to Ti^{+4} phase of TiO_2 [111]. The broad peaks between TiN and TiO_2 peaks are assigned to titanium oxynitride (TiO_xN_y - Ti^{+2}) [112, 113, 114]. Therefore, the grown film has a mixture of TiN and oxide. The presence of TiO_2 material could be due to the surface oxidation of TiN as soon as the samples comes in contact with the atmosphere, while the formation of TiO_xN_y might have occurred during the sputtering process.

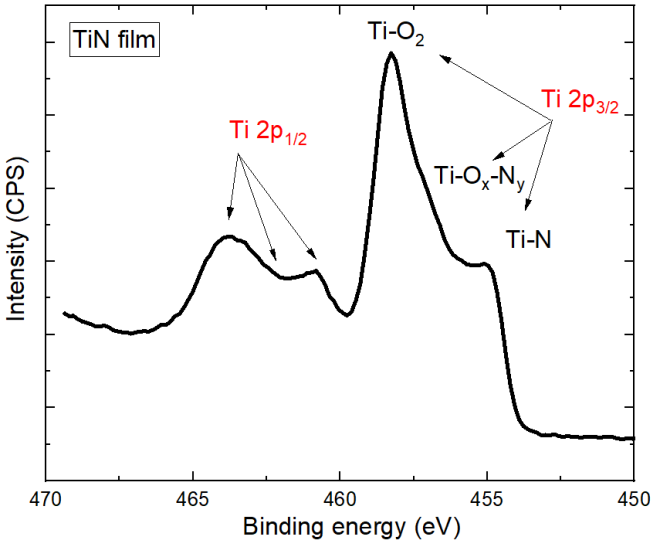

Figure 4.4: XPS of TiN film deposited at 300 W, 80 sccm showing Ti 2p region.

4.5 Polycrystallite size and RMS surface roughness

Table 4.2 illustrates the effect of varying RF power and Ar flow rate on the polycrystallite size and RMS surface roughness of TiN deposited films [102]. The polycrystallite sizes are calculated from (200) diffraction peak using equation (3.4), while RMS surface roughness are obtained from AFM measurements. At a sputtering power of 300 W, the polycrystallite size of the films increased from 13 to 95 nm, when Ar flow rate was increased from 65 to 95 sccm. On the other hand, increasing RF power from 200 to 300 W, while maintaining the flow rate at 80 sccm did not have the same level of effect on the polycrystallite size, in fact it only slightly increased from 10 to 20 nm [102]. The same trend is seen with the RMS surface roughness in which Ar flow rate greatly influenced the surface roughness as compared to the RF power, see Figure 4.5 [102]. The variation in polycrystallite size and surface roughness with Ar flow rate can be explained by the relationship between the mean free path (λ) and the molecular diameter of the sputtering gas [115],

$$\lambda = 2.330\ x\ 10^{-20}\frac{T}{PM} \qquad (4.1)$$

where T (K) is the temperature, P (Torr) is the sputtering gas pressure which is proportional to the flow rate, and M is the molecular diameter of the gas [116]. According to the equation, when the sputtering pressure increased (as a consequence of increasing the flow rate), λ decreases due to the number of collision that the sputtered atoms experience before arriving onto the substrate. Consequently, the sputtered atoms would have a higher probability of agglomeration in the plasma before depositing onto the substrate surface, which could lead to an increase in grain size as well as polycrystallite size. Although, energy of the deposited particles are reduced upon increasing the flow rate, this could give more time to those sputtered atoms to migrate onto the surface and find optimum bonding sites before any new sputtered atoms arrive (decrease of deposition rate) [116]. Figure 4.6 (a)-(b) shows 3D AFM images of the TiN films sputtered at 10 and 80 sccm, illustrating the effect of Ar flow rate on the topographical structure of the TiN films [102].

Table 4.2: Influence of deposition parameters on polycrystallite size and surface roughness of TiN film [102].

Parameters		Polycrystallite size (XRD) (nm)	Average roughness of 5 µm scan size (AFM) (nm)
300 W	10 sccm	No polycrystallites	0.694
	65 sccm	13	1.17
	80 sccm	20	1.570
	95 sccm	95	1.95
80 sccm	200W	10	1.375
	300W	20	1.570

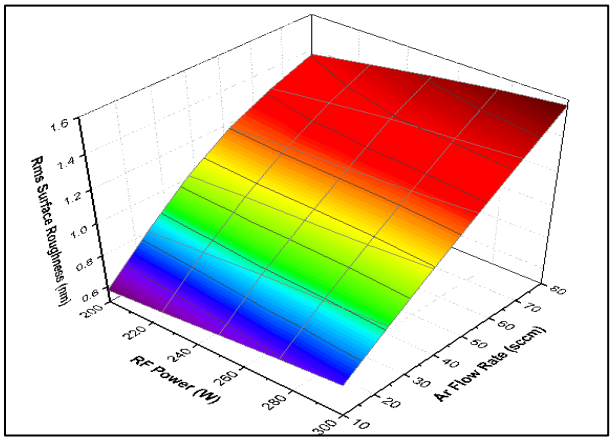

Figure 4.5: Effect of RF power (W) and Ar flow rate (sccm) on surface roughness of TiN film [102].

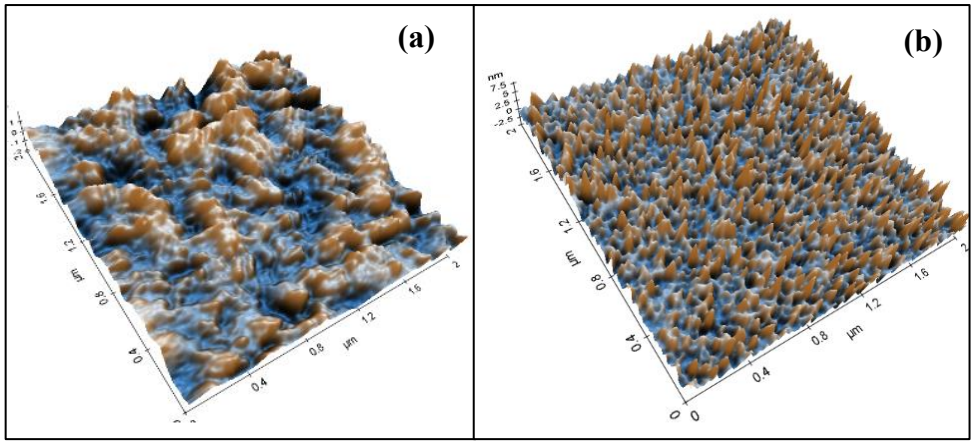

Figure 4.6: AFM 3D Images of TiN film surface deposited at 300 W a) 10 sccm and b) 80 sccm showing the effect of Ar flow rate on surface roughness [102].

4.6 Effect of thickness on polycrystallite size, strain and lattice parameters

The optimum sputtering condition of 300 W, 80 sccm was used for thickness variations since the resultant film exhibits various crystallographic orientations. Thickness was varied from 100 to 700 nm and their XRD patterns are shown in Figure 4.7. It can be seen that films at 200 and 300 nm thickness exhibited preferential orientation of (200) plane, while films grown from 400 to 700 nm exhibited preferential orientation of (111) plane. At 100 nm thickness, no peaks were observed which could be due to the amorphous nature of the film. As explained before in section 5.4, the change in preferred orientations can be explained together in terms of the surface energy and the strain energy, however, in the case of varying film thickness, the change in preferred orientation cannot be explained in terms of the overall energy of the film because the surface energy and mobility of adatoms cannot be changed with film thickness since all deposition conditions are the same except the duration of deposition. Another driving force for the preferred orientation would be the internal stress as the thickness of the film increases. Internal stress is composed of intrinsic and thermal stress. Thermal stress can only be considered if the film was heated and cooled after, therefore, intrinsic stress is the only driving force in this case. However, it is reported that the intrinsic stress causes large strain energy within the film [109]. Hence, the change in preferred orientation with thickness will be explained in terms of the strain energy only.

It is known that the strain energy of the film is proportional to the film thickness [109]. Therefore, (200) plane is observed as the preferred orientation at low thickness (200 to 300 nm) due to the small strain energy, while (111) is observed as the preferred orientation at thicker films due to the dominance of strain energy.

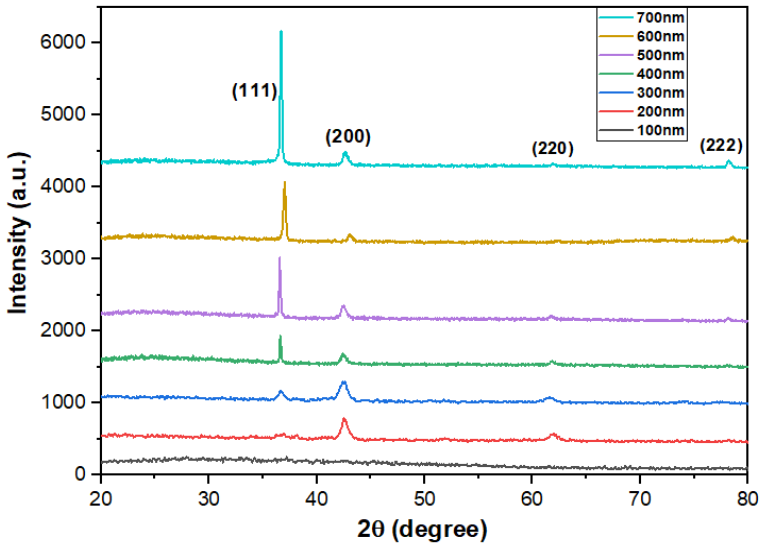

Figure 4.7: XRD spectra of TiN films sputtered on glass at 300 W and 80 sccm with varying thickness.

From Figure 4.7, the increase in the intensity of (111) plane as film thickness increased, indicates that the film is more polycrystalline in nature. By finding the FWHM of the preferred orientation (111) as well as (200) plane of all thickness, the polycrystallite sizes were calculated and their effect with film thickness are presented in Figure 4.8. It can be seen that there is no noticeable change in the polycrystallite sizes corresponding to (200) plane with increase of thickness, while the polycrystallite size corresponding to (111) plane remarkably increased from 47 nm to 83 nm when thickness increased from 300 to 700 nm. The large increase in polycrystallite size of (111) plane as compared to (200) plane might be because that the polycrystallites prefer to grow in (111) plane rather than (200) to lower their strain energy caused by the increase in intrinsic stress with increase of thickness.

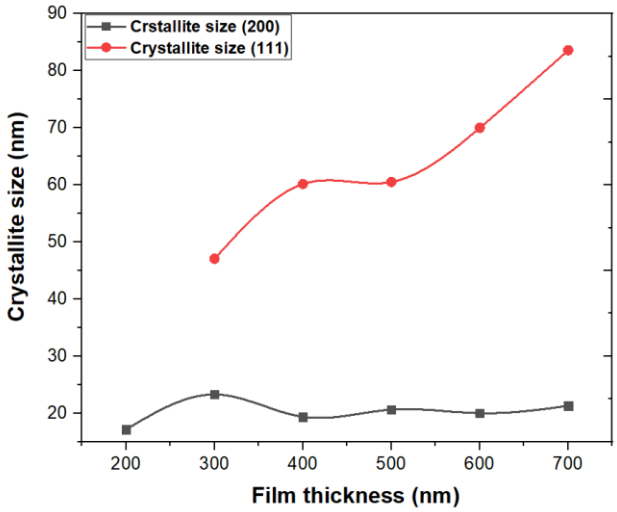

Figure 4.8: Effect of TiN film thickness on crystallite size.

The lattice parameter a of the cubic TiN was calculated using equation (3.2) where d_{hkl} of the (111) plane was calculated from Bragg's equation (3.1). The effect of changing TiN film thicknesses on lattice parameter a are present in Table 4.3. Generally, TiN bulk with a cubic crystal system has lattice parameter of $a = b = c = 0.4240$ nm (PDF Card No: 038-1420). The calculated lattice parameteres of all thickness, ~0.424 nm, were close to that of TiN bulk. This highlights the potential use of this optimised sputtering condition.

Table 4.3: lattice parameter and inter planner spacing d of TiN (111) plane of varying thickness.

TiN film thickness (nm)	Inter-planner spacing "d" (nm)	Lattice parameter of the cubic TiN structure (a=b=c) (nm)
200	-	-
300	0.2422	0.4205
400	0.2451	0.4244
500	0.2454	0.4250
600	0.2451	0.4245
700	0.2447	0.4237

4.7 Effect of thickness on grain size

Figure 4.9 (a)-(b) illustrates AFM images of TiN surface of 300 and 750 nm thickness (deposited for 60 and 135 minutes, respectively) [102]. The 300 nm deposited film exhibited grains with average diameter size of 22 nm, while the 750 nm sputtered film exhibited 60 nm of average grain size [102]. The increase of grain size with thickness could be due to the fact that more atoms were deposited onto the surface, which increased the probability of making bonds with neigbouring atoms.

With regard to the use of TiN film as a nucleation layer for the growth of TiN-NWs, the layer exhibiting smaller grain size as seen in Figure 4.9 (a) would be more suitable for the growth of the nanowires. It has been reported previously that the smaller the diameter of the seeding particle, the higher the density of the grown nanowires, and hence the higher the surface area of the overall structure [117] (however, this will not be investigated in this work). With reference to potential exploitation in neural interfaces, reducing the diameter of the NWs to some degree, whilst maintaining their charge injection capabilities, may be beneficial in limiting the invasive penetration of the cellular walls, which may affect detrimentally the efficacy of the interface with the cells in question.

(a) **(b)**

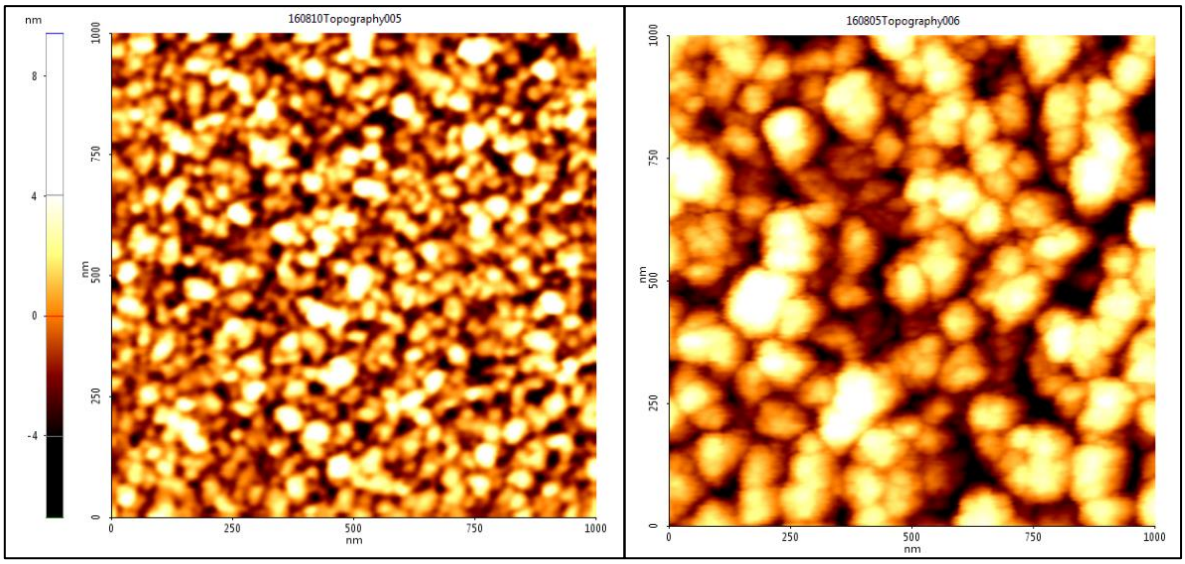

Figure 4.9: AFM Images (1 x 1 μm^2) of TiN film surface deposited at 300 W 80 sccm for a) 1:02 hour and b) 2:15 hours [102].

4.8 Electrochemical test – Cyclic voltammetry (CV)

4.8.1 Effect of Ar Flow rate

To investigate the electrochemical behaviour of TiN films, CV system consisting of a three-body cell1: a Saturated Calomel Electrode (SCE) as a reference electrode, Pt mesh as a counter electrode and TiN as the working electrode (with an area of 1 cm^2), were used. All samples were scanned at a rate of 5 mV/s in a conducting solvent (one tablet of 1/4 Strength Ringers 1007 dissolved in 500 mL of DI water) with an applied potential ranging from -0.6 to 0.6 V versus SCE [102]. To examine the effect of Ar flow rate on the electrochemical behaviour of TiN films, CV of TiN thin films deposited at 300 W, 80 and 10 sccm were measured and their CV curves are presented in Figure 4.10 [102].

The CV shapes seen in Figure 4.10 is indicative of the capacitive behaviour of TiN material. It can be noted that the CV curve of the film sputtered at 80 sccm is enlarged as compared to the film sputtered at 10 sccm, giving capacitance values of 0.0416 mF/cm^2 and 0.029 mF/cm^2, which is equal to a charge injection of 0.021 mC/cm^2 and 0.0145 mC/cm^2, respectively (calculated using equation (3.6) and (4.2), respectively) [102]. Generally, the electrochemical performance of an electrode material depends on the nature, porousity, surface area, crystalline structure and conductivity of the electrode material [118]. Therefore, the enhanced capacitive performance of TiN thin film sputtered at 80 sccm as compared to that of the film sputtered at 10 sccm can be correlated to the higher polcrystalline nature, as seen previously in XRD data, which facilitated the transport of charge carriers [118]. In fact it can be nocited that the cathodic and anodic current of the film sputtered at 10 sccm, shift slightly negatively, this is assumed to be a surface effect due to different orientations of exposed crystal surface [119, 60]. In addition, the surface roughness of the films sputtered at 80 sccm was higher than the film deposited at 10 sccm, as seen in AFM data in Figure 4.6, which provided higher surface area, leading to enhancment of its capacitance [102].

Therefore, from the above, it has been shown that it is important to control the polycrystalline quality of the film, surface area which depends on surface roughness as well as film composition to develop a material with better electrochemical performance which is essential for electrode recording and stimulation. Further electrocheimical invesitgation of the film is conducted in the next section to optimise the electrochemical parameters towards increasing film capacitance as well as testing its stability over number of cycles, in which all could help to mediate the transduction of charge injection capacity through the nanowires.

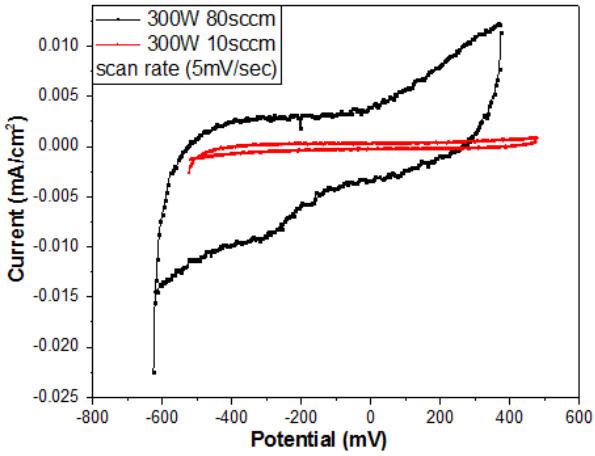

Figure 4.10: CV of TiN (300 nm) for a potential cycling between 0.6 and -0.6 V Versus SCE in Ringer solution at a scan rate of 5 mV/s [102].

4.8.2 Potential limits and scan rate

The CV results in this section were carried out using a BioLogic VMP3 potentiostat for the attempt to improve measurement sensitivity. The set is consisted of a three-body cell; Ag/AgCl as a reference electrode, carbon as counter electrode and TiN film as the working electrode with an exposed area of 1 cm^2. Phosphate buffer saline (PBS) was used as an electrolyte solution (pH=7.4). PBS is commonly used as an electrolyte medium in biology because its osmolarity and ion concentrations usually match those of the human body.

To determine the onset potentials for hydrogen and oxygen evolution, a sweep rate of 50 mV/s was used with initial potential window of -0.4 and +0.4 V. The lower potential limit was further decreased from -0.4 to -0.6 and -0.9 V, while the positive potential limit was increased to 0.6, 0.9 and 1.2 V, see Figure 4.11. It can be seen that cathodic current (at the lower limit) increased when the negative potential limit increased. The increase in the cathodic current can be attributed to the irreversible oxygen reduction reaction due to the presence of O_2 in the solution (equation (3.8)) [120]. However, beyond -0.6 V a significant cathodic current is observed in which it is assumed to be correlated to hydrogen evolution (equation (3.9)) [120].

On the other hand, when the positive potential limit was increased above 0.6 V (Figure 4.11), a clear upturn is observed which correspond to the irreversible anodic oxidation reaction. This increase in current is attributed to oxidation of the electrode material. The irreversible reaction of oxygen reduction, hydrogen and oxygen evolution could potentially degrade the electrode at a long-term cycling experiments as well as harm the surrounded tissue by changing the extracellular pH value. Therefore, from these different observations, potential cycling between -0.4 and +0.6 V appears to be the best suitable cycling conditions to obtain a stable cycling and avoid oxidation of the electrode surface as well as reduction of oxygen or hydrogen evolution.

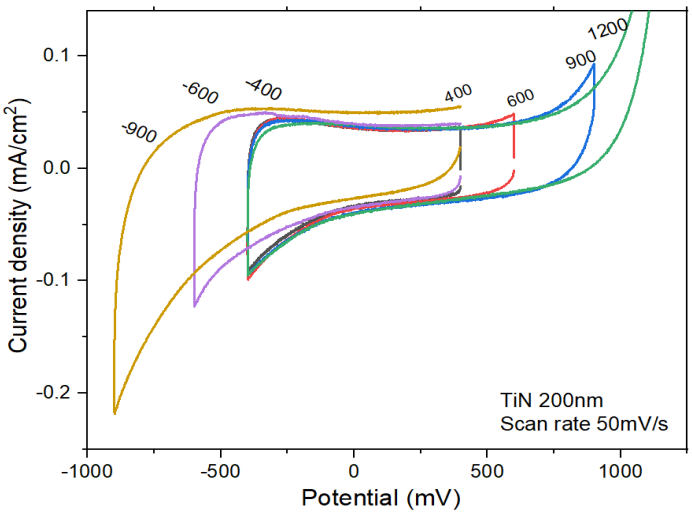

Figure 4.11: CV curve of TiN film (200 nm) between -0.4 and more negative potential, and +0.4 and more positive potentials at a scanning rate of 50 mV/s.

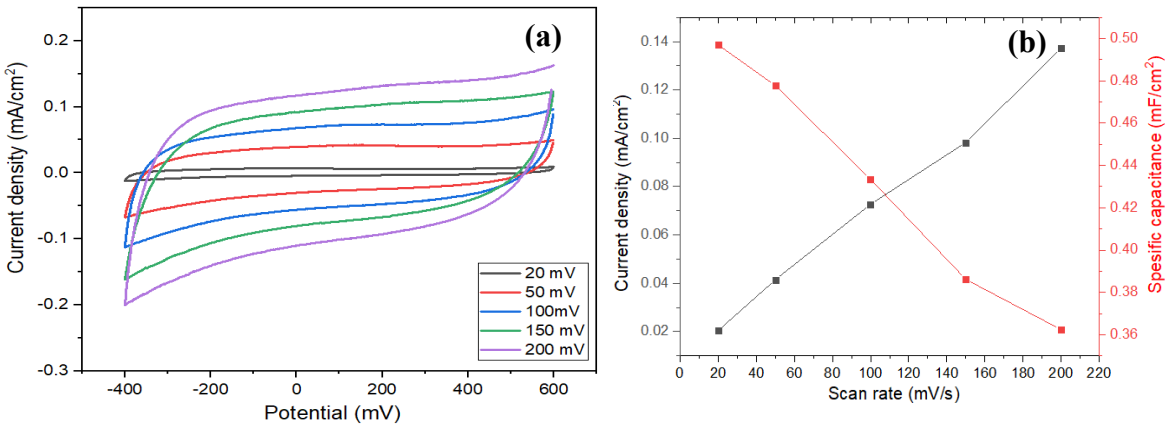

Figure 4.12: (a) CV curve of TiN film (200 nm) cycled at varying scan rates, (b) current density and specific capacitance variation with scan rate.

To investigate the stability of TiN film at different scan rates, CV was performed on a new TiN electrode at 20, 50, 70 and 100 mV/s between potential window limit of -0.4 to +0.6 V (Figure 4.12 (a)). It can be seen that the CV curves of TiN film at all the scan rates exhibited quasi-rectangular shapes, indicating a good capacitive behaviour. Generally, when the electrode material is in contact with the electrolyte, there is a double layer forming near the electrode surface. When a potential is applied, ions of opposite charge to the applied potential diffuse from the solution to near the electrode surface, this form a diffusion layer. This diffusion layer increases in thickness when the scan rate is lower which result into reduction in concentration of newly diffused ions (with reference to the electrode surface), causing reduced current and increase capacitance [40]. The increase in capacitance at low scan rate is attributed to the time given to those ions to diffuse further at the electrode/electrolyte interface [40]. On the other hand, at faster scan rate, the size of the diffusion layer is smaller, as a consequence, higher currents and lower capacitance values are observed. Figure 4.12 (b) shows the decrease in capacitance value with increase of scan rate.

4.8.1 CV Stability performance under nitrogen and air ambient

To further understand the oxidation behaviour of our TiN electrode, the electrolyte solution was saturated with nitrogen gas prior to experiments by bubbling the electrolyte for 40 minutes to replace any dissolved oxygen in the solution. Dissolved oxygen could contribute into the cathodic current at lower potentials by forming oxygen reduction reactions near the electrode surface. In addition, dissolved oxygen could contribute into forming oxide layer onto the electrode surface which could degrade the electrode over cycling. Here, this is investigated by cycling the electrode once under nitrogen ambient and another under air ambient followed by SEM and EDX measurement of the electrode surface to study any change of surface structure and compositions resulted upon cycling.

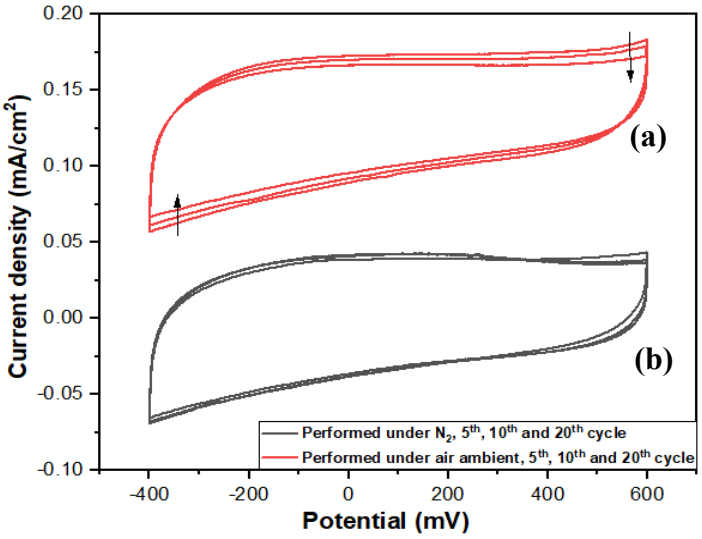

Figure 4.13: CV curve of (a) Electrode cycled under air ambient and (b) electrode cycled under nitrogen ambient.

First to study any differences in CV curves between the two electrodes, Figure 4.13 present the first 5th, 10th and 20th cycles of the two electrodes, one cycled under nitrogen electrolyte saturation and other cycled in an ambient electrolyte between -0.4 V and 0.6 V at a scan rate of 50 mV/s. It can be observed that there is an upturn of the anodic current at the higher potential limit which does not diminishes until around the 20th cycle while the upturn of the electrode cycled under nitrogen ambient diminishes at only the 6th cycle and stabalises over further cycling.

This observations means that there are some oxide growth that may have occurred on the electrode cycled under air ambient and it is much more pronounced as compared to that cycled under nitrogen ambient. The decrease in the anodic oxidation current (of the electrode cycled under air ambient) over cycling, means that the oxide growth diminishes and eventually reaches a stable oxide thickness [56].

However, this is less seen in the CV curve of the electrode cycled under nitrogen ambient in which the anodic current height is smaller and stable over cycling which indicate less pronounced oxide growth. On the other end, oxygen reduction reaction near the electrode cycled under air ambient is seen to contribute into the cathodic current in which it decreases with further cycling, indicating the consumption of the oxygen molecules available for reduction at the electrode surface [56]. This is less observed in the electrode cycled under nitrogen ambient.

The same two electrode were further cycled over 200 cycles to evaluate the electrochemical durability and stability difference between electrode performed under nitrogen saturation and air ambient. Figure 4.14 (a)-(b) shows the 5^{th} and 200^{th} cycle curves of electrode material cycled once under nitrogen saturation and air ambient. Figure 4.15 shows the corresponding capacitance with respect to the cycle number. It is observed that the electrode cycled under air ambient exhibit a slightly higher decline rate of the capacitance over the 200 cycles while the electrode capacitance cycled under nitrogen exhibits a slight decline during the first 25 cycles only and then achieves a steady level. The capacitance retention of electrode cycled under air and nitrogen ambient was about 70% and 85%, respectively after 200 cycles, presenting the comparative stability and durability in a cyclic process. A recent work has reported the cycling stability of as-deposited TiN thin film, through reactive sputtering, over 10,000 cycles showing excellent cycling stability [121]. The work has further annealed the as-deposited film under N_2/argon gas mixture in which its surface capacitance has increased by a factor of 3, giving a value of 8.2 mF/cm^2 without any sacrifice of cycle life. The capacitance improvement was correlated to the doping of TiN surface by the diffusion of nitrogen atoms from the subsurface towards the surface, leading to nitrogen substitution of oxygen in the TiO_x layer that builds up at the surface of TiN layer, hence improving the capacitance [121]. Therefore, the stability of the deposited TiN film can correlated to those nitrogen atoms at the surface that hinder the incorporation of oxygen.

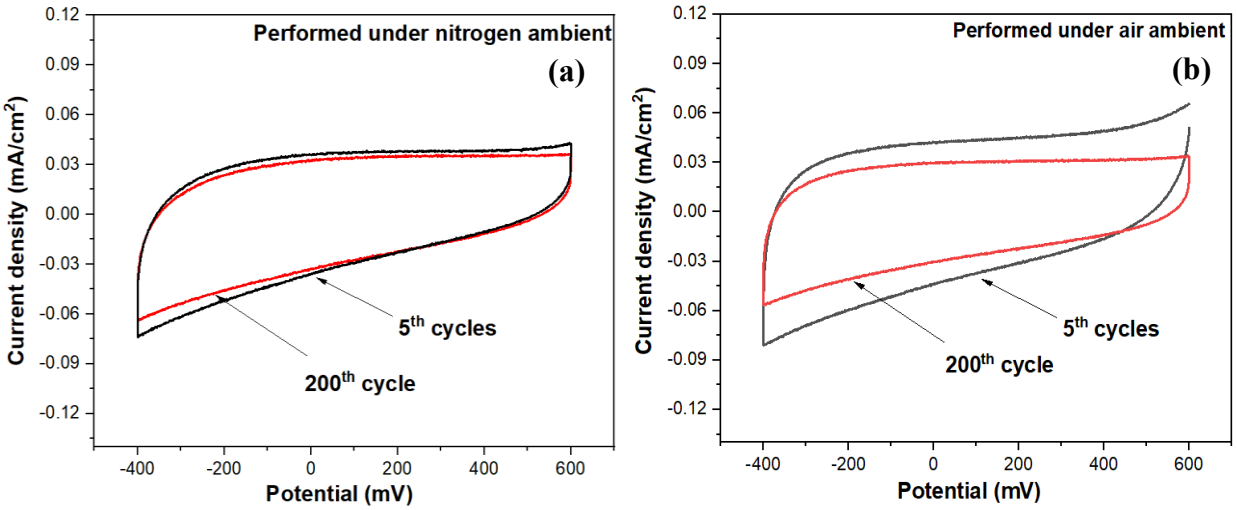

Figure 4.14: The 5th and 200th CV cycle of electrode cycled under (a) nitrogen ambient and (b) air ambient at a scan rate of 50 mV/s.

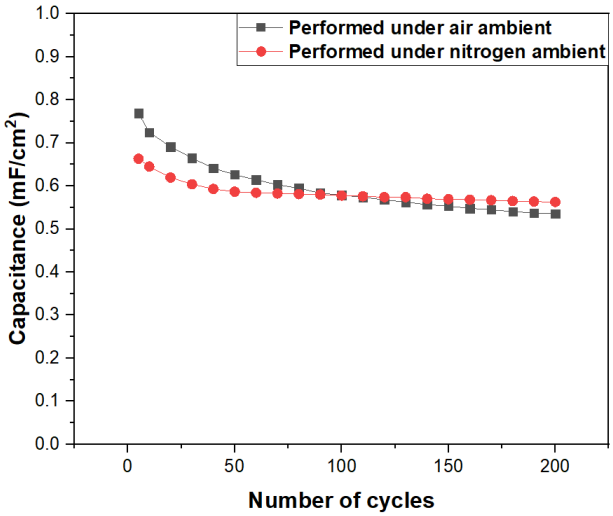

Figure 4.15: Capacitance retention of electrodes cycled under nitrogen and air ambient over 200 cycles at a scan rate of 50 mV/s.

SEM studies of those two electrodes cycled over 200 cycles showed no obvious morphological change, and no cracks in the film surface structure (data not shown). EDX elemental analysis has been performed on each electrode before and after cycling (in air and nitrogen ambient) and it is presented in Table 4.4. It can be seen that there is a slight decrease in the atomic percentage (at.%) of the elements after cycling under both ambient, but the decrease in at.% of the electrode cycled under air ambient is slightly higher. To see if this reduction is of significant as compared to the electrode cycled under nitrogen ambient, an independent-samples T-test (a statistical analysis, not shown here) was used. Obtaining a P-value > 0.05, it can be said that there is no significant change in composition between both electrodes after cycling. However, the small difference in composition seen in Table 4.4 could have been enough to make a difference in the samples' stabilities, which could explain the decline in capacitance of the electrode cycled under air ambient as the growth of oxide layer could act as poor electrical conductivity layer.

The growth of the oxide takes place as oxygen atoms penetrate the surface of electrode and replace the nitrogen atoms [56]. Since this mechanism is irreversible, oxidation of the surface can be carried on until all nitrogen atoms located on the surface/subsurface are replaced and oxide thickness is stabalised resulting in capacitance stabilisation at some point, as seen in Figure 4.15. Although there might have been some oxide growth on the surface of TiN during potential cycling, the capacitance is not so much different from that cycled under nitrogen, suggesting that the oxide thickness is not of significance. It has been suggested that the stability of TiN material lies on the presence of N^{-3} on the surface of TiN which has large electron densities that screens the underlying titanium ions and protects them from oxidation at low applied potentials [122].

Table 4.4: Atomic % of two TiN films before and after 200 cycles, performed under nitrogen and airm ambient.

	Under N_2 ambient		**Under air ambient**	
Sample (S)	**Before cycling**	**After cycling**	**Before cycling**	**After cycling**
At. % of N	**34.51**	**31.08**	**33.39**	**27.65**
At. % of O	**21.27**	**26.10**	**26.84**	**35.88**
At. % of Ti	**40.17**	**37.16**	**36.39**	**30.51**

4.8.2 Effect of sputtering pressure on CV stability performance

Previously in section 5.8.1, electrochemical analysis of the sample deposited at 10 and 80 sccm (sputtering pressure of 4 and 6.5 mTorr) were discussed. Here further analysis is performed on two electrodes of different sputtering pressures, 7 and 8.5 mTorr, and test their stability performance under air ambient. Electrodes were scanned by sweeping the cathodic and anodic potential over 30 cycles at a scan rate of 50 mV/s between -0.4 to 0.6 V (see Figure 4.16 (a)-(b)). The CV curve of the sample sputtered at lower pressure shows excellent cycling stability with almost full capacitance retention, ~0.70 mF/cm^2. A slight increase in the capacitance value of the 5th cycle is due to the contribution of the oxide layer growing at the surface of the electrode which becomes minimum (stabilisation of the oxide layer thickness) as electrode is cycled further. It is suggested that the excellent stability of TiN material and its resistive to further oxidation is maybe be due to the presence of native oxide/oxynitride layer on the surface of TiN which are not-uniformly distributed on the surface which prevent the surface from further oxidation [108, 23]. In addition, the presence of nitrogen (coming from the oxynitride compounds) on the surface of the material provides a large electron density that screens the underlying titanium ions and hence inhibits the oxidation of the material [108, 23].

On the other hand, the CV curve of the sample sputtered at 8.5 mTorr, presented in Figure 4.16 shows less capacitive behaviour with anodic peak appearing at -0.2 V corresponding to oxide/hydroxide growth onto the surface [56]. The shift in peak position indicates an increased overpotential required for the same reactions due to the thickened of the oxide/hydroxide layer [56]. Equation (4.3) and (4.4) show the chemical reactions that result in the formation of oxide and hydroxide titanium [122]. The decrease in the peak height with cycling illustrates film passivation which suppresses the current flow through the film and suppresses any further oxide growth. In addition, as mentioned before that existence of nitrogen ions in the subsurface may screen any further oxidation of the film surface, and so the reason for this electrochemical behaviour of the film sputtered at higher pressure could be due to the increased nitrogen vacancies during sputtering process which act as an attraction site of oxidation reaction.

$$2\,TiN + 4\,H_2O \rightarrow 2\,Ti_2O + N_2 + 8\,H + 8\,e- \quad (4.3)$$

$$TiO_2 + nH + ne- \rightarrow TiO_{2-n}(OH)_n \quad (4.4)$$

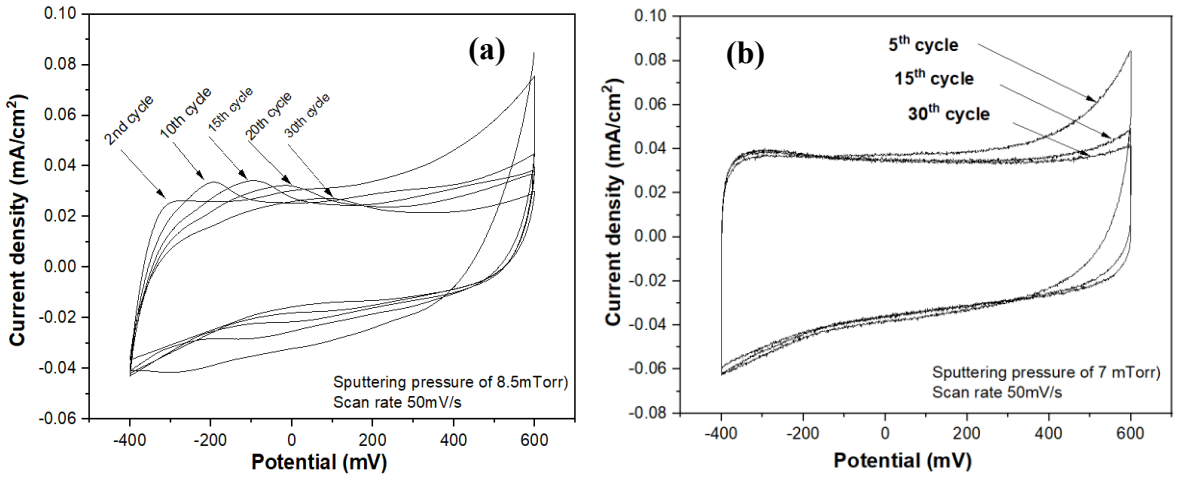

Figure 4.16: CV curves of TiN film (200 nm) sputtered at (a) 8.5 mTorr and (b) 7 mTorr, scanned over 30 cycles at a scanning rate of 50 mV/s.

4.9 Summary

Titanium nitride films were grown using non-reactive sputtering in which RF power and Ar flow rate were optimised towards polycrystalline structure and good electrochemical properties. Structural properties including crystal orientation, polycrystallite and grain size, RMS surface roughness, strain and lattice parameters were studied. The preferred orientation was found to change from (200) to (111) when Ar flow rate increased from 65 to 80 sccm, and changed back to (200) when Ar flow rate was further increased to 95 sccm. Polycrystallite size, grain and surface roughness were greatly influenced by Ar flow rate rather than RF power. By studying the kinetic energy of sputtered atoms and deposition rates, it was realized that relatively higher KE with lower deposition rate can result in crystals oriented in (111) plane and (200) otherwise. Therefore, by tuning the KE and deposition rate through variation of Ar flow rate, one can control the properties of the deposited film. The electrochemical behaviour of TiN films showed superior stability over 200 cycles and a comparable capacitance to that previously reported in literature. Electrochemical performance under nitrogen has shown better stability than the electrode preformed under air ambient in which capacitance retention was higher by 15%. Optimising the electrochemical behavior is essential to achieve a high capacitance as it could also help to mediate the transduction of charge injection capacity. It is believed that TiN-NWs would give further improvement to the electrochemical, mechanical and biocompatibility which could provide a safe stimulation and recording over a long period of time keeping the electrode/neuron interface healthy. This exploration is detailed in Chapter 5.

Chapter 5. Results-Synthesis and characterisation of TiN-NWs

5.1 Introduction

Growing TiN-NWs through a two-step approach has been studied in the literature where TiO_2-NWs are first grown through a solution route followed by annealing at high temperatures (>800°). Here we report a novel nitridation process through PECVD where low temperatures are utilised. The mechanism of nitridation is discussed.

This chapter is divided into two experimental work-steps to grow TiN-NWs; **(1)** *Growing TiO_2-NWs* through hydrothermal solution method at low temperatures (<200˚C). The growth involves the hydrolysis of Titanium (IV) butoxide (as the Titanium source) in hydrochloric acid (HCL) and deionised (DI) water (with resistance of 18.2 MΩ). The growth takes place in a closed system in a stainless-steel autoclave lined with Teflon chamber (25mL). The influences of the growth conditions of the hydrothermal method such as growth temperature, reaction time and seed layer thickness on the morphological and structural properties have been investigated towards finding the optimum growth condition of TiO_2-NWs. **(2)** *Nitridation of TiO_2-NWs under ammonia ambient* at temperature of 600˚C. The process is performed in PECVD which offers a lower activation energy of the reactant gases, promoting surface reaction and allowing nitridation at lower temperatures. Nitridation parameters, such as RF power, chamber pressure, and reaction time were varied to optimise the transformation of TiO_2-NWs to TiN-NWs. The morphological, compositional, structural, and electrochemical properties of the nanowires, examined by SEM, Raman, XPS, TEM, XRD, CV, and EIS, respectively were discussed and part of the analysis were previously reported [123].

Figure 5.1 below shows samples that underwent the synthesis steps to grow TiN-NWs. It can be seen that TiN deposited film exhibits the gold colour which is the typical colour of TiN material. After nitridation of TiO_2-NWs, TiN-NWs exhibit a dark blue colour. It is reported that TiN colours varies from gold for low oxygen contents to dark blue for higher oxygen content, as this will be discussed in this chapter.

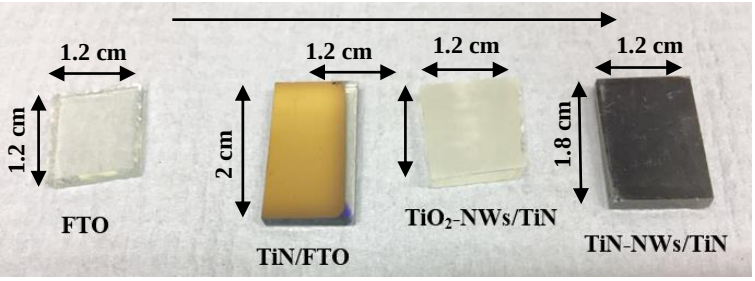

Figure 5.1: Steps taken to grow TiN-NWs, starting from an FTO substrate, deposition of TiN film, growth of TiO_2-NWs, and finally nitridation to obtain TiN-NWs.

5.2 Experimental work of TiO_2-NWs growth

An attempt to grow TiO_2-NWs on TiN/glass as well as TiN/Silicon substrates have been done resulting into nanoflower-type of structure which were randomly oriented with respect to the substrate and nonadherent to the substrate surface (homogeneous nucleation). Therefore, TiN layer sputtered on fluorine tin oxide (FTO) coated-glass was used as a substrate for TiO_2-NWs growth as FTO provided some degree of surface roughness to TiN layer needed for the growth of nanowires. Prior to growth, TiN thin films of different thickness; 50, 100, 200 nm, optimised previously [102], were prepared. The growth solution was prepared by mixing 1 ml of titanium but-oxide (TNB), 30 ml hydrochloric acid (HCl, 37 wt%) and 30 ml deionised water (DI). The mixture was ultrasonicated for 15 minutes until the solution became clear. 12 ml of the mixed solution was transferred to a 25 ml Teflon lined in which the substrates were placed at an inclined angle against the Teflon wall facing downwards. The Teflon lined was sealed with stainless steel autoclave and transferred in an electrical oven. The hydrothermal process was carried out at different temperatures (150, 175, 195˚C) and for different growth time (4, 9 and 18 hours). After synthesis, the autoclave was cooled down to room temperature and the substrates were taken out and rinsed extensively with DI water and Isopropanol and dried with nitrogen gas. The effect of those growth parameters on morphological and structural properties of the grown nanowires were investigated towards achieving relatively high aspect ratio and good crystalline quality.

5.2.1 Effect of hydrothermal growth parameters on morphologhical properties of TiO_2-NWs

To investigate the effect of growth temperature on the morphology, TiO_2-NWs were grown at 150 °C, 175 °C and 195 °C on a 100 nm nucleation layer thickness for 18 hours. Their SEM images are shown in Figure 5.2. It can be noted that an attempt to grow TiO_2-NWs at a temperature below 150 °C has been done, however, no growth of NWs were observed (data not shown). It is suggested that below 150 °C, there might be insufficient thermal energy to facilitate the adsorption of precursor ions on the substrate to form TiO_2-NWs.

At 150 °C, in Figure 5.2, it can be seen that the surface of the substrate is covered with dense NWs exhibiting vertical orientation with respect to the surface. The average length and diameter measured for those NWs were ~1.98 µm and ~150 nm, respectively. At 175 °C and 195 °C we observe no TiO_2-NWs, but TiO_2 multi-layered porous film. The measured thickness of the film at 195 °C is 15 µm with pore size of 2 to 4 µm. Generally, the formation mechanism of a TiO_2 porous film is proposed as two competitive processes; crystallisation and chemical dissolution [126]. In an ideal condition for the growth of NWs, the concentration of Ti^{+4} and OH^- in the solution (generated from the decomposition of TNB and HCL) supersaturates and so they combine to form nuclei. However, at higher temperature, the OH^- concentration, at the beginning of the growth process, is relatively higher which promotes a quick condensation of TiO_2 resulting into a lateral growth or growth of porous films instead of NWs [126]. The high temperature that favours quick condensation with neighbouring particles promote the formation of porous films [127]. The variance in structure as a consequence of growth temperature highlights the potential of this technique to produce bespoke NWs/porous materials for targeted application. In this work, a growth temperature of 150°C is considered as the optimum temperature for the growth of NWs and therefore is used for further analysis.

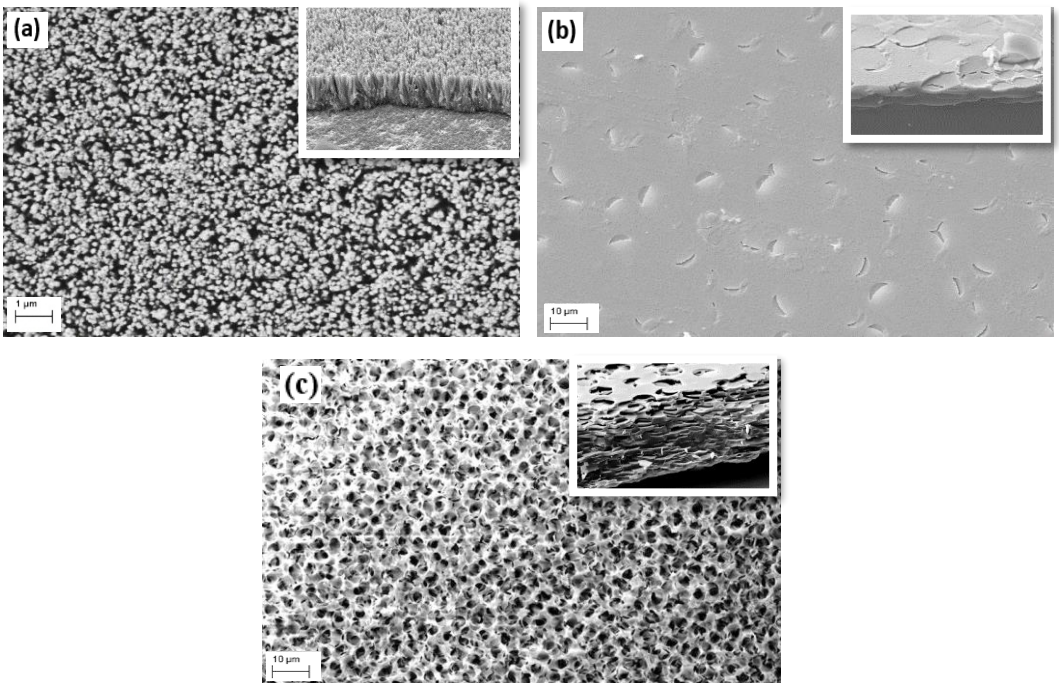

Figure 5.2: SEM images of TiO_2 structure grown at a) 150°C b) 175°C and c) 195 °C for 18 hours on 100 nm TiN thickness.

Since the variation of TiN nucleation layer thickness could affect the length and diameter of NWs, the film thickness is optimised here to grow relatively high aspect ratio of TiO_2-NWs, so the thickness of the nucleation layer was varied from 50, 100 to 200 nm [125]. Plan-view and side-view SEM images (Figure 5.3) of TiO_2-NWs grown on different nucleation layer thicknesses at 150°C for 18 hours reveal dense, uniform and well-aligned vertical NWs with respect to the surface, which suggest the homogeneity in grain distribution of TiN nucleation layer at different thickness [125]. All NWs exhibited the tetragonal pillar structure known for TiO_2 with a flat facet surface (Figure 5.3 (d)). The length and diameter with respect to nucleation layer thickness are plotted in (5.16) [125].

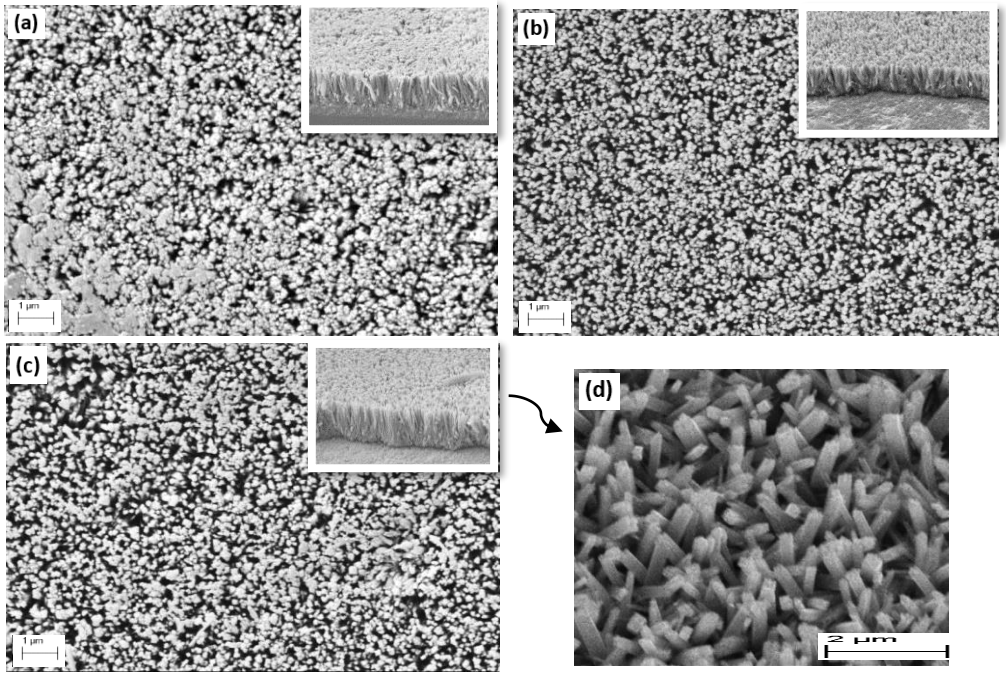

Figure 5.3: SEM images of TiO_2-NWs grown at 150 °C for 18 hours on different TiN film thickness; a) 50 nm, b) 100 nm, c) 200 nm and d) higher magnification of (c) [123].

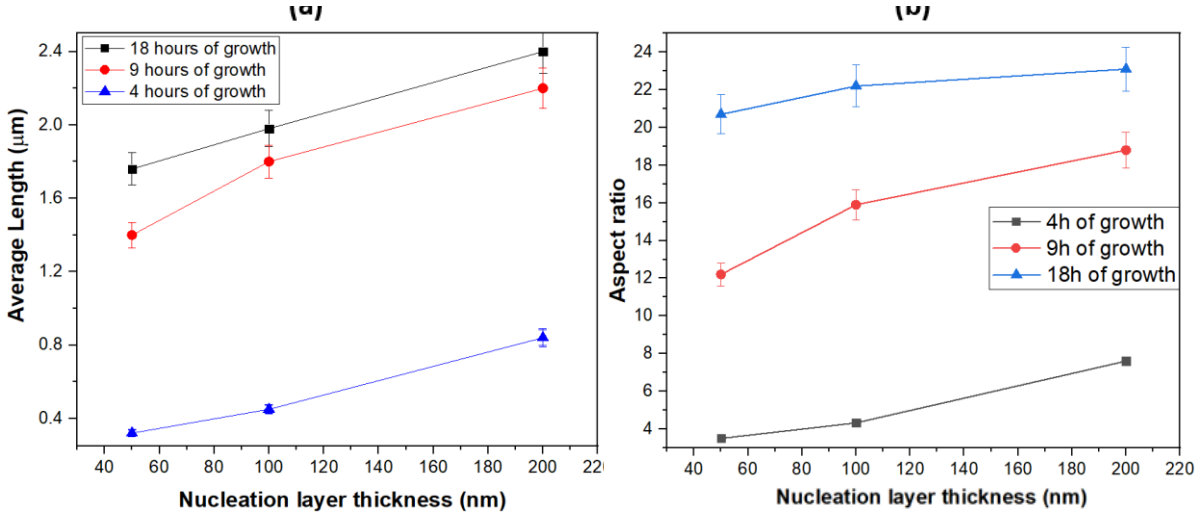

Figure 5.4: (a) Effect of varying TiN film thickness on length of TiO_2-NWs grown at 150˚C, (b) Aspect ratio of the grown NWs on different nucleation thickness and growth time [123].

Figure 5.4 (a) demonstrates that when the nucleation layer thickness increased from 50 to 200 nm, the length of NWs grown for 4 hours increased from 320 nm to 840 nm, while the NWs grown for 9 hours increased from 1.4 to 2.2 µm, and those grown for 18 hours increased from 1.76 to 2.4 µm. On the other hand, when the nucleation layer thickness increased, the diameter of all grown NWs, regardless of growth time, slightly increased from 85 to 109 nm. The increase in length and diameter of the NWs for the same growth time can be associated to the increase of the nucleation layer polycrystallite size with thickness which enhanced the growth of NWs [128] [129] [102].

It is also observed from Figure 5.4 (a) that the increase of growth time from 4 to 18 hours (at 200 nm nucleation layer) resulted in an increase of length from 850 nm to 2.4 µm. SEM images of NWs grown at different reaction time are shown in Figure 5.5. It can be seen that the NWs grown for 4 hours are randomly oriented across the substrate while those NWs grown for longer time are vertically aligned with respect to the substrate surface. Further increase in growth time, resulted in a slight increase of length, illustrating that the NWs tend to saturate around 18 hours, which might have attributed to the decrement in Ti^{+4} and OH^- with increase of growth time. The diameter of the NWs (~109 nm), grown on 200 nm thickness (as well as 50 and 100 nm thickness), seem not to be affected by the growth time.

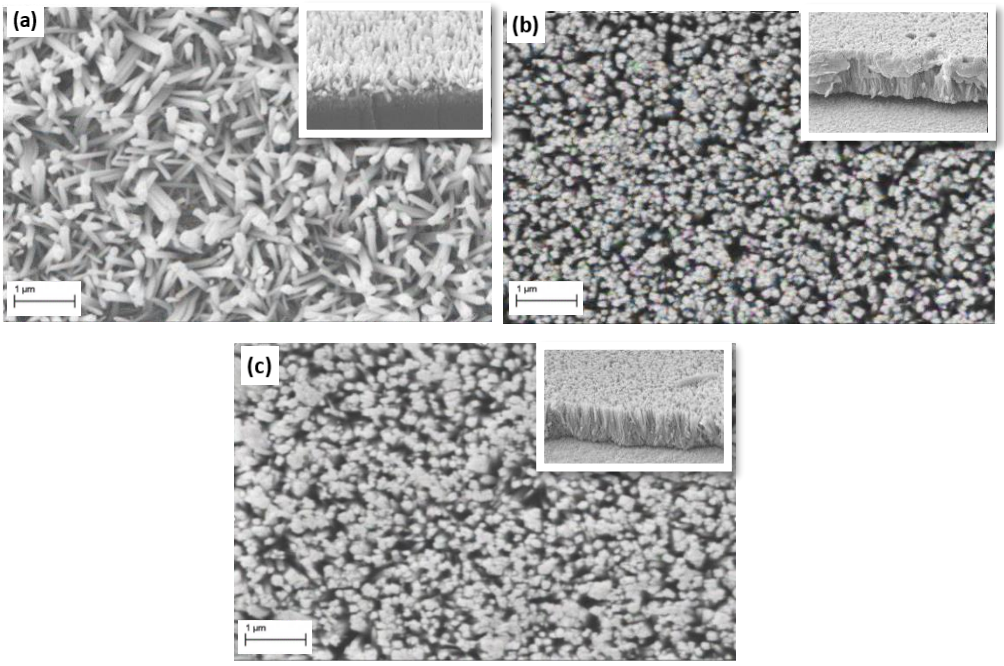

Figure 5.5: SEM images of TiO_2-NWs grown at 150 °C for a) 4 b) 9 and c) 18 hours on 200 nm TiN film thickness [123].

The aspect ratios of NWs grown at different reaction times and on different nucleation layer thicknesses are plotted in Figure 5.4 (b). It can be seen that the NWs grown on a 200 nm nucleation layer for 18 hours obtained the highest aspect ratio of 23.1, higher than the aspect ratio of the one reported in [130] grown at 155 °C for 20 hours, and also higher than that reported in other work [131] [132] [133]. Therefore, it can be concluded that aspect ratio of NWs can easily be tuned by controlling two factors: the growth time and thickness of nucleation layer. It has been claimed that by increasing the aspect ratio of nanostructures, it can enhance their flexibility and results in improvement of cell adhesion and survival, hence improving the recording and stimulation properties of the electrode [134]. A work on cellular-interfacing ultilising high aspect ratio (21.7) silicon nanowires showed that due to the relatively high bending level of the NWs, the cell traction force on the nanowires (the force generated when cell migrates) was minimised [135], consequently increasing the accuracy of the cellular measurements [26]. However, further increase in NWs aspect ratio could lead to inflammatory response [136]. A work has studied the effect of varying the length of gallium phosphide (GaP) nanowires, on inflammatory response in the brain [136]. The length was varied at 2, 5 and 10 µm while maintaining a diameter of 80 nm. It was found that the 2 µm NWs did not cause significant inflammatory response nor significant loss of neighbouring neurons as compared to 5 and 10 µm. It was suggested that relatively high aspect ratio NWs with length equal to or greater than the size of immune cells can cause inflammatory response. This is because the nanowires become detectable by the immune cells [136]. Therefore, in this work, the grown TiO_2-NWs with length of 2.2 to 2.4 µm and diameters of between 85 to 109 nm could be of suit to the proposed application.

5.2.2 Effect of hydrothermal growth parameteres on structural properties of TiO_2-NWs

Figure 5.6 shows XRD patterns of (a) TiN on glass (200 nm), (b) FTO on glass, (c) TiN sputtered on FTO and (d) TiO_2-NRs (grown for 18 hours on 100 nm thickness). It can be noted that due to the influence of FTO layer underneath TiN layer, the film is only oriented in (200) plane. Pattern (d) shows strong TiO_2 peaks observed at 2θ of 36.14° and 62.81°, assigned to the (101) and (002) planes respectively, while other rutile peaks are observed at 2θ of 27.4° (110), 69.0° (301) and 69.8° (112) (PDF Card No.02-0494).

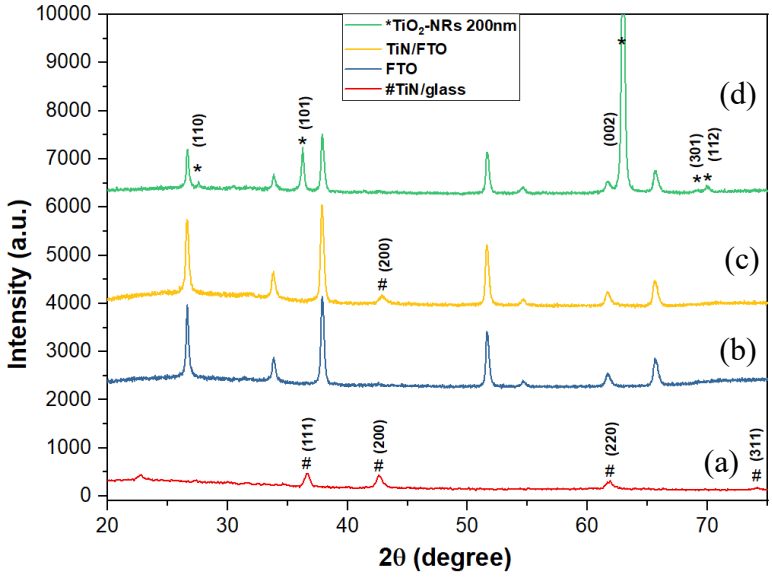

Figure 5.6: XRD pattern of a) TiN/glass, b) FTO, c) TiN/FTO and TiO_2-NRs on TiN/FTO.

To investigate the effect of the growth time and nucleation layer thickness on the crystallinity of the grown TiO_2-NWs, XRD diffraction pattern of the NWs grown at varying growth times and nucleation layer thicknesses were obtained and are presented in Figure 5.7 and Figure 5.8, respectively. From Figure 5.7, the diffraction peaks of NWs grown for 18 hours (on 200 nm) show clear increase in peak intensities of (101) and (002) planes as compared to that grown for 9 hours, which indicates an improvement in polycrystalline quality. The increase of polycrystallinity with increase of growth time could be because Ti and O atoms re-arrange themselves into optimum sites/or come out to the solution, increasing film polycrystallinity.

Figure 5.8, on the other hand, shows that TiO_2-NWs grown on 200 nm nucleation layer thickness exhibits relatively higher polycrystalline structure as compared to 50 and 100 nm thicknesses, due to the increase in their diffraction peak intensities. It can be observed that as the nucleation thickness increased, the intensity of (002) peak gradually increased while the (101) peak slightly decreased. Since (002) and (101) peaks reflect the axial (or the *c*-axis which is perpendicular to the substrate surface) and lateral directions (the direction in which NWs diameter grow into) respectively, an increase in the intensity of (002) indicates preferential growth along the c-axis, due to the lower surface energy, while a decrease in the intensity of (101) represents a slow growth in the lateral direction [137]. Therefore, as seen before, when film thickness increased. the growth rate of NWs lengths were much higher compared to the diameter.

The lattice parameters of the tetragonal phase of TiO_2-NWs (of all thickness) and the interplanar d-spacing for (002) plane (calculated using equation (3.3)) were a = b = 4.576 Å, c = 2.943 Å and d = 0.2422, respectively. The calculated lattice parameters are close to the bulk value of the material (a = b = 4.580 Å, c = 2.950 Å, PDF Card No. 00-002-0494,).

From the SEM and XRD results above, TiO_2-NWs grown at 150 °C for 18 hours at 200 nm seed layer showed the highest aspect ratio as well as higher polycrystalline quality. Hence those NWs grown at these conditions will be further used for nitridation process.

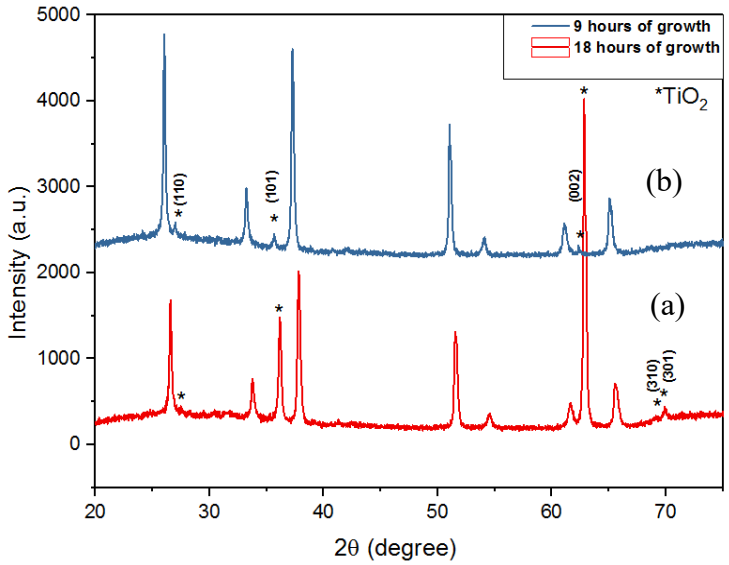

Figure 5.7: XRD pattern of TiO_2-NWs grown at 150 ℃ for 9 and 18 hours [123].

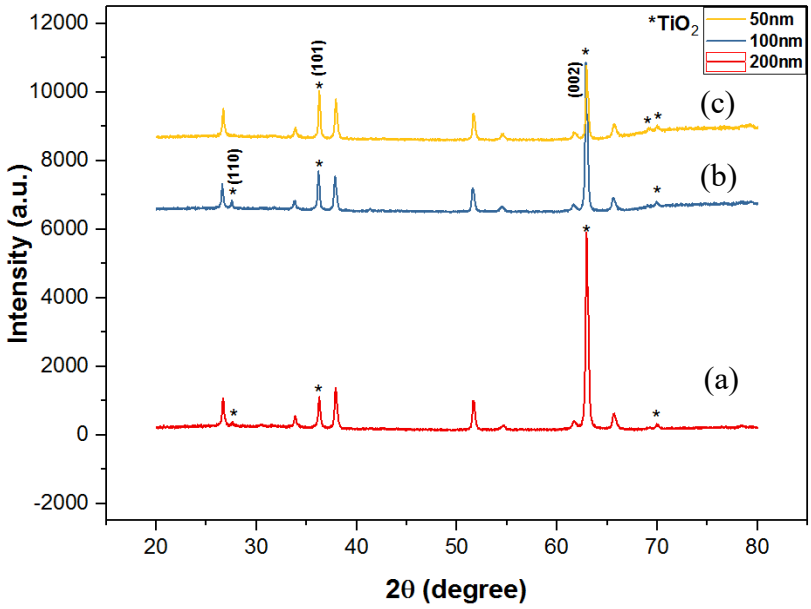

Figure 5.8: XRD pattern of TiO_2-NWs grown on TiN film of varying thicknesses; a) 200, b) 100 and c) 50 nm [123].

5.3 Experimental work for TiO_2-NWs nitridation

RF-PECVD system (Oxford Plasma Lab 100; 13.56 MHz, performed at KAUST) was utilised with ammonia (NH_3) gas as a nitrogen source to nitride TiO_2-NWs at a base pressure of 2.7 $x10^{-6}$ Torr. The gas flow rate was controlled by MFC and all the samples studied were nitrided at a constant NH_3 flow rate of 100 sccm, which was the maximum flow rate in the system, to maximise availability of nitridation species.

In order to convert TiO_2-NWs into TiN-NWs, PECVD is able to generate the required reactive species at lower temperature for nitridation [138]. Due to the high KE of electrons in the plasma, electrons collide with NH_3 molecules causing ionisation and dissociation reactions, resulting in the generation of free radicals and ions, such as NH_x^+, and hydrogen and nitrogen atoms. The following possible reactions may occur in the plasma [139];

Possible reactions for the generation of NH_3^+:

$$NH_3 + e^- \rightarrow NH_3^+ + 2e^- \quad (5.1)$$

Possible reactions for the generation of NH_2^+:

$$NH_3 + e^- \rightarrow NH_2^+ + \mathrm{H} + 2e^- \quad (5.2)$$

$$NH_2 + e^- \rightarrow NH_2^+ + 2e^- \quad (5.3)$$

Possible reactions for the generation of NH^+:

$$NH_3 + e^- \rightarrow NH^+ + \mathrm{H_2} + 2e^- \quad (5.4)$$

$$NH_2 + e^- \rightarrow NH^+ + \mathrm{H} + 2e^- \quad (5.5)$$

$$\mathrm{NH} + e^- \rightarrow NH^+ + 2e^- \quad (5.6)$$

Possible reactions for the generation of N^+:

$$NH_3 + e^- \rightarrow N^+ + 3\mathrm{H} + 2e^- \quad (5.7)$$

$$NH_2 + e^- \rightarrow N^+ + \mathrm{H_2} + 2e^- \quad (5.8)$$

$$\mathrm{NH} + e^- \rightarrow N^+ + \mathrm{H} + 2e^- \quad (5.9)$$

$$\mathrm{N} + e^- \rightarrow N^+ + 2e^- \quad (5.10)$$

while NH_2, NH and N_2 radicals can be generated by direct thermal decomposition or via collisional dissociation of the parent NH_3;

$$NH_3 \rightarrow NH_2 + H \quad (5.11)$$

$$NH_2 \rightarrow NH + H \quad (5.12)$$

$$2\mathrm{NH} \rightarrow N_2 + H_2 \quad (5.13)$$

The highly active $NH_{x<3}^+$ and N_x^+ ions and radicals, e.g. NH_X and $N_{x<2}$, are believed to be responsible for the nitridation. In fact the nitridation mechanism can occur in two different ways or both together: (1) through bombardment of $NH_{x<3}^+$ and N_x^+ onto the material and (2) through surface adsorption of NH and N radicals. Due to the potential difference built up between the plasma and the electrode (the anodic sheath), the highly active $NH_{x<3}^+$ and N_x^+ ions would accelerate and bombard the metal oxide surface with sufficient energy breaking the chemical bond of O-Ti-O through energy transfer and leaving behind the highly active Ti^{+3} ions and two oxygen atoms (O_2^{-2}). Together with the elevation of substrate temperature and the energy transferred from those ions, nitrogen species gain enough energy to form the triple bond with titanium forming TiN. Oxygen molecules released from the metal oxide surface bond with H atoms forming H_2O which can be swept away by the plasma. The following reaction illustrate this process [140];

$$3TiO_2 + 4NH_3 = 3TiN + 6H_2O + 1/2N_2 \quad (5.14)$$

The other way of achieving nitridation is through surface diffusion. According to DL. Douglass [141], there are two main steps to achieve nitridation;

(1) TiO_2 is rapidly reduced or dissociated by ammonia gas into TiO which lead to a loss of an oxygen atom. It is known that titanium atom gives two electrons each to two oxygen atoms to form the partially ionic/covalent bond with the oxygen atoms, therefore titanium loses 4 electrons (hence, Ti^{+4}). When one of O-Ti-O bond is broken, an electron is gained by the titanium (perhaps from the oxygen atom that was set free), therefore, reducing TiO_2 to Ti^{+3} and forming TiO. The reduction reaction by ammonia gas can be expressed as follow;

$$TiO_2 + \frac{2}{3}NH_3 = TiO + H_2O + \frac{1}{3}N_2 \quad (5.15)$$

However, the above reaction does not occur directly, instead it occurs after many reduction steps of TiO_2, and reduction from one oxide to a lower oxide. After going through a sequence of complex oxide structures, the Face-centered-cubic phase of TiO is formed.

(2) The second step is the formation of the nitride as the product of the reaction of TiO with ammonia;

$$TiO + NH_3 = TiN + H_2O + \frac{1}{2}H_2 \quad (5.16)$$

Equation (5.16) simply occurs by the exchange of oxygen in TiO with nitrogen atoms through the diffusion of nitrogen species into the material, forming the cubic faced TiN structure. Another paper supported the argument above in which it has found that the reaction of TiO_2 with ammonia produces TiO as an intermediate phase before forming TiN [142]. Figure 5.9 summaries the nitridation steps.

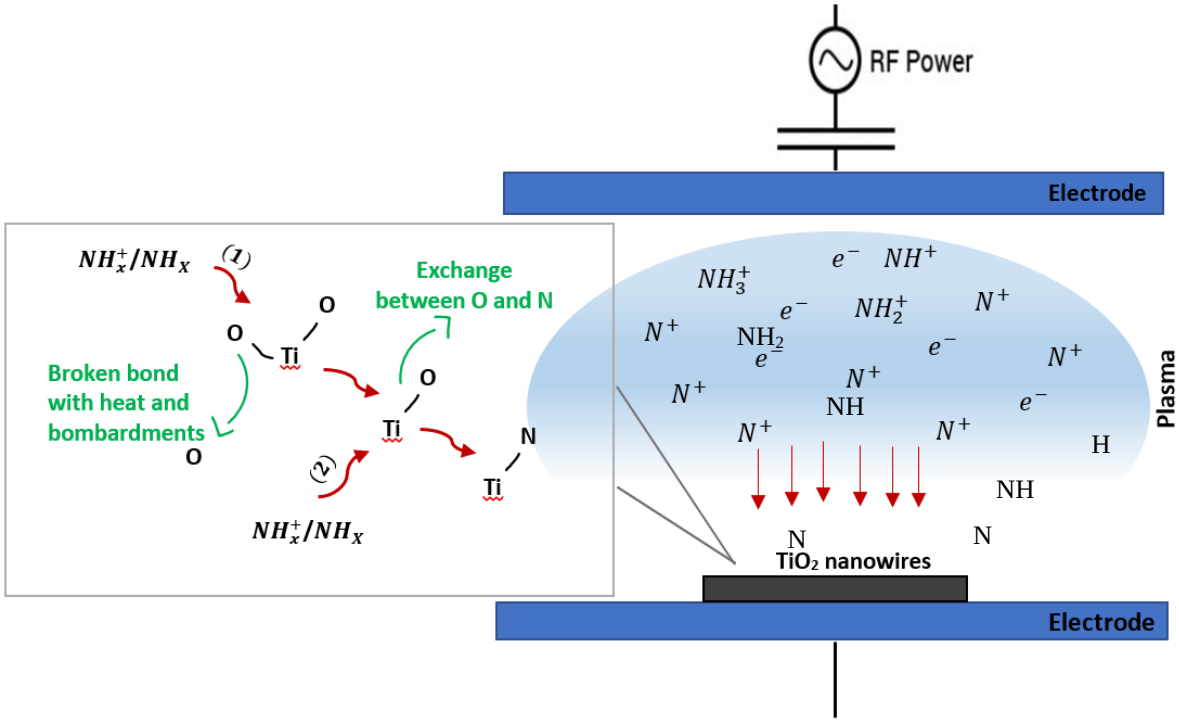

Figure 5.9: Schematic diagram showing plasma nitridation process.

The advantages of using plasma nitridation over a high thermal budget process are the energetic species that cause dissociations of the process gas thereby lowering the substrate temperature required, as well as preparing the sample surface for chemical reactions needed for nitridation through ion bombardment onto the substrate surface. Nitridation through a purely thermal process proceeds by the diffusion of nitrogen molecules only requiring elevated temperatures for the nitridation to occur. In plasma nitridation, the chemical and energetic state of ions and radicals and their concentration can be controlled by plasma parameters, such as RF power, chamber pressure. This cannot be performed by conventional nitridation methods.

DOE methodology was used to optimise the nitridation process with three to four levels resolution. The DoE can be summarised in Table 5.1. RF power was set at 50, 100 and 150 W, giving power densities of 0.15, 0.32 and 0.47 W/cm^2, respectively, while chamber pressure was varied at 300, 500, 900 and 1400 mTorr, for a process time ranging from 0.5 to 3 hours. All the experimental runs (noted as R_X) listed in table A1 in the appendix. The samples were first pre-heated to the desired temperature for 10 minutes then ammonia gas flowed into the chamber for the nitridation step. After the process is done, plasma was deactivated and the samples were allowed to cooldown to room temperature under the flow of ammonia. The samples were then taken out from the chamber, placed in a sealed box flushed with nitrogen gas to minimise samples oxidation or contaminants before

being used for further characterisation. A change of sample colour from white to dark-green was observed after nitridation.

Table 5.1: DOE of nitridation process [125].

Parameters	Level 1 (Min)	Level 2	Level 3	Level 4 (Max)
Power (W)	50	100	150	-
Pressure (mTorr)	300	500	900	1400
Duration (hour)	0.5	1	-	3

5.3.1 Compositional analysis

The compositional and structural properties of TiO_2-NWs nitrided at various process parameters were studied towards finding the optimum parameters for effective conversion to TiN-NWs [125]. This was done by varying the RF power, reaction time, chamber pressure and substrate temperature. Raman spectroscopy (conducted at Nanotechnology and research centre at KAU), XPS and TEM (conducted at KAUST), as well as XRD were employed to examine the effect of nitridation. SEM images of the nitrided NWs were examined (shown in Figure B1 in Appendix) in which no morphological changes were seen, illustrating structural robustness [125].

5.3.1.1 Varying RF power

Initial attempt to nitride the NWs at substrate temperatures below 600 °C while varying RF power, chamber pressure and time (R_1 to R_{10}) were employed in which no sign of nitridation by visual change in sample's coulor or by XPS measurements were seen (data not shown). Maintaining a substrate temperature of 600 °C, chamber pressure of 500 mTorr, while varying RF power at 50 (R_{11}), 100 (R_{12}) and 150 W (R_{15}) for a reaction time of 1 hour were employed in which some sign of plasma nitridation were seen by Raman and XPS measurements. Figure 5.10 presents Raman spectroscopy of the previously sputtered TiN film, the as-grown TiO_2-NWs and the NWs nitrided at varying powers. The characteristic peaks of TiN material can be seen at 200 - 350 cm^{-1} and 500 - 700 cm^{-1}, which can be fitted with three Lorentain peaks at around 208, 319 and 580 cm^{-1} that are related to the transverse acoustic (TA), longitudinal acoustic (LA) and transverse optical (TO) modes, respectively [141]. On the contrary, the as-grown TiO_2-NWs have three Raman-active vibrational modes at 234, 446, and 609 cm^{-1} in which all are attributed to rutile phase [141]. After

plasma nitridation, it could be observed that all the three rutile peaks of the nitrided NWs have decreased in intensities [123]. This illustrates some structural changes within the NWs lattice arrangements, i.e. oxygen disorder in the TiO_2-NWs or incorporation of nitrogen atoms (N). It is noted that as RF power increased, the peak intensities decreased which suggests that there might be a relatively higher ion bombardment onto the sample's surface with increasing power, leading to a greater lattice dislocation or/and incorporation of nitrogen atoms into the TiO_2 lattice. Additionally, there was a noticeable shift in the peaks of the nitrided NWs, as compared to the as-grown sample, towards lower wavenumbers. It is acknowledged that the shift in Raman peaks towards lower or higher wavenumber is linked to the change of chemical bonds of molecules [142]. A shift to a lower wavenumber demonstrates the formation of a longer bond length, while the shift to a higher wavenumber demonstrates the formation of a shorter bond length. Indeed, Ti-O bonds have a length of 1.96 Å whereas Ti-N bonds are 2.12 Å long [142]. Therefore, the observed shift of the nitrided NWs towards lower wavenumber indicates that Ti-O bonds were being replaced with nitrogen atom, forming a longer bond with titanium atoms. However, as stated elsewhere [142] the increase of bond length can also be correlated to the intermediate formation of Ti-O-N. While structural changes of nitrided NWs were seen by Raman, the results did not provide enough evidence for the formation of TiN material. Similar Raman results were reported upon nitridation by other researchers at temperatures above 600 °C [143, 144, 112].

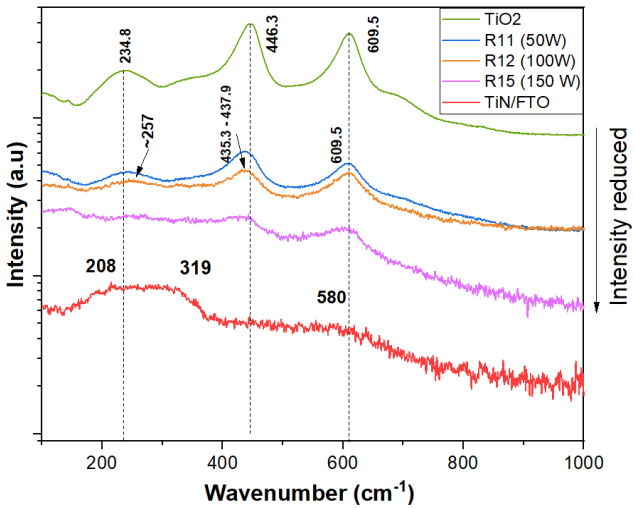

Figure 5.10: Raman spectra of TiN/FTO, TiO_2-NWs nitrided at 50, 100, 150 W and as-grown TiO_2-NWs for comparison [123].

The high resolution XPS spectra for Ti 2p (470-450 eV), N 1s (402-392 eV) and O 1s (550-525 eV) core levels of the nitrided NWs at various powers were measured and are presented in Figure 5.11. The index figures are spectrums of R_{12} fitted with sub-peaks, using CasaXPS software, to acquire elemental information such as peak position and atomic percentage (at.%). Spectrum (a) shows Ti 2p region of the as-grown TiO_2-NWs which form Ti $2p_{3/2}$ part of a doublet with accompanying Ti $2p_{1/2}$ lines located at 458.7 eV and 464.4 eV, respectively, referring to Ti^{+4} phase of TiO_2 material [111]. N 1s region of the as-grown TiO_2-NWs (top right corner of spectrum (a)) illustrates a low intensity peak at 399 eV, which attributes to absorbed nitrogen originated due to atmosphere exposure [111].

On the other hand, spectrum (b) shows the Ti 2p regions of the nitrided NWs. At a power of 50 W, the spectrum exhibited no nitrogen-bond type, whereas N 1s region (spectrum c) showed relatively low peak intensity positioned at 397.8 eV and ~396.6 eV, attributed to TiN and titanium oxynitride (TiO_xN_y). It is suggested that a power of 50 W may not have produced sufficient reactive species, e.g. N and NH_x ions [142], or it was deficient to promote intense surface bombardment needed for the replacement of nitrogen atoms.

On the contrary, it seems that the increase in nitridation power at 100 and 150 W led to a greater reduction in TiO_2 peaks and the appearance of two new peaks at lower binding energies of 455.2 and 457.2 eV, assigned to TiN (Ti^{+3}) and TiO_xN_y (Ti^{+2}), respectively [112, 113, 114, 123]. Additionally, N 1s core level of those samples demonstrates an increase of the peaks at ~397.8 eV and ~396.6 eV, assigned to TiN and TiO_xN_y, while the peak positioned at ~399.2 eV is assigned to absorbed nitrogen or NH_3 (interstitially incorporated) [145, 146, 114, 113]. Moreover, from the O 1s region (spectrum d) of the nitrided samples, it is seen that the peak at ~530 assigned to O – Ti peak in TiO_2 lattice decreased with increase of RF power, while the peak at ~532 eV assigned to O – N peak and belonging to TiO_xN_y, became pronounced upon nitridation, illustrating the exchange of oxygen with nitrogen atoms. An interesting observation related to the decrease of O – N peak with increase of power can be attributed to the higher energy of bombardment ions that decrease the formation of TiO_xN_y and hence perhaps increase the amount of TiN.

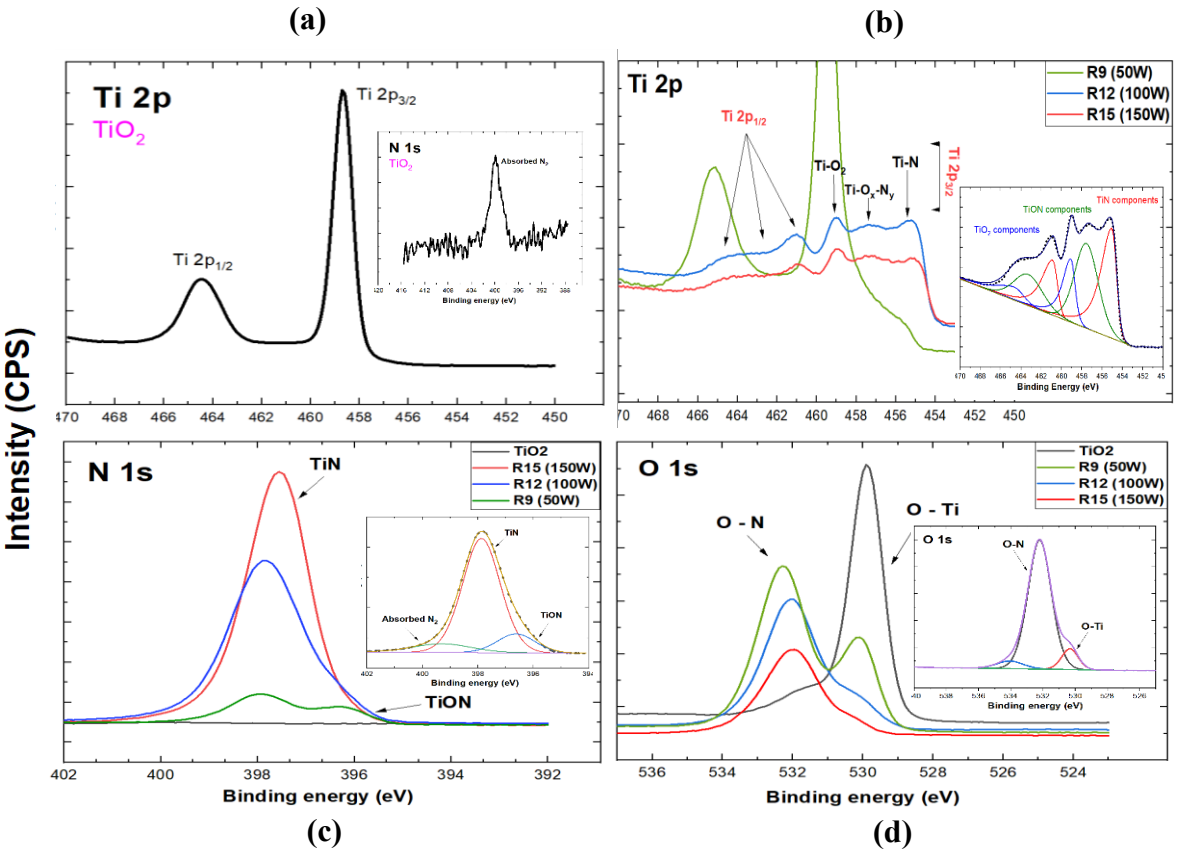

Figure 5.11: XPS of (a) TiO_2-NWs, TiO_2-NWs after nitridation at different powers; 50, 100, 150 W for (b) Ti 2p, (c) N 1s and (d) O 1s core levels [123].

Using CasaXPS software, the binding energies of Ti $2p_{3/2}$ elements (Ti-N, Ti-O-N and Ti-O) of all nitrided NWs, with their relative peak areas (in count per second (CPS)), are summarised and compared in Table 5.2. In addition, the nitrogen at.% of the three elements (Ti-N, Ti-O-N, and absorbed N) presented in N 1s core level for each nitrided NWs are obtained and summarised in Table 5.3. Since the peak area of the element in the core regions is proportional to the number of atoms presented in the specimen, a reasonable comparison between different nitrided samples can be done. Therefore, from Table 5.2, it can be noticed that the peak areas of the three elements of the NWs nitrided at 150 W significantly decreased as compared to those of the NWs nitrided at 100 W, i.e. peak area reduction by 40% is observed for the Ti-N. In contrast, from Table 5.3, the nitrogen at.% in Ti – N peak element in the N 1s regions of 50, 100 and 150 W nitrided NWs gradually increased from 3%, 19% to 30%. This could be due to the fact that when RF power increases, the hot electrons gain more kinetic energy which cause a higher ionisation and dissociation of the gas molecules through collisions, providing increased reaction products (e.g. NH_x, N) needed to promote NWs nitridation [123].

However, the decrease of Ti $2p_{3/2}$ elements with increase of power, (in case of 150 W), could be attributed to the effect of etching of the NWs surface due to the higher energy ion bombardment, which could also create defects and vacancies in the titanium lattice structure [123]. Therefore, the decrease of titanium elemental peaks, while the increase in nitrogen at.% could suggest that the nitrogen radicals had more active sites (which were created with the high ion bombardment causing defects and dislocations) to react with [147]. Another explanation to this behaviour could be attributed to the relatively higher power forcing those nitrogen radicals to be adsorbed at the substrate surface, and with the aid of energy that these bombardment ions create, those nitrogen radicals diffuse into TiO_2 lattice structure substituting the oxygen vacancy and interstitially occupying the site [148]. The stoichiometry of TiN_x of the 100 and 150 W nitrided NWs were calculated as x=0.45 (titanium rich) and x= 2.5 (nitrogen rich), respectively.

Hence, from the results above, NWs nitrided at 100 W is chosen as the optimum power for giving satisfactory elemental compositions as well as stoichiometry [123]. A work has reported the nitridation of TiO_2 nanofibers at relatively high temperature of 1000 °C for 10 hours in which TiN stoichiometry of 0.47 was obtained [27]. This suggests that this work can offer the ability to tune out the N/Ti by varying the RF power while keeping the nitridation temperature low.

Table 5.2: Ti $2p_{3/2}$ binding energies and relative area counts of different titanium environments obtained by modelling the 2p region of the XPS spectra of the samples nitrided at a power of 100 and 150 W at 500 mTorr and 600 °C [123].

Binding energy (100 W)	Area (CPS)	Binding energy (150 W)	Area (CPS)	Peak bond attribution
455.0 eV	18,438	454.8 eV	11,032	Ti – N (substitutional N)
457.5 eV	18,203	457.3 eV	11,723	Ti – O – N (Interstitial N into TiO lattice)
459.0 eV	8,333	458.2 eV	6,681	Ti – O (TiO_2 lattice)

Table 5.3: N 1s binding energies and at.% of different nitrogen environments obtained by modelling the N1s region of the XPS spectra of the samples nitrided at a power of 100 and 150 W at 500 mTorr and 600 °C [123].

Binding energy (50 W)	Atomic %	Binding energy (100 W)	Atomic %	Binding energy (150 W)	Atomic %	Peak
397.9 eV	3 %	397.8 eV	19 %	397.5 eV	30 %	Ti – N (substitutional N).
396.3 eV	2 %	396.6 eV	13.9 %	396.5 eV	0.5 %	Ti – O – N (Interstitial N into TiO lattice).
399.0 eV	0.6 %	399.2 eV	2.9 %	399.1 eV	7.1 %	Absorbed N_2 or N – H from NH_3.

5.3.1.2 Varying nitridation time

To optimise the nitridation time required to effectively convert TiO_2-NWs into TiN-NWs, time was varied from 0.5 (R_{13}), 1 (R_{12}), and 3 hours (R_{14}), while power, pressure, and temperature were kept constant at 100 W, 500 mTorr, and 600 °C, respectively. Raman spectra of those nitrided NWs are presented in Figure 5.12. 30 minutes of nitridation did not seem to have a huge change in the material in which the Raman peaks only slightly decreased in intensity as compared to that of TiO_2, which indicates the incomplete nitridation process due to the short exposure time of the substrate surface to nitrogen species (this result is consistence with XPS data, discussed next).

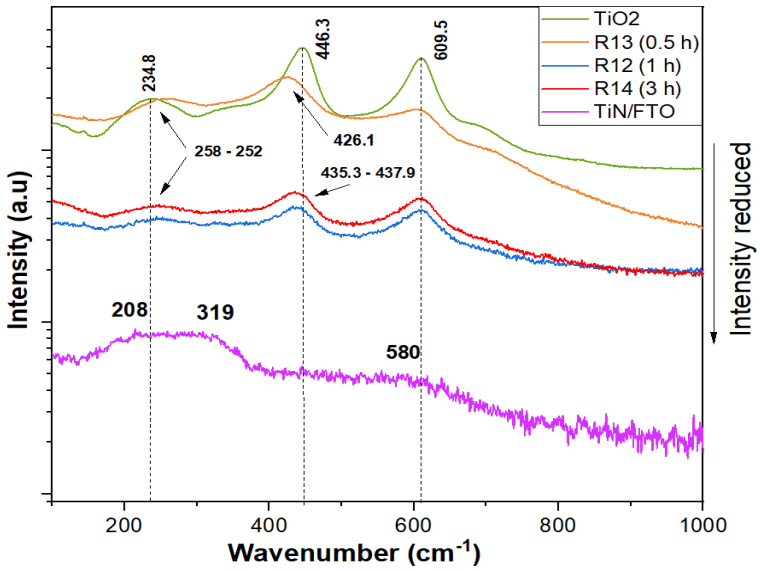

Figure 5.12: Raman spectra of TiN/FTO, TiO_2-NWs nitrided at 0.5, 1 and 3 hours and the as-grown TiO_2-NWs is shown for comparison [123].

The high resolution XPS spectra of Ti 2p, N 1s and O 1s regions of the NWs nitrided at 0.5, 1 and 3 hours are presented in Figure 5.13. From Ti 2p, spectrum (a), it could be observed that the TiO_2 doublet peaks are still pronounced in the NWs nitrided for 0.5 hour with a very small area portion of TiN (10%) and oxynitride (28%) located at lower binding energies which show the incomplete nitridation process. N 1s (spectrum b) and O 1s (spectrum c) further showed that the nitrogen fraction in TiN peak centered at 397.8 eV is relatively lower as compared to the other nitrided NWs, while the fingerprint of TiO_2 peak is still pronounced in the O 1s state. On the contrary, increasing the nitridation time to 1 hour, increased the peak intensity of TiN and titanium oxynitride, nonetheless further increase in time (3 hours) almost diminished all Ti 2p peaks. In fact, TiN peak doublet areas reduced by 69% as compared to the 1 hour nitrided sample. From Table 5.4, the nitrogen at. % of NWs nitrided at 1 and 3 hours were almost equal in amount. A possible explanation could be that at a nitridation time of 1 hour, sufficient amount of oxygen atoms are replaced by nitrogen atoms in the TiO_2 lattice in which for a longer nitridation time, no exchange of oxygen with nitrogen occurred (hence same at. % of nitrogen is seen). In fact titanium ions might have escaped from the lattice (or sputtered out) due to the continues exposure of ion bombardments and this could explain the reduction in the Ti 2p peaks for the sample nitrided for 3 hours.

From the result above, it was concluded that that 1 hour was enough to nitride the sample effectively. Therefore, 1 hour of nitridation was considered as the optimum time and was used for further optimisation.

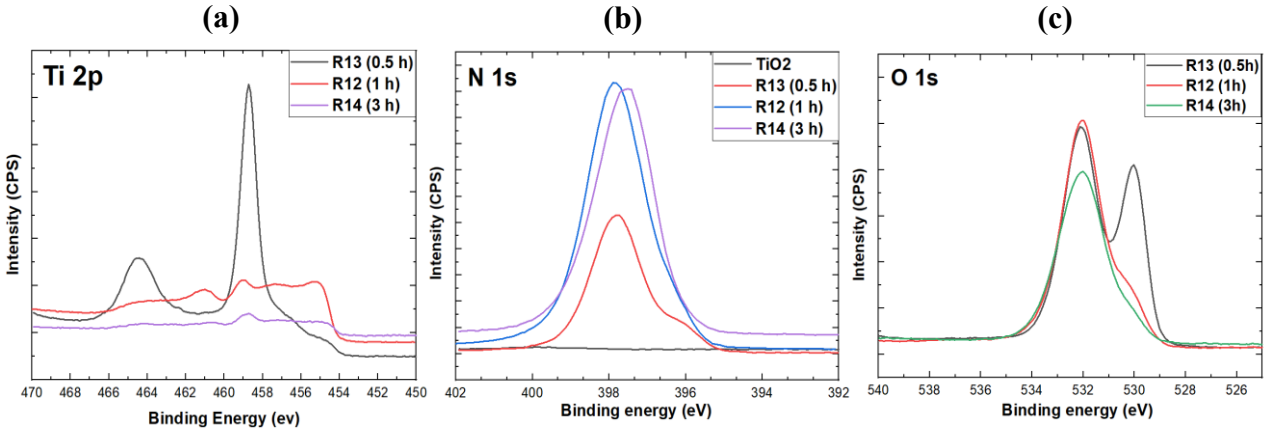

Figure 5.13: XPS of TiO_2-NWs nitrided at 0.5, 1 and 3 hours showing (a) Ti 2p, (b) N 1s and (c) O 1s regions [123].

Table 5.4: N 1s binding energies and at. % of different nitrogen environments obtained by modelling the N1 s region of the XPS spectra of the samples nitrided for different time; 0.5, 1 and 3 hours (h) at 100 W, 500 mTorr and 600 °C.

Binding energy (0.5h)	At. %	Binding energy (1h)	At. %	Binding energy (3h)	At. %	Peak
397.8 eV	10 %	397.8 eV	19 %	397.5 eV	20 %	Ti – N (substitutional N)
396.2 eV	1.9 %	396.6 eV	13.9 %	-	-	Ti – O – N (Interstitial N into TiO lattice)
399.3 eV	0.6 %	399.2 eV	2.9 %	399 eV	2.2 %	Absorbed N_2 or N – H from NH_3.

5.3.1.3 Varying chamber pressure

In order to optimise the chamber pressure towards effective nitridation, the parameters were varied from 300 (R_{19}), 500 (R_{12}), 900 (R_{16}) and 1400 mTorr (R_{17}) while power, time and temperature were kept constant at 100 W, 1 hour and 600 °C, respectively. The Raman spectra of those nitrided NWs are illustrated in Figure 5.14 in which all the peak intensities have reduced and it does not seem that varying the pressure has different effect on the nitridation as compared to power and time. However, XPS analysis have reveal more information about the compositional change.

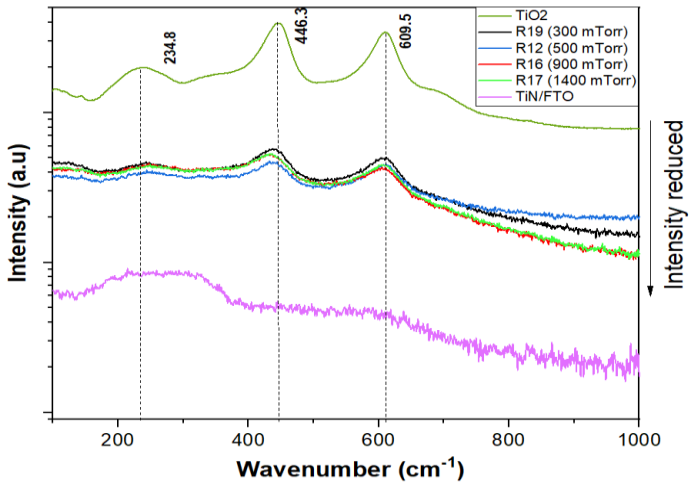

Figure 5.14: Raman spectra of TiN/FTO, TiO_2-NWs nitrided at 300, 500, 900 mTorr and the as-grown TiO_2-NWs is shown for comparison [123].

Figure 5.15 illustrates that NWs nitrided at a pressure of 500, 900 and 1400 mTorr exhibit pronounced TiN and oxynitride peaks at ~455 and ~457 eV, respectively, with varying intensities, while NWs nitrided at a pressure of 300 mTorr had a very low nitride peak intensity. It is known in PECVD that at low gas pressures, plasma density is lower due to the less gas molecules available for collisions, leading to a less ionisation and generation of free radicals responsible for nitridation [136].

Another way of looking at this resultant behaviour is that due to the increased mean free path of the generated ions, as a consequence of applying lower gas pressure, those ions would greatly bombard the surface of the NWs with greater kinetic energy causing re-sputtering of atoms already made reaction with the surface, e.g. formation of Ti-N bond, hence suppressing nitridation [123]. N 1s region of the NWs nitrided at 300 mTorr, not surprisingly, shows relatively higher nitrogen portion (and similar to that of NW nitrided at 900 mTorr) as compared to the other nitrided NWs. It is suggested that nitrogen ions and radicals are progressively diffusing or bombarding the sample surface, while breaking Ti-O bonds on their path, due to their relatively higher energy bombardment, leading to over-stoichiometry TiN_x or nitrogen rich TiN-NWs [123].

Nitridation are much more pronounced in Ti 2p region at 500 and 1400 mTorr as compared to 900 mTorr. In Figure 5.16, the area counts of Ti-N peak at ~455 eV, obtained from Ti 2p, spectra are plotted with respect to gas pressure. It can be observed that the area counts tend to generally increase with pressure. This is because of the increased ionisation and dissociation of the gas molecules due to the increased ion collisions, leading to increased surface reaction. However, N 1s of the sample nitrided at 1400 mTorr showed the lowest nitrogen content as compared to other nitrided samples. This is because the plasma becomes relatively denser in which those ions start to lose their energy as they reach the substrate surface as a consequence of higher rate of collisions, leading to lower nitrogen diffusion into the sample surface. The process pressure of 900 mTorr, resulted in a stoichiometry of 2.5 while the stoichiometry of the sample nitrided at 1400 mTorr exhibited 1.7.

From the results above, it can be concluded that a pressure of 500 mTorr resulted in more effective nitridation as compared to the other nitrided samples in which the N/Ti at.% is much closer to stoichiometry than the other nitrided samples.

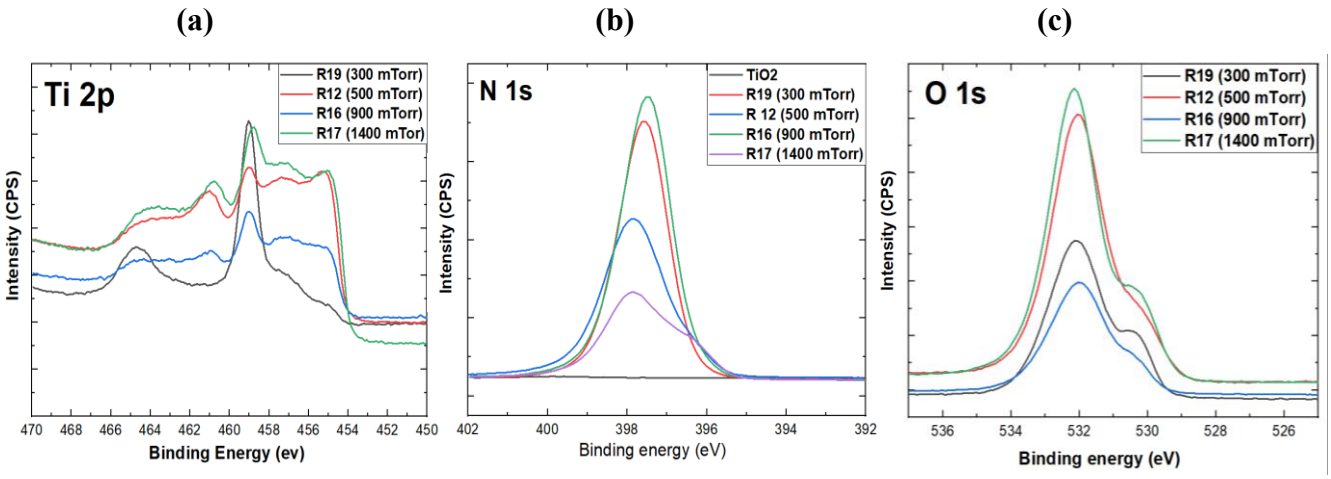

Figure 5.15: XPS of TiO_2-NWs nitrided at different pressures showing (a) Ti 2p, (b) N 1s and (c) O 1s regions [123].

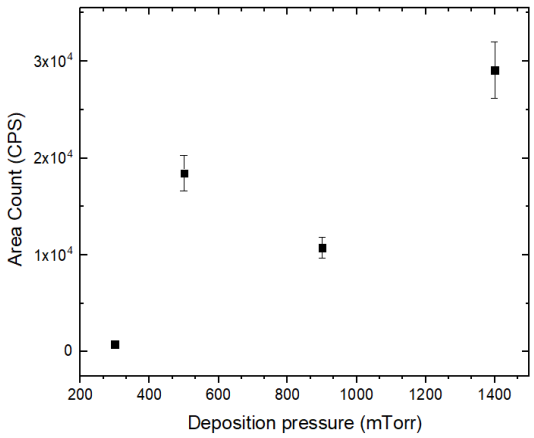

Figure 5.16: Effect of deposition pressure on Ti 2p peak area of Ti – N [123].

5.3.2 Structural analysis

5.3.2.1 TEM

Figure 5.17 shows TEM images of single TiO_2 nanowire (figure (a)-(c)) and TiN nanowire (figure (d)-(i)). The high resolution TEM image in Figure 5.17 (b) displays a uniform, regular and highly oriented crystal configuration with a typical interspacing distance of 0.3 nm and 0.25 nm, corresponding to the (200) and (101) crystal plane of rutile phase TiO_2, respectively. It can be noted that (200) plane corresponding to inter-planner spacing 0.3 nm is the preferential growth orientation seen in TEM, while the preferential orientation plane seen previously in XRD (Figure 5.8) was (002). The deviation of the results here is because the XRD pattern obtained had the preferential orientation of the crystal with respect to the substrate, while in the selected area electron diffraction (SAED) pattern, the single crystal have been oriented along precise zone axis for the electron diffraction acquisition without any relationship with the substrate. The SAED in Figure 5.17 (c) also identifies the plane orientations.

After nitridation, the high resolution TEM image in Figure 5.17 (e) and Figure 5.17 (h) display two planes of (200) and (111) which correspond to the character crystal plane of TiN material. The two planes have regular crystal configuration with reduced interspacing which confirms the transformation of TiO_2 to TiN material [149]. However, the fingerprint of TiO_2 material is still present; (101), (200) (110) and (001) and the preferential orientation of the material after nitridation is still (200). TEM agrees with XPS results in which the nitrided nanowires exhibit a combination of TiO_2 and TiN.

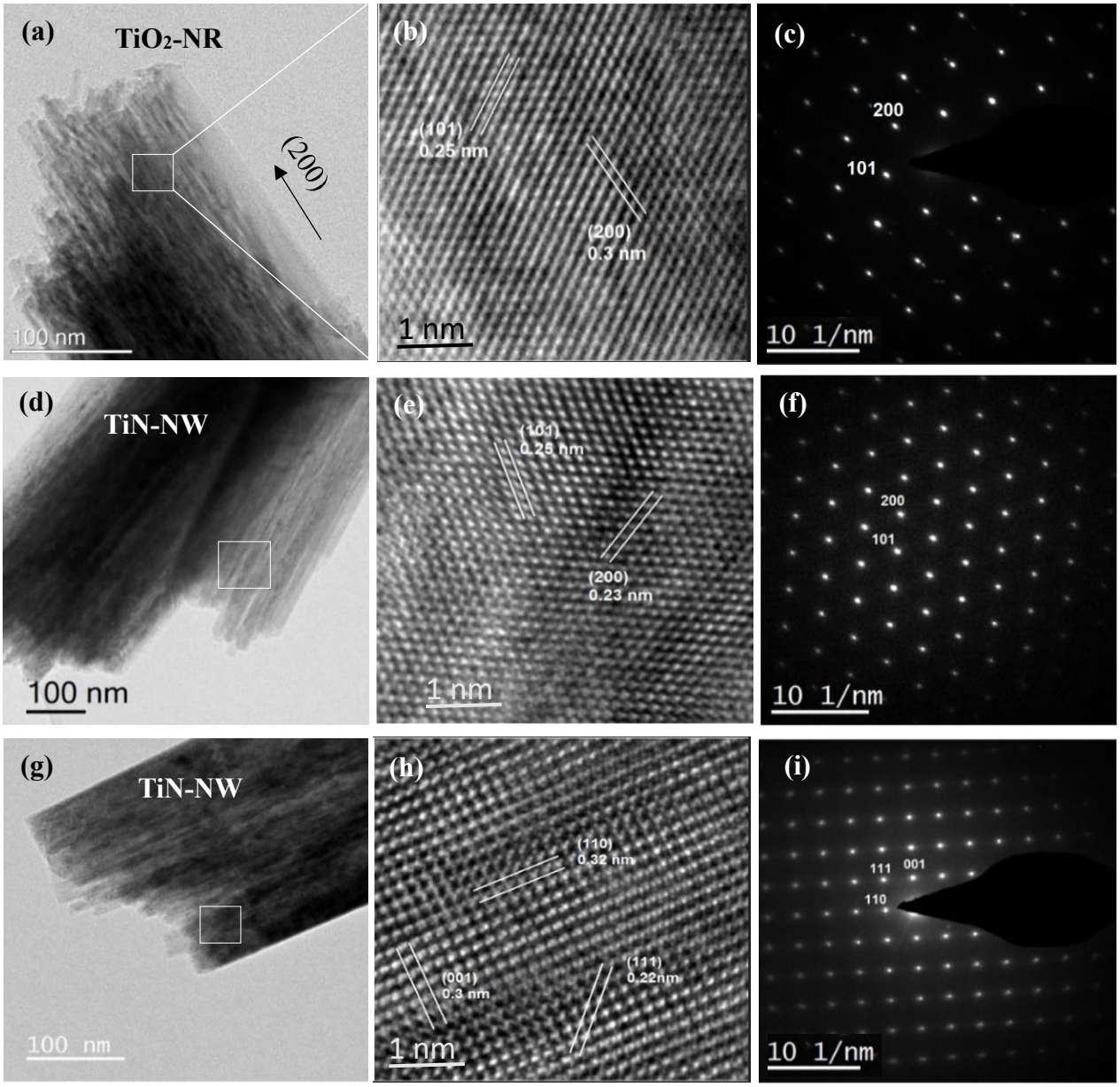

Figure 5.17: TEM images of TiO_2-NWs, b) HRTEM of TiO_2-NR, c) SAED of TiO_2-NR, d) and g) TEM images of TiN-NW, e) and h) HRTEM, f) and i) SAED of TiN-NW [123].

5.3.2.1 XRD

XRD patterns of TiN-NWs nitrided at various time, power and pressure are shown in Figure 5.18, Figure 5.19 and Figure 5.20, respectively. From Figure 5.18, it seems that the peaks of TiO_2, (101) and (002), have significantly decreased after nitridation, even at the first 30 minutes. However, few new peaks corresponding to TiO_2 as well as TiO have evolved. An increase of the peak intensity corresponding to TiO is observed at nitridation time of 3 hours. The increase of TiO peak intensity could be due to the continues ions bombardments onto the substrate which breaks many of the TiO_2 into TiO. TiN diffraction pattern, however, are not seen for those samples nitrided at 100 W, 500 mTorr for different nitridation times. TiN peaks are also not presence for those samples nitrided at different powers for 1 hour and 500 mTorr (Figure 5.19), while only different patterns of TiO_2 are present. Figure 55, shows those samples nitrided at different pressures at an RF power of 100 W and for a nitridation time of 1 hour. It can be seen that a new peak has appeared at $2\theta = 43°$ for those samples nitrided at 300, 900 and 1400 mTorr. This peak could either be interpret as TiN or TiO_xN_y. To confirm this, the lattice parameter of this peak was calculated and 4.128 nm was obtained. This value is much less than TiN lattice parameter. It is known that the oxygen atom could lower the lattice parameter of TiN. Considering this, the peak at 43° could be attributed to TiO_xN_y. In addition, it seems that TiO phase is not present for those samples and so direct nitridation from TiO_2 to TiO_xN_y might have occurred. Although TiO_xN_y is present in R_{16}, R_{17} and R_{19}, R_{12} was chosen as the optimised parameter in this work. This is because it appears that at higher and lower pressures than 500 mTorr, more intensive energetic species might have generated which might have caused higher bombardment to the substrate, causing the dissociation of FTO layer underneath the nanowires. This is evidence from the appearance of tin (Sn). In addition, TiO_2 peaks corresponding to (101) and (002) can still be observed after nitridation except for sample nitrided at a pressure of 500 mTorr. This also agrees with XPS that showed higher concentration of TiO_2 in R_{16}, R_{17} and R_{19}. Although R_{12} has not resulted into polycrystalline TiN but it is believed that higher percentage of TiO_2 has been converted into amorphous TiN.

From XRD data it can be seen that plasma nitridation not only attempts to convert TiO_2 into nitride but has generate further crystallographic orientation of TiO_2, which could be due to an oxygen by-product re-depositing on the sample surface or could be due to annealing. However, it can be seen that the results here provide evidence that the nitridation conversion of the nanowires under the applied conditions will eventually yield to full conversion to the TiN cubic structure with possibly higher resolution of parameters optimisation. Nevertheless, an attempt to nitride TiO_2-NWs at higher temperature of 750 °C did not result in improvement of nitridation. In fact, increasing the nitridation temperature resulted in the escape of titanium atoms from the sample surface as were seen in Ti2p XPS region (data not shown). Therefore, there could be a quite narrow window of temperature in which polycrystalline TiN can be obtained in PECVD.

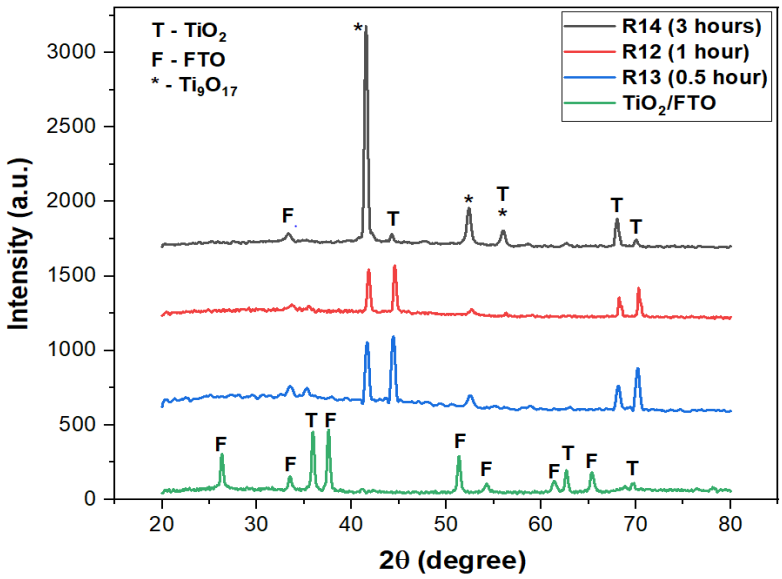

Figure 5.18: XRD pattern of TiN-NWs nitrided at a power of 100 W and pressure of 500 mTorr for 0.5, 1 and 3 hours.

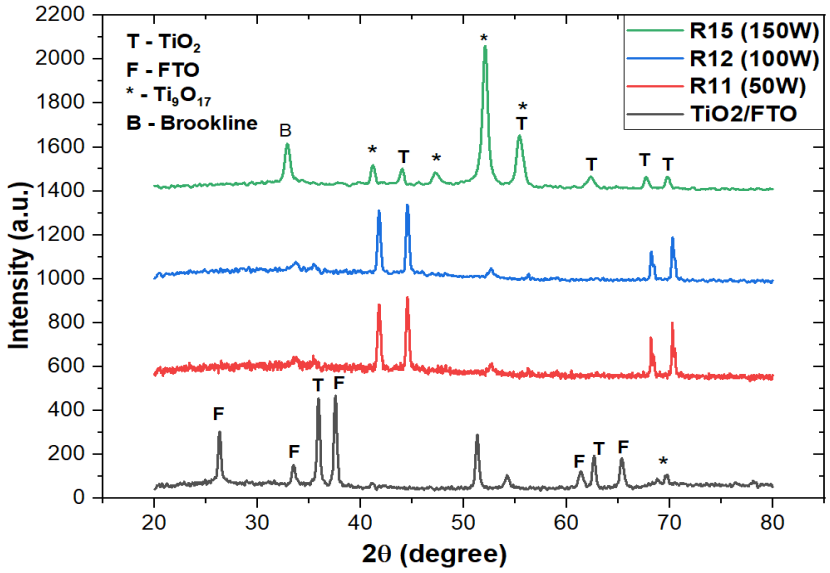

Figure 5.19: XRD pattern of TiN-NWs nitrided for 1 hour, at a pressure of 500 mTorr and for 50, 100 and 150 W.

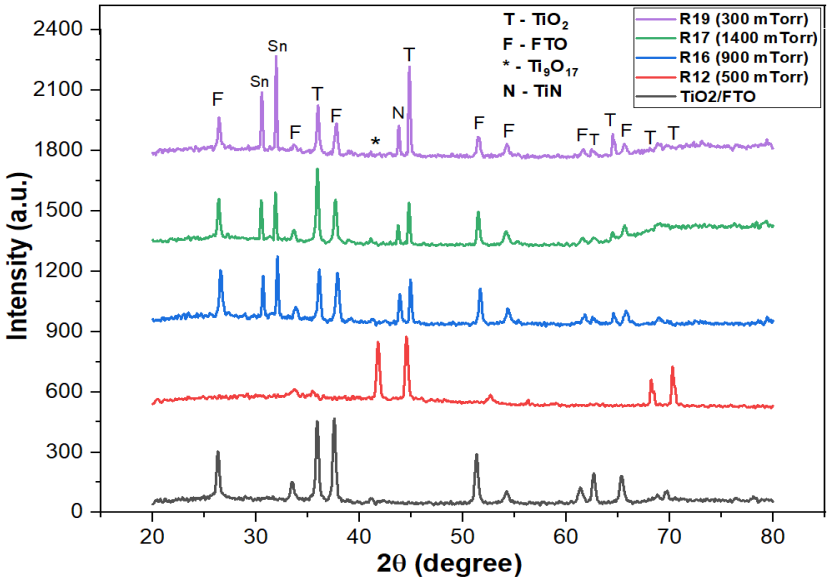

Figure 5.20: XRD pattern of TiO_2-NWs nitrided for 1 hour, at an RF power of 100 W for different pressures.

5.3.3 Electrochemical test – Cyclic voltammetry

5.3.3.1 TiN-NWs and film capacitances

In order to test the suitability of the grown TiN-NWs as an electrode material, their electrochemical performance was studied. In addition, to emphasise the effect of surface area, TiN-NWs CV performance was compared to that of a sputtered TiN thin film optimised in the previous work [102]. Figure 5.21 shows CV curves of TiN film and TiN-NWs tested in PBS solution of 0.1 M at a scan rate of 50 mV/s and potential range of -0.4 to 0.6 V versus Ag/AgCl. The quasi-rectangular shape of both CV curves indicates a good electrical double layer capacitance with reversible electrochemical process, which is essential characteristic of an electrode material for stimulation and recording neural activities. The 3th cycle curves were taken into account here to ensure that the electrode material has stabilised with the electrolyte solution. It can be seen that the integral area of the nanowires as compared to thin film is enlarged giving a capacitance value of 3.46 mF/cm^2 (equal to a charge injection of 2.1 mC/cm^2) as compared to ~0.71 mF/cm^2 of the thin film (equal to a charge injection of 0.426 mC/cm^2). The remarkable enhancement of current density and capacitance of TiN-NWs is attributed to the high surface area that those nanowires exhibit. The enhanced surface area achievable in nanowires increases the electrical conductivity which not only facilitates the faster transport of charge carriers but also permits intake in larger quantities [118].

The areal capacitance of those nitrided nanowires obtained in this work is higher than the one reported in [19] and slightly lower than that obtained in other work [20]. It is believed that the capacitance value of TiN-NWs obtained here can be improved. The existence of the amorphous structure and having a stoichiometry of $TiN_{0.49}$ may have limited the charge transport for the double layer capacitance [150]. In addition, since the CV of TiO_2-NWs in this work showed a resistive behaviour (data not shown), the existence of some TiO_2 structure in the nitrided sample could be a limiting factor for its capacitive behaviour [27]. Nevertheless, the capacitance value produced elsewhere [19] (3.14 mF/cm^2) is associated with TiN nanotube produced by nitridation of TiO_2 nanotube at a higher temperature of 800 °C and for longer time of 4 hours under the flow of N_2. Another work [20] has synthesised TiN nanowires through nitridation of TiO_2 nanowires at 1200 °C for two hours, achieving a capacitance of 4.3 mF/cm^2.

This work has offered the synthesis of TiN nanowires at much lower temperature and with an aspect ratio fit for the purpose of the application here that allow the achievement of comparable order of capacitance to other work. It is believed that further optimisation of nitridation conditions towards full conversion of TiO_2 to TiN as well as obtaining polycrystalline and stoichiometric TiN can promote further enhancement in specific capacitance of TiN.

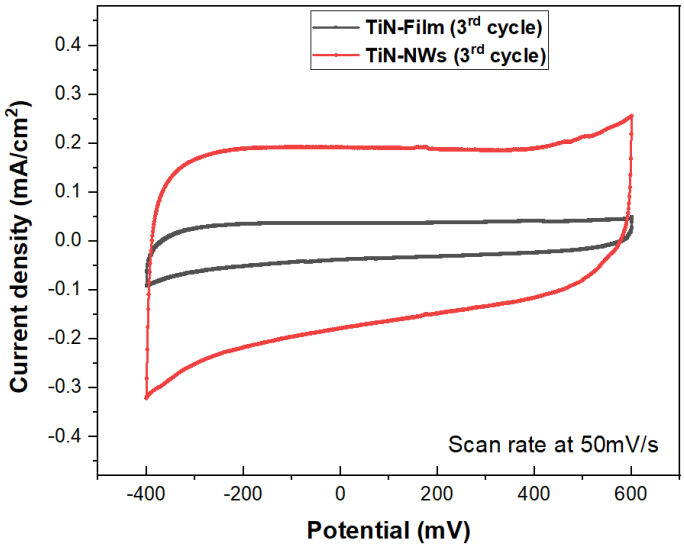

Figure 5.21: CV curve of TiN-NWs and TiN film for a potential cycling between -0.4 to 0.6 V versus Ag/AgCL.

5.3.3.2 CV Stability test over number of cycles

To measure long-term device performance, electrochemical stability tests of TiN-NWs were performed by sweeping the cathodic and anodic potential over 200 cycles at a scan rate of 50 mV/s. The experiments were performed under nitrogen and air ambient using two different electrodes. SEM images of electrodes before and after 200 cycles were taken (data not shown) to confirm any structural changes onto the surface. No structural changes to the surface morphology have been observed to electrodes cycled after 200 cycles, illustrating the structural stability of the grown NWs. From Figure 5.22 (a)-(b), it can be seen that the shape of the CV curves across the 200 cycles remained relatively unchanged for both electrodes which indicates a good stability behaviour and robust nitridation. From the CV shape in Figure 5.22 (b), the current is seen to tail downwards at low potentials which could be due to oxygen reduction in the solution near the electrode surface which contributes into the current. The same behaviour was seen previously with TiN film (Figure 4.13). As oxygen is reduced and consumed near the electrode surface, the current is reduced with increase of cycles. This behaviour is less pronounced in the electrode cycles under nitrogen (Figure 5.22 (a)) due to the less concentration of free oxygen in the electrolyte. It is worth mentioning that TiN-NWs CV curve did not show a noticeable increase in oxide layer over cycles; a broad cathodic peak like the one seen in Figure 4.16 (a), this indicate a robust nitridation process.

Figure 5.23 shows the corresponding capacitance of both electrodes with respect to the cycle number. It is observed that the electrode cycled under air ambient experienced a gradual reduction of capacitance during the first 50 cycles where it stabalised afterward. The capacitance of the electrode cycled under nitrogen, on the other hand, remained relatively unchanged across the 200 cycles. Both electrodes, however, showed excellent capacitance performance with capacitance retention of 99% and 92% for the electrodes cycled under nitrogen and air ambient, respectively. The good stability in the cyclic voltammetry process TiN-NWs highlight the potential capability of PECVD as a nitridation method. In addition, due to the excellent electrochemical performance of those TiN-NWs, they can act as a highly feasible electrode material for recording and stimulation of neurons.

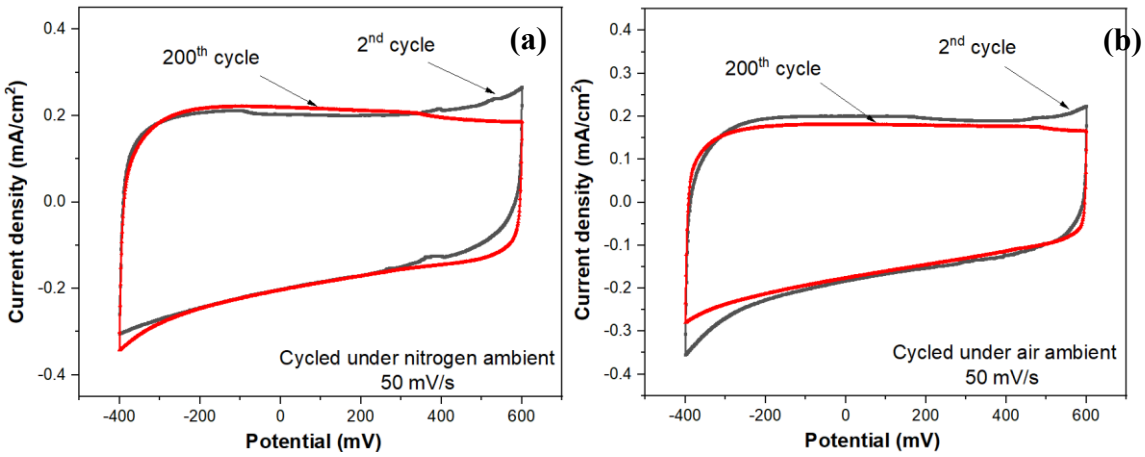

Figure 5.22: CV curves of TiN-NWs for a potential cycling between -0.4 to 0.6 V versus Ag/AgCl showing cycling stability performance under (a) nitrogen ambient and (b) air ambient, over 200 cycles.

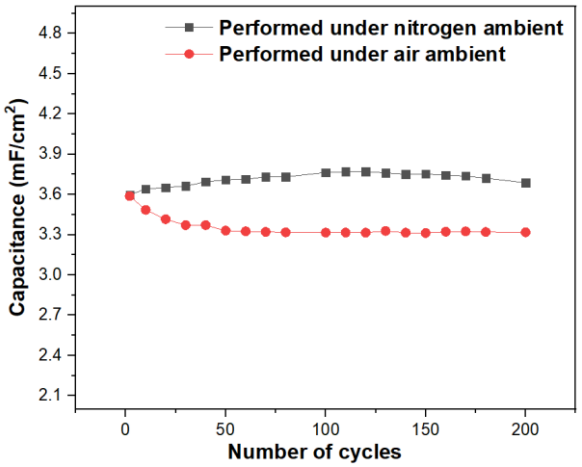

Figure 5.23: Capacitance stability over 200 cycles tested under nitrogen and air at a scan rate of 50 mV/s.

5.3.1 Electrochemical test - Impedance

5.3.1.1 TiN-NWs and film impedance comparison

Electrochemical impedance spectroscopy (EIS) is another way of testing the suitability of the grown TiN-NWs as an electrode material as it studies the material's internal resistance. The electrochemical impedance for TiN film and NWs electrodes were measured and compared. The impedance was recorded after 3 CV cycles (their CV curves were presented in Figure 5.21). EIS measurements were made at the open circuit potential, with a frequency range of 4 MHz to 1 Hz at an applied AC voltage amplitude of 10 mV. EIS is used to give a good understanding about the interfacial resistance between the electrode and electrolyte. Generally, the total electrode impedance is attributed to the solution resistance (R_s), polarisation (R_p) or charge transfer resistance (R_{ct}) occurring at the interface as well as diffusion resistance of ions from bulk solution towards or away from the interface. EIS can be represented in Bode (Figure 5.24) and Nyquist plots (Figure 5.25) which are both discussed in detail below.

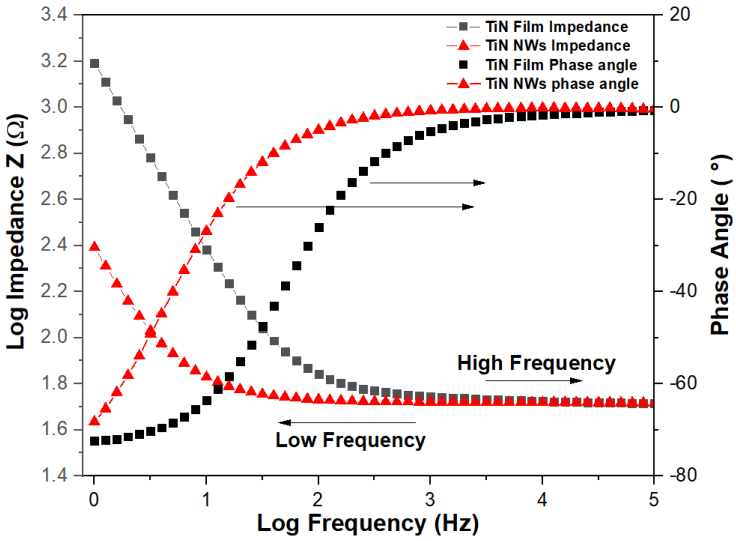

Figure 5.24: Bode plot of TiN film and TiN-NWs.

Bode plot is usually represented using log of frequency on the x-axis and log of impedance on the y-axis. In an electrochemical capacitive system, the impedance (Z) decreases with increasing frequency according to equation (3.13)). In fact, *at high frequency region*, the impedance is independent of frequency and it becomes dominated by the solution resistance between the working and reference electrode. *In the middle frequency region*, where the impedance starts to increase with decreasing frequency, the impedance is attributed to the capacitive double layer formed at the

electrode interface. *At low frequencies*, ion diffusion towards the electrode plays an important role and the impedance becomes more capacitive as the phase angle almost reaches 90° [62]. Therefore, at high frequencies, the contribution of C_{dl} decreases as there is not enough time for the ions to diffuse toward the interface, and the major contribution of capacitance comes from bulk electrolyte process (B_{ulk}) [151].

Here, the double layer capacitance (C_{dl}), originates soon after an electrode is immersed in an electrolyte solution from the accumulation of opposite charges towards the electrode due to electrostatic attraction. As charge is not transferred but only accumulated in a double layer in close proximity to the electrode, it can be modelled as a capacitor. As it is difficult to interpret the electrochemical phenomena that occurs at the electrode surface, an attempt has been made to do the same.

Here, Figure 5.24 represents bode plot and phase angle of both TiN film and NWs, which shows characteristics of capacitive behaviour. It can be seen that the impedance of both structures at the high frequency region (4 MHz- 50 KHz) overlap, giving R_s of ~54 Ω. As frequency reduces (mid-frequency range) it can be seen that the NWs provide lower impedance at 1Hz than that of the film which might be an indication of higher capacitive behaviour corresponding to higher active surface area [152]. However, the polarisation resistance is not shown in the bode plot and so Nyquist plot of both structure will be explained to further understand the electrochemical process at the electrode-electrolyte interface.

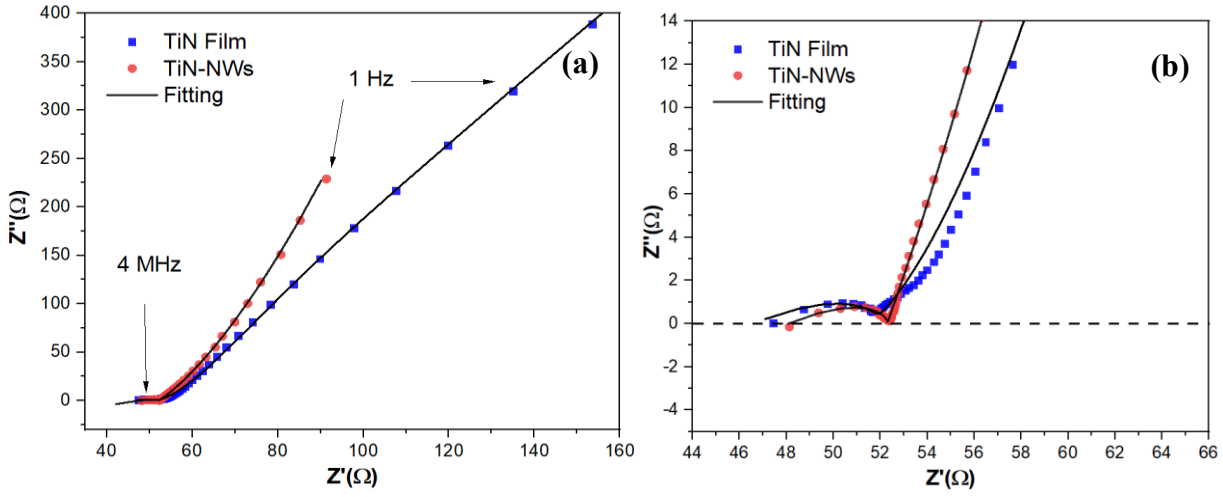

Figure 5.25: a) Nyquist plot and b) Nyquist plot at higher frequency region, for both TiN film and nanowires.

Nyquit plot, on the other hand, in Figure 5.25 (a)-(b), shows impedance behaviour as a function of real Z in the x-axis and imaginary part on the y-axis, where the left most and right most points of the graph represent the maximum (4 MHz) and minimum (1 Hz) frequency, respectively.

Generally, in an electrochemical double layer capacitor system, nyquist plot has a typical shape as the one shown in Figure 5.26; with a semicircle at high frequency (first segment), followed by a line with 45° inclination (second segment) then a vertical line at low frequencies with 90° phase angle (third segment) [151]. The first interception point on the real axis in high frequency region is represented as a series resistance (R_s), which is introduced to model the resistance of the electrolyte and the internal resistance of the electrode. The semicircle is developed as the electrical double layer formed by the accumulation of charges (or polarised ions) to the Helmholtz region near the electrode surface, and so the second interception point on the real axis is represented by the resistance of those polarised ions to form the double layer; polarisation resistance (R_p). In a polarised electrode, no charge transfer across the electrode-electrolyte interface occurs, whereas in a system where charge transfer through redox reactions occurs, the diameter of the semicircle is represented by charge transfer resistance (R_{ct}). Therefore, a bigger semicircle means larger resistance [153].

At middle frequency region (the second segment), diffusion of ions determining the diffusion impedance is represented by the element (W) corresponding to Warburg impedance and usually appears as a straight line with a slope of 45°. The presence of such line means that the electrochemical process is under diffusion control and is independent of frequency [154]. A lower slope means higher ion diffusion resistance [153]. The Warburg impedance at high frequencies is small because ions do not have time to move very far, while at sufficiently low frequencies, sufficient time is given to those charges to diffuse through the diffusion layer and move closer to the Helmholtz plane. This movement increases the Warburg impedance [155]. As frequency is further reduced (the third segment), charges ultimately occupy all of the available active surface on the electrode and contribute to the electrical double-layer capacitance (C_{dl}), therefore, the vertical line seen in Nyquist plot is an indication of capacitance behaviour dominance in which its line phase approaches 90° [151].

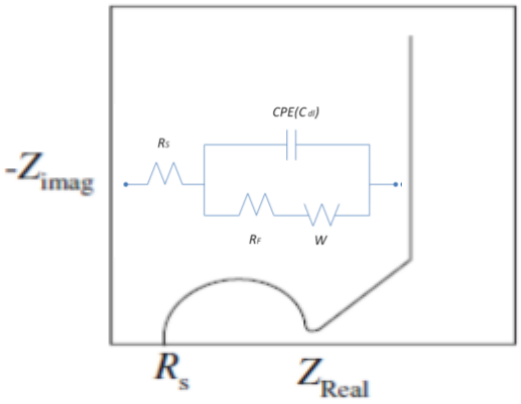

Figure 5.26: Nyquist plot of an electrochemical double layer capacitance with Warburg effect and a constant phase element [151].

Therefore, knowing the above, the magnified spectrum presented in Figure 5.25 (b) shows a semicircle and an inclined line at lower frequencies for both the nanowires and film samples, but their shapes are deviated from the ideal shape that correspond to a capacitive behaviour with Warburg effect discussed above (this will be explained later below). The semicircles arise due to the formation of a capacitive component attributed to the double layer formation at the electrode surface soon after the electrode is immersed in the electrolyte. The shape of the semicircles of the film and NWs illustrate a Gerischer-type response which arises due to ions interacting with a porous-type surface. However, the Gerischer response is slightly different in the film electrode from the NWs electrode as it will be seen from the modelled circuit in the following section. It can be noticed that both the NWs and film semicircles at high frequency region exhibited similar internal resistance values (R_s) although both samples have different surface structures. It could be that at high frequencies, the area of the electrode exposed to the ions in the electrolyte are similar as ions have not yet diffused through the NWs structure, hence giving similar solution resistance. As frequencies are reduced, a noticeable difference in ion diffusion behaviour between both structures can be observed (Figure 5.25 (a)).

From Figure 5.25 (b), the thin film exhibits first an inclined line at approximately 45°, followed by a second steep line corresponding to a semi-infinite linear diffusion of ions, whereas the nanowires exhibited only a steep line which started from the end of the semicircle, and continued with a shorter and steeper line than the film. The presence of a 45° line in the thin film represents a resistive behaviour of the ions diffusion from the bulk solution to the planar electrode surface [156]. The absence of this 45° line in the nanowires suggest a more capacitive effect, possibly due to trapped charges within the nanostructure. The steep line seen in Nyquist plot for the NW-based electrode at

the low frequency end corresponds to finite or restricted ion diffusion type which can be modelled with anomalous or Bisquert element. The semi-infinite diffusion usually arises with planar electrodes (or thin films) where an ionic concentration gradient exists and the diffusion layer thickness increases. However, TiN film was modelled as a porous film given its surface roughness and existence of pin-holes which can result in a small degree of finite ion diffusion. On the other hand, as in the case of an electrode containing a NWs structure, the type of ion diffusion can be finite. Due to the almost vertical nature of the grown TiN-NWs, the surface resembles a porous film, where the small diameter compared to the height of the nanowires results in a finite or restricted diffusion of ions as they are trapped within these spaces [157]. Therefore, such diffusion can be modelled with the anomalous Bisquert element. However, due to the dense nature of the NWs, which can be seen as a planar surface, semi-infinite and/or radial diffusion can also be occurring, but its effect can be small.

Indeed, the line for the nanowire leans more towards the vertical Z" axis as compared to the film, indicating that the nanowire has a better capacitive performance which was evidence in the CV in Figure 5.21. The phase angle presenting in Figure 5.24, in fact shows that the film phase angle approaches 80°, while NWs continues to approach 90° in the phase angle plot. Therefore, it can be deduced that ions are experiencing different diffusion paths in both structures, hence the difference in the phase angle and the magnitude of real and imaginary impedances. Analysing Nyquist plots to understand the underlying mechanism of ion-material interactions is not straightforward. When the nanowires are immersed into the electrolyte, double layer is formed not only on the surface of the nanowires but also around individual nanowire allowing effective entrapment of electrolyte ions which not only accumulate at the surface of the nanowires but diffuse throughout the structure of the nanowires, increasing system capacitance due to the larger surface area compared to a planar electrode. In this case, the charge double layer surrounds the nanowire structure due to their increased surface area and possibly also their tips due to their dense structure. Whereas with the films, the charge double layer is only formed in the vicinity of the electrode surface. This may explain the smaller impedance line in the nanowires as compared to the film at lower frequencies, as an increase in capacitance will decrease the impedance at the same frequencies.

Fitting the data with an equivalent circuit:

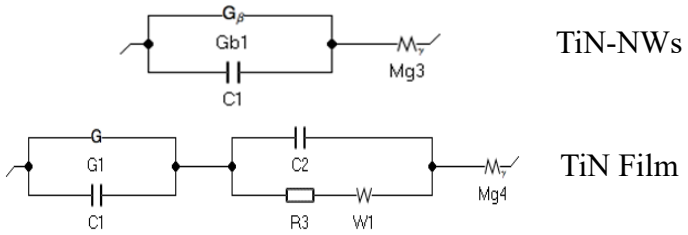

Figure 5.27: Circuit model for TiN film and nanowires used to fit the impedance data.

An equivalent circuit is usually used to model the electrochemical process in the system and fit the data points obtained in the Nyquist plot. In an ideal electrochemical double layer capacitor system, Randles circuit is usually used to model the system where the semicircle is fitted with three elements; R_s in series with C_{dl} and R_{ct} in parallel with C_{dl}, while the Warburg impedance (W) is used in series with R_{ct} to fit the diagonal line with a phase angle of 45° (see inset in Figure 5.26) [158]. However, in our system (for both nanowires and film electrodes), we find that the impedance diagram must include a Gerischer phase element (G) to fit the semicircle data point. Neither the capacitance element (C), representing an ideal capacitor, nor the constant phase element (Q), representing a non-ideal capacitor, were able to fit the experimental data. The equivalent circuits used to illustrate the electrochemical process for both nanowires and thin films are presented in Figure 5.27 (data were fit using EC-Lab fitting software). All fittings of the real and imaginary parts between experimental data and simulated values were less than 2% deviation, indicating a good fitting with the proposed equivalent circuits.

The need of Gerischer element illustrates that the electrodes are behaving like a porous electrode in combination with anomalous diffusion [159]. Although semi-infinite ion diffusion might be dominant in the planar system, modelling the system with Gerischer element was also used to account for the TiN surface roughness and defects. Additionally, the surface of the nanowires (if viewed from top) can be looked at as a porous film, with the distance between two wires (30 nm) acting as a porous hole. It is possible that when ions diffuse through the pores, they get trapped inside due to the electric field build up between two adjacent wires. Therefore, since the NWs structure differ from that of the film, although both are seen as porous, a modified Gerischer element is used for the NWs (G_b). Some papers in the literature have actually used the G element to model a porous or non-flat electrodes [160, 159, 161].

The Gerischer impedance as well as its resultant function is given and illustrated in Figure 5.28 below [162];

$$Z(f) = \frac{R_1}{(1 + i\tau_1 2\pi f)^{\alpha_1/2}} \quad (1)$$

where R_1 is the combination of R_s and R_p in the illustrated case, i donates the complex number at the maximum frequency f of the semicircle, τ_1 is the time constant and α_1 is a constant determining the peak value and the shape of the semicircle.

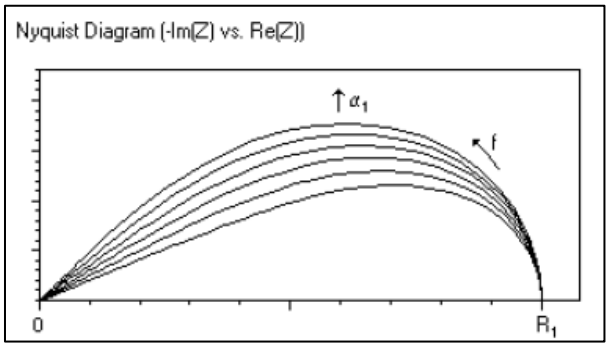

Figure 5.28: Gerischer diffusion element [162].

To fit the nearly 45° inclined line at middle frequency in the thin film, Warburg element is added along with R_p and C_{dl}. Anomalous diffusion element (M_g) is added next in both models to represent ion diffusion through such pores/rough surface of both electrodes and account for the low frequency line that is steeper than 45°. It is worth noting that an attempt had been made to model the thin film with a Warburg impedance element in series with the G_b R circuit but fitting the data at low frequency was not possible and the anomalous diffusion element was needed. M_g has a parameter that accounts for the low frequency line angle; the Gama parameter (γ) which controls the level of the line steepness. However, further examination of the circuit model is needed to improve the fitting of the data for thin films.

The expression of M_g impedance and function (Figure 5.29) is illustrated below;

$$Z(f) = R_1 \frac{Coth(j\tau_1 2\pi f)^{\gamma/2}}{(j\tau_1 2\pi f)^{1-\gamma/2}} \quad (2)$$

where R_1, τ_1, and γ corresponding to the ion diffusion resistance, time constant of ion movement and the anomalous diffusion exponent, while f is the frequency at the point shown in the graph.

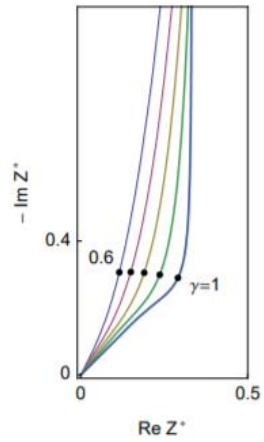

Figure 5.29: Anomalous diffusion element (M_g) [177].

In the anomalous diffusion, the diffusion of ions is non-linear with time due to the non-homogeneity of the electrode geometry [163]. When $\gamma < 1$, the process is called sub-diffusive and when $\gamma > 1$ it is super-diffusive. Table 5.5 below presents the numerical values of the elements of the circuit models presented in Figure 5.27.

γ for the NWs and film are 0.48 and 0.98, respectively. Generally, having a γ that is lower than 1 means that ionic species do not have sufficient space to move and results in sub-diffusive finite transport. Whereas, in TiN films, the value of γ is almost 1, indicating an almost normal semi-infinite diffusion, apart from certain pin-hole defects in the thin-film where there could be a small amount of sub-diffusive transport.

The Gerischer phase impedance, on the other hand, shows no significant difference in value between the two structures. It was expected that the NWs would have a much lower G_b (hence smaller semi-circle) as compared to the TiN film, due to its higher capacitance, but the existence of TiO_2 structures cannot be ignored. TiO_2 structure could be acting as an insulating material, thereby increasing the electrode resistance. As seen from the Figure 5.25 (a), the impedance for 1Hz was much lower with NW electrode than thin film, which is also supported by the assumed model with Mg for TiN-NW electrode showing a lower impedance than TiN-film.

Table 5.5: Numerical values of the elements presencted in the model circuit of both TiN-NWs and TiN film, where R_1 is R_s+R_p , t is diffusion time constant, α is a constant determining the peak value of the semicircle and γ is anomalous diffusion exponent.

Elements	Parameters	TiN-NWs	TiN-Film
G	R_1	52.29 Ω	51.7 Ω
	α_1	0.95	0.95
	G	70.3 Ω	73.66 Ω
	R_3	101.9 Ω	224.6 Ω
M_g	γ_3	0.48	0.98
	M_g	199.16 Ω	222 Ω

5.3.1.2 Impedance stability test over number of cycles

The same TiN-NWs samples used for CV stability test (in section 5.3.3.2) were subjected to EIS after 3 cycles and 200 cycles for both experiments performed under nitrogen and air ambient, their Bode and Nyquist plots are presented in Figure 5.30.

It is seen that the semicircle of both electrodes slightly shift to higher impedance after 200 cycles, but the shifts were similar under both nitrogen saturated and ambient electrolytes. Table 5.6 shows values obtained from the modelled circuit, agree with this observation. The solution resistance of each electrode slightly increases, although it should be the same; this might be because the concentration of ions near the electrode is different after cycling the electrode for 200 cycles, as ions move towards and away from the electrode with CV, changing the electrolyte concentration at the electrode surface. Moreover, there is unpronounced change in the semicircle diameter after cycling in both electrodes, in addition to no greater increase in the semicircle diameter for the electrodes cycled with ambient electrolyte. This illustrates the cycling stability of the TiN-NWs even under electrolyte containing oxygen. The fact that electrolyte ions experience a restricted diffusion through the NWs, oxygen molecules do not have sufficient time to diffuse deep into the NWs structure, due to hindered movement of charges. This supports the nearly identical CV curves obtained at these TiN-NW electrodes before and after cycling, under air or nitrogen ambience (Figure 5.23), where the capacitance values before and after cycling were very similar compared to thin films (see Table 5.7). Consequently, the semicircle does not appear to change much in its diameter.

On the other hand, a noticable increase in impedance would be expected for the TiN film electrode especially when cycled under air. The CV measurments of TiN film before and after 200 cycles in Figure 4.14 illustrates this assumption. Due to the semi-infinite diffusion of ions on the planar electrode, oxygen molecules are able to difuse back towards the electrode surface after being reduced and absorbed onto the surface causing oxidation/reduction, hence decreasing the capacitance and increasing the resistance, and in turn its impedance.

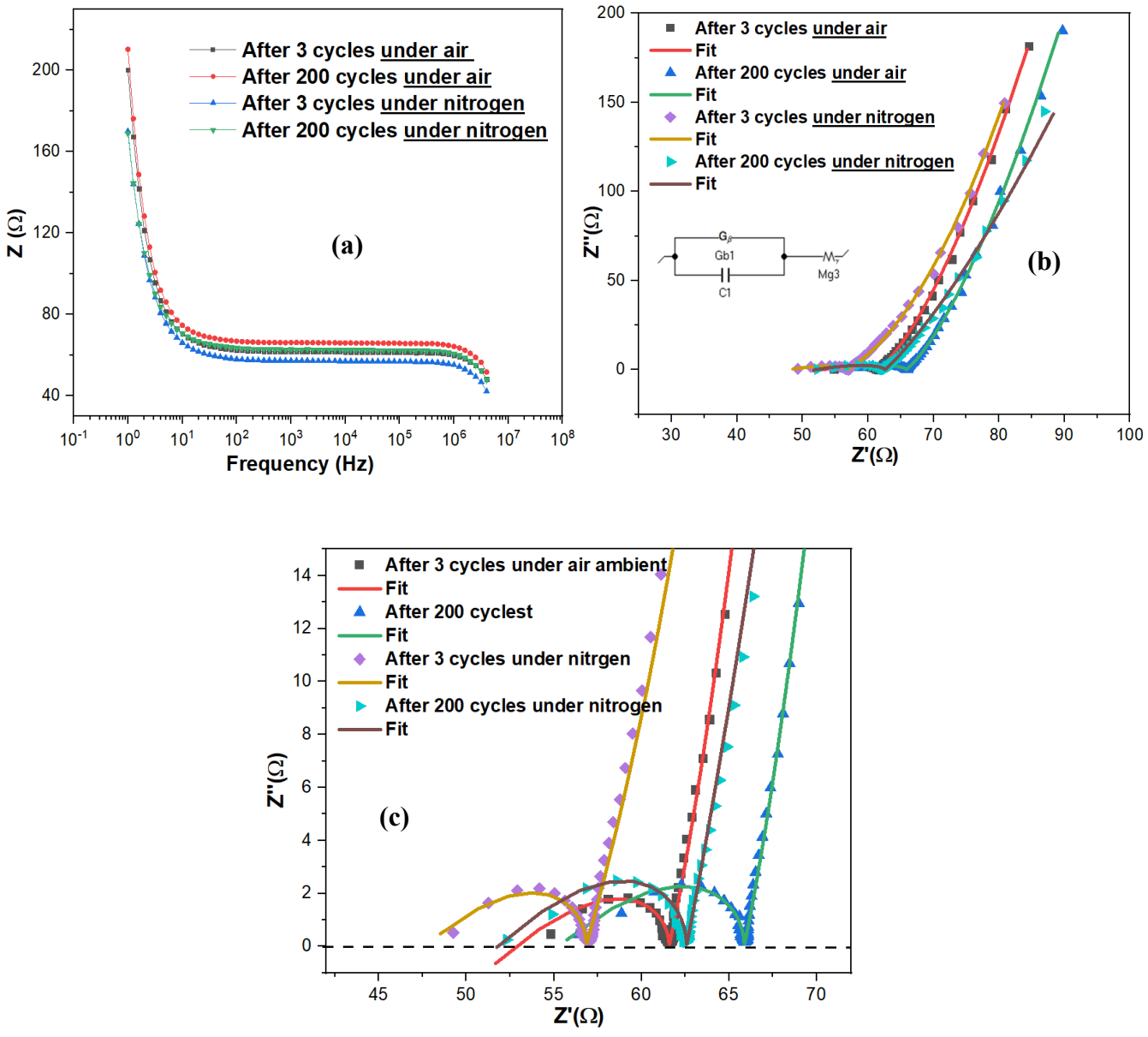

Figure 5.30: (a) Bode plot (b) Nyquist plot showing TiN-NWs impedance cycled under nitrogen and air ambient after 3 and 200 cycles, and (c) Nyquist plot at high frequency region.

From the above results, the impedance of TiN-NWs electrode at high frequencies showed similar internal resistance to that of TiN, while impedance at lower frequencies corresponding to ion diffusion was noticeably lower than that of the film. Although the diffusion of ions is finite or restricted through the nanostructures, the ions were able to diffuse further with time given higher capacitance values and lower diffusion impedance, whereas ions were mostly adsorbing at the surface of the planar electrode through semi-infinite diffusion. Furthermore, TiN-NWs have shown greater CV cyclic stability and lowered susceptibility to oxidation compared to TiN thin films due to their structural nature that promotes finite diffusion and hinders diffusion of oxygen molecules from the bulk solution. For further improvement of the impedance analysis, the circuit model of TiN film could possibly be changed to model a semi-infinite ion diffusion process as this was the dominant process although some surface porosity of the electrode exist.

Table 5.6: Impedance values of TiN-NWs after 3 and 200 cycles, cycled under nitrogen and air ambient.

Elements	**N_2 ambient (3 CV cycles)**	**N_2 ambient (200 CV cycles)**	**Air ambient (3 CV cycles)**	**Air ambient (200 CV cycles)**
G_b (Ω)	70.301	71.83	69.21	72.1
M_g (Ω)	199.16	347.63	243.91	287.12

Table 5.7: Summary of capacitance values of TiN-Film and TiN-NWs at 3rd and 200th cycle, performed under nitrogen and air ambient.

Electrode	**N_2 ambient (3 CV cycles)**	**N_2 ambient (200 CV cycles)**	**Air ambient (3 CV cycles)**	**Air ambient (200 CV cycles)**
TiN-Film	0.68	0.60	0.78	0.57
TiN-NWs	3.6	3.8	3.6	3.4

5.4 Summary

TiO_2-NWs were hydrothermally grown on sputtered TiN nucleation layer. The nanowires were optimised towards achieving high aspect ratio and polycrystalline structure. An aspect ratio of 23.1 and a preferred orientation along (002) plane were obtained at a synthesis conditions of 150°C for 18 hours on 200 nm nucleation layer thickness. Those nanowires were then nitrided through PECVD under ammonia gas at a temperature of 600°C, lower than those reported in the literature. Nitridation process parameters were optimised through XPS and Raman by studying the effect of parameters on the material compositional and structural change. It was found that by increasing the

RF power from 50 to 100 W, this resulted in higher density of dissociative species, allowing effective nitridation. However, further increase in power, some etching of the material started to dominate over nitridation. A nitridation time of one hour was enough to nitride the material in which increase of time resulted in 69% reduction of TiN 2p peak while N at. % remained relatively unchanged indicating that most of oxygen atoms at the surface has been replaced by nitrogen atoms. Pressure on the other hand was found to affect the amount of nitrogen incorporation into the sample. However, analysing the material through XPS, Raman, TEM and XRD has shown fingerprint of TiO_2 material after nitridation, even at higher temperatures suggesting the smaller window in which a fully nitrided material can be obtained.

TiN-NWs was used for electrochemical test and was compared to that of TiN sputtered film. TiN-NWs and TiN thin film obtained a capacitance value of 3.78 mF/cm^2 (2.1 mC/cm^2) and 0.7 mF/cm^2 (0.426 mC/cm^2) respectively. The increase in capacitance seen in the TiN-NWs is due to higher electrochemical active sites that those nanowires exhibit as a consequence of their relatively higher surface area. Stability test for both film and nanowires were performed over 200 cycles showing the excellent capacitance retention of TiN-NWs electrode of almost 99% as compared to the film. In fact, the capacitance retention of TiN-NWs under air ambient (92%) was better than that of the film (70%). EIS has also been performed to study the interfacial resistance of the system. From the electrochemical impedance analysis of NWs and film electrodes it was possible to explain the reason behind the electrochemical cycling stability of the NWs and the lowered susceptibility to oxidation. This was because of the restricted ion diffusion of the NWs hindered the diffusion of oxygen molecules.

To conclude at this point, this work has shown the potential use of PECVD in nitridation at lower temperature which has resulted in material properties suitable for neural-electrode application. However, further optimisation of PECVD process is needed to fully convert TiO_2-NWs to TiN-NWs and achieve a polycrystalline structure. This would produce a material with a higher capacitance value which would further help to mediate the transduction of charge injection capacity.

Chapter 6. Cell culture

6.1 Introduction

Neural interface material should transduce electrical pulses into the nerve tissue without altering the physiological properties of the targeted tissues. Prior to electrophysiological recordings and stimulations, the biocompatibility of the interface material should be tested by culturing cells *in vitro* and examining the cell viability and behaviour on the interfaced material. For an interface material to be biocompatible it should not cause toxicity to the biological tissue, such as causing inflammatory response and its mechanical properties should be suitable in which it should not oxidise, corrode, or degrade over time and so it should provide a prolonged contact between the two interfaces [89]. The properties of neural cells, such as adhesion, cell divisions (known as proliferation), cell density and neurite outgrowth are very much influenced by their extracellular environment. Indeed, when cells are cultured under conditions that prevents adhesion and differentiation, cells can stop growing and ultimately lose viability.

A study has tested the differential behaviour of human neural stem cells (hNSCs) cultured on graphene as compared to glass [164]. After 10 hours of culture, more hNSCs were found on graphene than on glass region, indicating a rapid attachment of the cells on the graphene. However, when the cells where proliferated in the culture media with a growth factor for five days, both regions were fully occupied with viable hNSs cells and no difference in cell number were observed. After 3 weeks of culture the graphene region was fully occupied with the differentiated cells, while many cells were aggregated and detached from the glass region during the differentiation process. Hence the number of cells on the graphene regions were much more compared to the glass region. It was concluded that the graphene upregulated laminin receptors (a high molecular weight proteins of the extracellular matrix which exist in the basal lamina of the cell that acts as a point of attachment for the cell) of the extracellular matrix of the cells, providing better microenvironment for the cells which promoted cell adhesion and neurite growth [164].

It is not just the substrate chemistry that the cells are cultured on can affect the cell viability and behaviour but also the topography of the material can have an effect. A study cultured central nervous system (CNS) cells, derived from postnatal mouse retinas, on arrays of GaP-NWs of different geometries and on flat substrate to investigate which topography support neurite outgrowth [165]. On flat GaP substrates, only few neurite were seen to extend out from cell clusters. The same behaviour was observed on those cultured on short NWs (0.5 μm long). Increasing the length of the NWs to 1 and 4 μm enhanced the neurite outgrowth, irrespective of the diameter of the NW. The overall cell distribution was assessed between the flat GaP and NWs surfaces with NWs density of 1 NW/μm^2. Cell clusters of different sizes were found on both substrates with smaller sized clusters dominated on the NWs, while the number of single cells being less on NWs. In addition, it was found that NW substrates were densely populated with cells while area devoid from cells were noted on the flat substrates, indicating the strong attachment of cells on the NWs substrates. The reason of the observed behaviour was attributed to the preferential adsorption of neurotrophic molecules on NWs that promoted cell adhesion [165].

On the other hand, there have been some reports stating that the viability of cells cultured on nanostructured material is not significantly affected by such structures [166]. Similarly, primary neuron cells were found to survive to the same extent on both GaP and flat substrates [167]. In contrast, some recent study showed that cell viability and proliferation were reduced when cultured on NWs [168]. For example, mouse retinal neurons did not generate any neurites when cultured on etched silicon NWs [168]. However, the decline in growth was found due to the presence of contaminants, such as hydrofluoric acid. The diversity of results between those reports depends on many factors, such as cell type, the chemistry of the material, density of the nanowires and perhaps culture method.

With regard to TiN material, TiN thin film has already been used as a neural-electrode material and was proven to be biocompatible *in vitro* [169] [170] and *in vivo* [171]. Cyster. L.A, et.al [169] have investigated the effect of TiN thin film surface chemistries and topographies on the behaviour of cultured primary hippocampal neurons. The neurons were found to attach and spread on all of the TiN film chemistries and topographies. However, neurons appeared to be more preferentially viable on the nitrogen rich TiN films and on reduced nanotopographical features films. The nitrogen rich TiN films exhibited a more crystalline and dense film structure with a relatively larger grain size, making the surface rougher than the other films, which could have allowed cells to better adhere onto the surfaces [169]. In addition, the cells were more spreader across the surface while

cells on other TiN films were clustered with long neuritic processes extending up to 150 µm in length were observed. This is because cells might be trying to explore their local environment by extending in length and "hunt" spot to attach on [169]. It was suggested that the spreading of cells is promoted by sum of factors, such as the hydrophilic behavior of the surface, surface composition, protein adsorption on the surface, surface roughness and texture [170]. It is quite difficult to predict why cells actually spreads on a surface as the process requires equilibrium between tension and elastic forces on the membrane surface, cellular internal pressures and molecule interactions.

Duta, L, et.al [170] have investigated the cytotoxicity of TiN by culturing fibroblasts, Hs27 cell-line. Different thickness of TiN films were deposited by DC sputtering and the composition and surface roughness were studied to understand what affect the behaviour of cells. All films exhibited good cytocompatibility but a difference between the biological responses of cells were detected depending on the TiO_xN_y and TiN concentration on the sample surface. The sample exhibiting higher concentration of nitrogen or stoichiometry close to 1, the biocompatibility of the material is better in which cellular death were relatively less.

Such TiN materials were grown through, pulsed DC reactive magnetron sputtering [169], pulsed laser deposition [170], and nitridation of titanium under nitrogen atmosphere. In this work, it would be of an importance to test the biocompatibility of TiN-NWs grown through a novel approach through PECVD and compare the behaviour of cells on thin films. In order to test the biocompatibility of the synthesised TiN-NWs material through PECVD approach, glioblastoma cells (GBM) were used for culture. Neural cell types were not available at an appropriate time during this research, but should be included as part of future work.. In addition, to studying the effect of surface structure, cells were also cultured on the optimised TiN film, exhibiting a flatter surface, and their behaviour were compared on both structures. The biocompatibility of the interface materials were tested by investigating cell density, proliferation and adhesion. Cell behaviour was studied for 3, 10 and 20 days *in vitro* (DIV) on both NW and film substrates. The work in this chapter was conducted at Neurooncology translational group, King Fahd Medical Research Center (KFMRC), at KAU.

6.2 Experimental work

6.2.1 Cell culture and plating cells

Jed41_Glioblastoma (GBM) primary cell line (passage 14), retrieved within the Neuroconology Translational Group laboratory at KFMRC, was grown in DMEM-F12 (Gibco), 10% FBS (HyClone), 100 U/ml penicillin, and 100 µg/ml streptomycin, and maintained in standard humidified incubators at 5% CO_2. Cells were seeded on TiN-Film and TiN-NWs substrates at $5x10^3/1cm^3$ for Day 3 collection and $1x10^3/1cm^3$ for Day 10 and Day 20 collection, respectively. Cell suspensions in DMEM-F12 were gently dropped on the surface of the substrates, in which they were then placed in 6 well plates, and incubated as previously mentioned. For long-term plating, media was changed twice a week to maintain cell growth. No chemical coating for cell adhesion mediator was used, prior to cell culture, so as to evaluate the cells adhesion on TiN-NWs as compared to TiN film structure.

6.2.2 Cell staining and imaging

Cells were stained for immunofluorescence imaging on day 3, 10 and 20 to image the cells' cytoskeleton along with the nucleus. Cells were gently washed with PBS, fixed with 4% Paraformaldehyde (PFA) for 10 minutes, and then permeabilized by incubation for 1 hour at room temperature with blocking reagent (5% NGS, 0.25% Triton X-100 in PBS). Cells were stained with primary antibodies solutions (2% NGS, W/O 0.25% 0.25% Triton X-100 in PBS) containing the following antibodies: mouse anti Nestin (1:50, ab6142, abcam) and rabbit anti-Ki67 (1:200, ab16667, abcam) with mouse anti-Vimentin (1:100, ab8978, abcam) and 4',6-diamidino-2-phenylindole (DAPI) for nuclei staining. The cells were further incubated with secondary goat antibodies, 488 anti-mouse (1:300, ab150105, abcam), 555 anti-Rabbit (1:700, ab150074, abcam). Thereafter, the substrates were turned over onto a cover slip to mount and process for image acquisition.

For cell SEM acquisition, cells were fixed in Trump's fixative for one hour at room temperature after being cultured for 3, 10 and 20 days. Following fixation, samples were rinsed with distilled water three times for 10 minutes and subsequently dehydrated in a series of ethanol solutions; 50%, 70% and 100% for 10 minutes in each step. Ethanol was replaced with acetone (99 pure) and the samples were socked for one hour. Thereafter, samples were sputter-coated with a thin layer of gold. SEM study was performed using Quanta 250 SEM (Phillips FEI).

6.2.3 Image acquisition, enhancement, and counting

Images were taken at 5x and 20x magnifications using fluorescence microscope (Leica DMI6000) and Leica DFC425 camera. Photos were processed in Photoshop 7.0 and signal levels were compared to negative controls of secondary only (to eliminate background noise). At least 19 non-overlapping locations on each sample were selected to calculate the average cell density per 1 mm^2, in which cells' nuclei, stained by DAPI, were subsequently counted using automated counting in Image J software for analysis. The differences between the counts for the number of nuclei grown on the film verses the NWs were analyzed using a T-test in Statistical Package for the Social Sciences (SPSS) Graduate Pack 21.0. The differences between two groups of data were considered significant when $p < 0.05$. Images were masked to count nuclei positive for Ki67, and counts were produced using ICTN plugin. Cells' morphology characterization was carried out as previously described [172]. For cell distribution analysis, black and white images of nuclei across a single chip, taken at 5X magnification for cells cultured for 20 days cells, were compiled to form a single image. For statistical analysis and reproducibility verification each experiment was repeated at least three times.

6.3 Cell viability on TiN substrates

Cell viability was assessed in terms of cell adhesion, proliferation and cell counts over the period of 3, 10 and 20 DIV. The cells proliferation was assessed by investigating the cell ability to express Ki67 gene which is a cellular marker for proliferation. The increase of cell nuclei number is also a way of assessing cell proliferation. Figure 6.1 shows fluorescence images of those samples presenting cell nuclei (DAPI, blue) and cell skeleton (Nestin, green). Almost all cells incubated for 3 days and further grown for 10 and 20 DIV, adhered to both TiN-film and TiN-NWs substrates in which clusters and single cells were found across both substrates. A small number of cells expressed the antigen Ki-67 (cell proliferation activity), immunostained with red, in both substrates at each culture period but no significant difference in cell number exhibiting the antigen between both substrates is found according to T-test (if $P<0.005$ is considered significant). In addition, the number of cell nuclei per unit area ($1mm^2$) increased in both substrates when cultured for 3 to 10 and 20 DIV. Those results indicate the viability of the cells on both substrates, since dead cells often detach from the substrate and no proliferation or cell division is found.

Figure 6.2 illustrates the growth rate of cells cultured on both substrates at 3, 10 and 20 DIV. It can be seen that the number of cells nuclei on TiN-NWs is higher in each culture period as compared to the thin film, giving a mean value that is higher on the NWs substrates. However, the difference is not significant according to T test (For 20 DIV, NWs has 7127 cells/$1mm^2$ and Film has 5504/$1mm^2$, giving $P=0.1235$). Similarly, the proliferation of cells (cell divisions) on NWs increased by 46% from Day 10 to Day 20, whereas cell divisions on film substrate increased by 42%, which is not significantly different. The similarity in cell number and proliferation between both substrates indicate that the substrate morphology or structure did not affect the biological function of GBM cells.

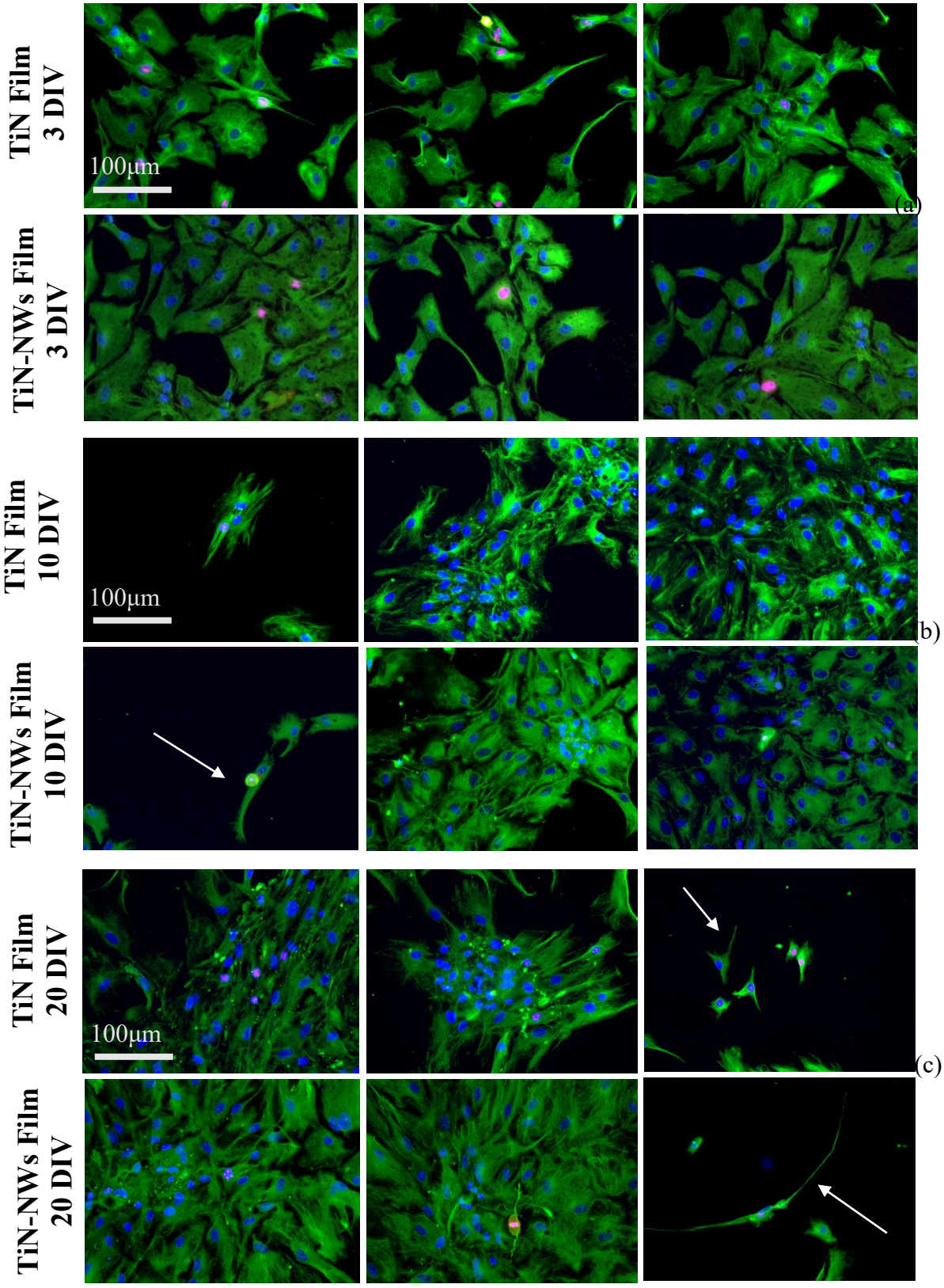

Figure 6.1: Fluorescence images of GBM cells cultured on TiN-NWs and TiN films for a) 3 DIV, b) 10 DIV and c) 20 DIV, showing cell nuclei (DAPI, blue) and cell body (NEStin, green). Images taken at 20X magnification.

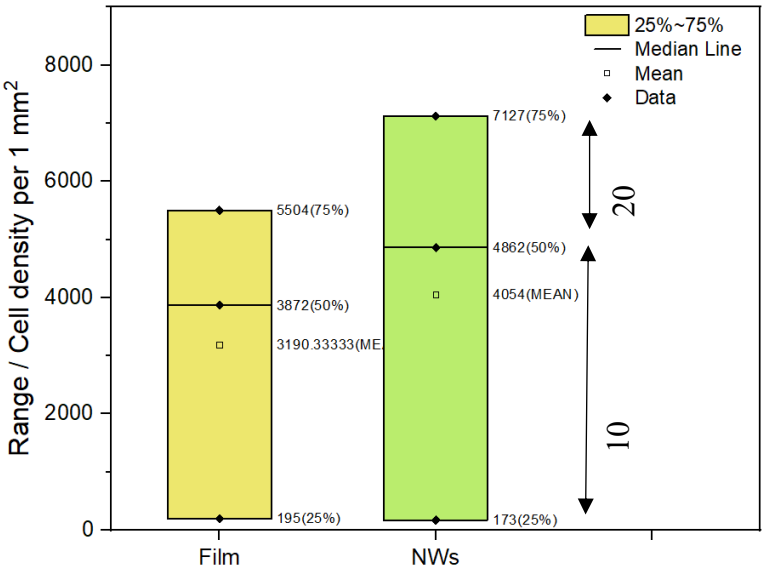

Figure 6.2: Statistical analysis of cell nuclei counts of TiN-Film and TiN-NWs.

In terms of cell morphology, a pronounced difference in cell morphology started to be seen at Day 10 and 20 where cells became more extended and elongated by developing pseudopodium on both substrates than Day 3, however, the degree of extension on the NWs substrate were noticeably higher than on the film, see arrows in Figure 6.1. SEM images in Figure 6.3 (d) illustrate the extension of neuronal-like cells on TiN-NWs at 20 DIV, whereas this behaviour is not seen on TiN-Film. Similar studies have reported the extension of cells on nanostructure materials [173, 174]. In addition, it can be noticed that cells on NWs is forming a 3D structure (Figure 6.3 (d)), whereas cells on the film substrates were mostly flatter in morphology (Figure 6.3 (a)). Florescence image shown in Figure 6.4 illustrates a number of cells exhibiting a 3D structure; since some area goes out of focus. Moreover, as seen in Figure 6.3 (b) and (c) for cells cultured on film for 20 DIV and NWs for 3 DIV, cells are developing filopodia to attach onto the substrate, whereas cells cultured for 3 days on TiN-Film did not show this behaviour. This might be the reason behind the slightly lower number in cell nuclei on TiN-Film as cells do not develop filopodia at early period of culture and detach from the substrate. Similar observation in morphology were reported for difference cell types cultured on NWs [175, 176]. In this work, it seems that nanostructure material reduces stress between cell-substrate interface and induce more comfort extracellular environment that allow them to extend in morphology and well anchor onto the substrate from early stage of culture.

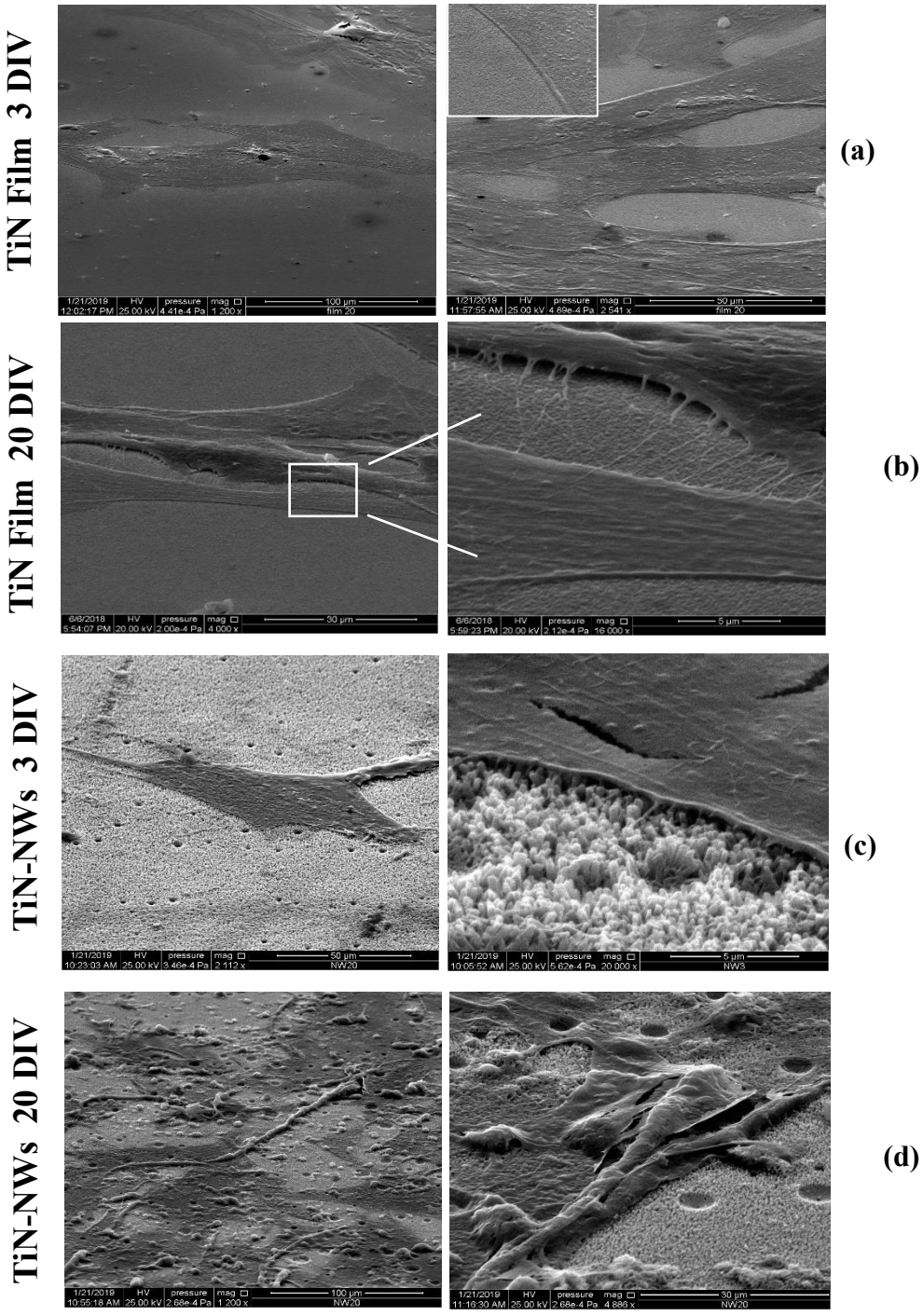

Figure 6.3: SEM images of GBM cells cultured on TiN-Film and TiN-NWs at 3 and 20 DIV.

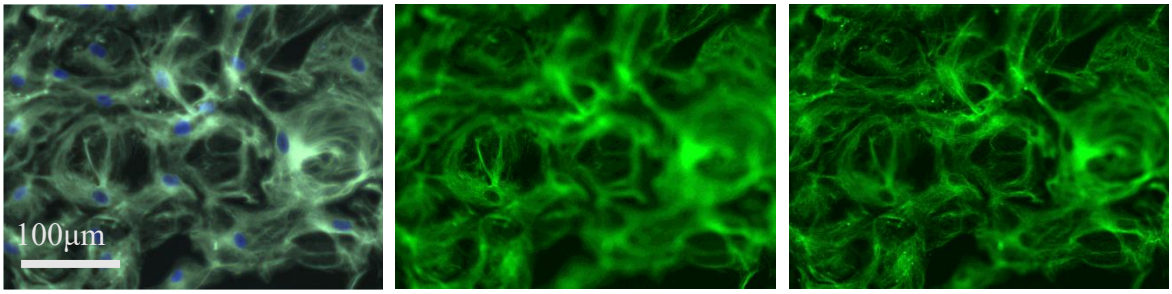

Figure 6.4: Fluorescence images of GBM cells cultured on TiN-NWs for 20 DIV, showing their 3D structure growth.

6.4 Cell distribution

Cell distribution was assessed at 20 DIV by visualizing images taken at 5X magnification showing DAPI-stained nuclei across a single sample of TiN-Film and TiN-NWs as shown in Figure 6.5 (a)-(b). Images were processed using Image J software and the average distance between nuclei's were assessed. In comparison between film and NWs surfaces, it was found that single cells as well as cell clusters could be observed on both surfaces, however, cell clusters are less observed on NWs surface and numerous single cells were presented. Therefore, cell confluence is observed on NWs and not on the flat film surface. A similar results were observed by Piret, G, et.al [165] and numerous number of clusters neurons were found on TiN thin film grown by Cyster, LA, et.al [169]. In fact, the average distance between cell nuclei's on NWs was found to be almost twice the average distance between nuclei's on TiN-film surface. According to the T-test, the effect of surface morphology on the average distance between cell nuclei on NWs as compared to the film is significantly different. This result could illustrate that the cells on NWs exhibit higher mobility allowing them to move freely and adapt a comfort spot to attach on and extend in length. It may well be that cells on the flat film might have a limited mobility and so they form clusters. The flat morphology of cells on film surface might have caused limited mobility of cells on the surface.

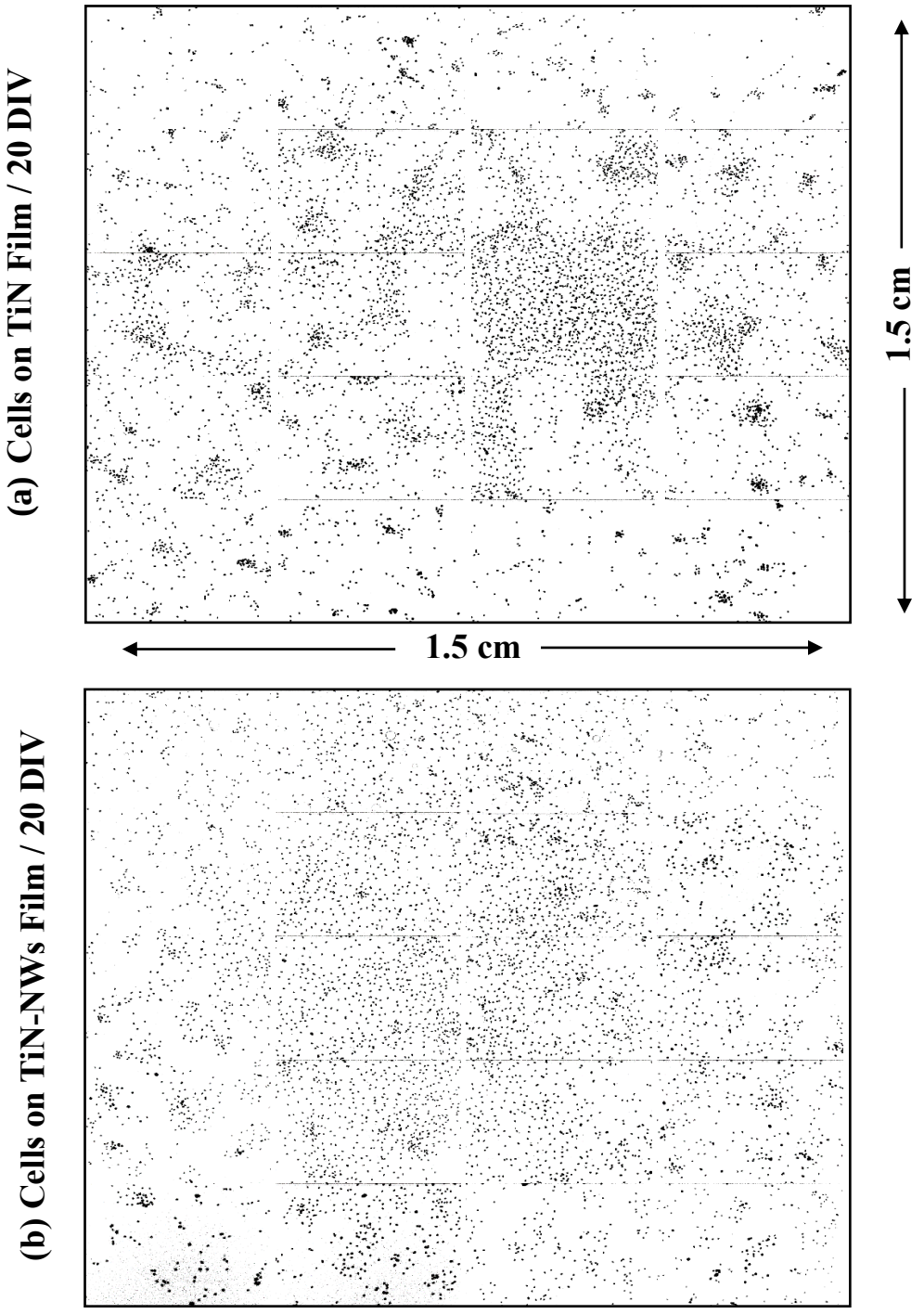

Figure 6.5: GBM cells nuclei stained with DAPI distributed across one sample of TiN-film and NWs substrate. Images were analysed with image J.

6.5 Summary

To examine the suitability of the synthesised TiN-NW as an electrode material, its biocompatibility was tested by culturing GBM cells *in vitro*. TiN film was also used for comparison with NWs to see the effect of surface structure on cells behaviour. Similar cellular behaviour in terms of nuclei's number, proliferation and adhesion over the period of 3, 10 and 20 DIV. A pronounce difference was observed on day 10 and 20 in terms of cell morphology where cells on thin film appeared to be flatter that cells on NWs, where they exhibited a 3D structure. In addition, although cells were outstretched on both substrates on day 20 but the degree of cells developing more pseudopodium on NWs surface were noticeable. Moreover, a significant difference in cell distribution between both substrate was detected. The distance between nuclei on NWs was twice the distance between nuclei on the thin film illustrating that NWs surface can allow those cultured cell to move around the surface and find an optimum spot to adhere on and further extend in morphology. Those results showed the improved biocompatibility of the synthesised TiN-NWs as compared to the TiN thin film and highlighted its potential as a neural-electrode material.

Chapter 7. Conclusion

The current state of stimulation and recording electrodes clearly shows substantial advances in material science development taking place over the last recent years. The development of material science in this regard included the optimisation of the electrode interface material with the biological target for the purpose of enhancing its electrochemical, mechanical performance and biocompatibility while reducing its size. TiN-NWs were suggested here as a potential neural electrode material providing, in particular, enhanced electrochemical properties and biocompatibility. TiN-NWs were synthesised here at a temperature of 600 °C, which is lower than the conventional fabrication of TiN-NWs. Lowering the manufacturing temperatures is always advantageous as it allows to expand the choice of substrates, and in particular the use of such interface material in flexible devices. The main outcomes of this work are summarised below.

7.1 Main outcomes emerged from this work

- Prior to the growth of TiN-NWs, TiN films were gown, through non-reactive RF magnetron sputtering with controlled polycrystalline and electrochemical properties, through the optimisation of RF power and Ar flow rate. XRD results showed that the preferred orientation of (111) can be obtained at a narrow window of process parameters, however, (111) plane could impart improved wear resistance to the electrode interface material. The electrochemical behaviour of TiN film, cycled under nitrogen ambient, showed good stability over 200 cycles with capacitance retention of 85%.
- TiO_2-NWs were grown on TiN/FTO substrate through hydrothermal growth method where the growth parameters were optimised towards high aspect ratio and polycrystalline structure. An aspect ratio of 23.1 and a preferred orientation along (002) plane was obtained at a synthesis conditions of 150°C for 18 hours on 200 nm TiN nucleation layer thickness. Having relatively high aspect ratio results in larger surface area, enhancing charge injection capacity, while polycrystalline structure can transduce electrical charge from the electrode surface to the tissue. It would be of advantage if the former and latter were varied to investigate their effect on the electrochemical properties. It could be a potential for future work.

- Nitridation of TiO_2-NWs through PECVD was implemented to convert the NWs into TiN-NWs at lower temperature than the conventional methods of nitridation. Nitridation process parameters were optimised through XPS and Raman by studying the effect of parameters on the material compositional and structural change. Varying the RF power was found to greatly affect the density of dissociated specious (NH^-_x) in the plasma. At an RF power of 150 W, ions in the plasma gained enough energy to cause etching of the surface, whereas lower RF power resulted in deposition of nitrogen atoms/ions needed for nitridation. The processing pressure, on the other hand, was found to vary N to Ti ratio and so the stoichiometry could be controlled. Nitridation time was optimised to one hour according to Ti-N peak area (in XPS) which was higher than that nitrided for less/more than an hour. Process parameters were, therefore, optimised towards achieving a larger peak area of Ti-N (illustrating better rate of nitridation), while Ti-O_2 peak are is reduced where possible. However, it is believed that by increasing the resolution of the process parameters a fully nitrided material can be achieved.
- Testing the electrochemical of the grown TiN-NWs and compare their properties to the grown TiN in film form, has highlighted the potential capability of TiN-NWs to be used as a neural electrode interface material. The capacitance of TiN-NWs was 5 times higher than that of the film, while their capacitance retention over 200 cycles was almost 99% under nitrogen electrolyte saturation and 92% under air ambient, showing higher stability than the film. Impedance of TiN-NWs at low frequency region, corresponding to ion diffusion, was lower than that of the film due to the nature of the nanostructure that allowed the diffusion of ions over time, although the diffusion was considered finite. TiN-NWs was found to be resistive to oxidation during cycling under air which was attributed to the restricted ion diffusion of the NWs hindered the diffusion of oxygen molecules.
- The biocompatibility test of TiN-NWs, on the other hand, showed superior difference to the TiN film in which the GBM cell distribution was 2 times higher than that on the TiN film, illustrating that NWs provide mobility to the cells and further extend in morphology.

The results in this work not only highlighted the potential capability of TiN-NWs to be used as neural-electrode interface material but have also highlighted the potential use of PECVD approach to nitride materials at lower temperatures.

7.2 References

[1] M. Vittorio and L. Martiradonna, Nanotechnology and neuroscience, 3rd ed., New York: Springer, 2014.

[2] P. Ambesh and D. Angeli, "Nanotechnology in neurology: Genesis, current status, and future prospects," *Ann Indian Acad Neurol,* vol. 18, no. 4, pp. 382-386, 2015.

[3] P. Fattahi, . G. Yang, . G. Kim and M. Reza Abidian, "A Review of Organic and Inorganic Biomaterials for Neural Interfaces," *Advance Material,* vol. 26, no. 12, pp. 1846-1885, 2015.

[4] U. Aregueta-Robles 1, A. Woolley, L. Poole-Warren, N. Lovell and R. Green, "Organic electrode coatings for next generation neural interfaces," *Frontiers in Neuroengineering,* vol. 7, pp. 1-18, 2014.

[5] C. Marrese , "Preparation of strongly adherent platinum black coatings," *Analytical Chemistry,* vol. 59, pp. 217-218, 1987.

[6] M. Abidian and D. Martin, "Experimental and theoretical characterization of implantable neural microelectrodes modified with conducting polymer nanotubes," *Biomaterials,* vol. 29, no. 9, pp. 1273-1283., 2008.

[7] S. Cogan, J. Ehrlich, T. Plante, A. Smirnov, D. Shire, M. Gingerich and R. Joseph, "Sputtered Iridium Oxide Films for Neural Stimulation Electrodes," *Biomedical Materials research part B: applied biomaterials,* vol. 89, no. 2, p. 353–361, 2009.

[8] M. Leber, M. Shandhi, A. Hogan, F. Solzbacher, R. Bhandari and S. Negi, "Different methods to alter surface morphology of high aspect ratio structures," *Applied Surface Science,* vol. 365, pp. 180-190, 2016.

[9] C. Patil Anoop and V. T. Nitish, "Implantable Neurotechnologies: A Review of Micro- And Nanoelectrodes for Neural Recording," *Med Biol Eng Comput,* vol. 54, no. 1, pp. 23-44, 2016.

[10] S. Tang, Y. Tang, Z. Liu and X. Meng, "Ultrasonic electrodeposition of silver nanoparticles on dielectric silica spheres," *Nanotechnology,* vol. 18, no. 29, p. 295607, 2007.

[11] N. Lawand, "Thin Titanium Nitride Films Deposited Using DC Magnetron Sputtering Used for Neural Stimulation and Sensing Purposes," *Procedia Engineering,* vol. 47, pp. 726-729, 2012.

[12] C. Boehler and S. T, "Nanostructured Platinum Grass Enables Superior Impedance reduction for Neural Microelectrodes," *Biomaterials,* vol. 67, pp. 346-353, 2015.

[13] J. Yang and D. Martin , "Impedance Spectroscopy And Nanoindentation Of Conducting Poly (3,4-Ethylenedioxythiophene) Coatings On Microfabricated Neural Prosthetic Devices," *Materials Research,* vol. 21, pp. 1124-1132, 2006.

[14] E. Castagnola and A. Ansaldo, "Smaller, softer, lower-impedance electrodes for human neuroprosthesis: a pragmatic approach," *Neuroenge,* vol. 7, no. 8, 2014.

[15] Y. Kim, H. Koo, M. Kim and S. Jung, "Iridium oxide on indium-tin oxide nanowires: An all metal oxide heterostructured multi-electrode array for neuronal interfacing," *Sensors & Actuators: B chemical ,* vol. 273, no. 2018, p. 718–725.

[16] T. Gabay and E. Jakobs, "Engineered self-organization of neural networks using carbon nanotubes clusters, statistical mechanics and its applications," *Physica A: Statistical Mechanics and its Applications,* vol. 350 , no. 6, pp. 611-621, 2005.

[17] M. Zukalova, J. Prochazka, Z. Bastl, J. Duchoslav, L. Rubacek, D. Havlicek and L. Kavan, "Facile Conversion of Electrospun TiO2 into Titanium Nitride/Oxynitride Fibers," *Material Chemistry ,* vol. 22, p. 4045–4055, 2010.

[18] S. Al-Thabaiti, R. Hahn, N. Liu, R. Kirchgeorg, S. So, P. Schmuki, S. Basahel and S. Bawaked, "NH3 treatment of TiO2 nanotubes: from N-doping to semimetallic conductivity," *Royal Scociety of Chemistry,* vol. 50, pp. 7960-7963, 2014.

[19] Y. Xie, Y. Wang and H. Du, "Electrochemical capacitance performance of titanium nitride nanoarray," *Materials Science and Engineering B,* vol. 178, p. 1443–1451, 2013.

[20] Y. Han, X. Yue, Y. Jin, X. Huang and P. Shen*, "Hydrogen evolution reaction in acidic media on single-crystalline titanium nitride nanowires as a non-noble metal electrocatalyst," *Material chemistry A,* vol. 4, no. 10, pp. 3673-7, 2016.

[21] G. Mangamma, P. Ajikumar, R. Nithya, T. Sairam, V. Mittal, M. Kamruddin, S. Dash and A. Tyagi, "Synthesis and gas phase nitridation of nanocrystalline TiO2," *Physics D: Applied physics,* vol. 40, p. 4597–4602, 2007.

[22] M. Patan, T. Shah and . M. Sahin, "Charge Injection Capacity of TiN Electrodes for an Extended Voltage Range," *Conference proceeding of IEEE Engineering in Medicine and Biology Society,* p. 890–892, 2006.

[23] A. Achour, R. Porto, M. Soussou, M. Islam, K. Boujtita, K. Aissa, L. Le Brizoual, A. Djouadi and T. Brousse, "Titanium nitride films for micro-supercapacitors: Effect of surface chemistry and film morphology on the capacitance," *Journal of Power source,* vol. 300, pp. 525-532, 2015.

[24] A. Scarano, "Bone Healing Around Titanium And Titanium Nitride-coated Dental Implants with Three Surfaces: An Experimental Study in Rats," *Clin Implant Dent Rel Res,* vol. 5.2, pp. 103-111, 2003.

[25] J.-D. Chang, "Future Bearing Surfaces In Total Hip Arthroplasty," *Clinics in Orthopedic Surgery,* vol. 6, pp. 110-106, 2014.

[26] Z. Xie, X. Liu, W. Wang, C. Liu, Z. Li and Z. Zhang, "Fabrication of Tin Nanostructure as a Hydrogen Peroxide Sensor by Oblique Angle Deposition," *Nanoscale Research Letters,* vol. 9, p. 105, 2014.

[27] B. Gray, A. Hector, M. Jura, J. Owen and J. Whittam, "Effect of oxidative surface treatments on charge storage at titanium nitride surfaces for supercapacitor applications," *Royal society of chemistry,* vol. 5, pp. 45-50, 2017.

[28] C. He´ber, J. Mazellier, E. Scorsone, M. Mermoux and P. Bergonzo, "Boosting the electrochemical properties of diamond electrodes using carbon nanotube scaffolds," *Carbon,* vol. 71, pp. 27-33, 2014.

[29] R. Normann, "Technology Insight: future neuroprosthetic therapies for disorders of the nervous system," *Nature Clinical Practice: Neurology,* vol. 3, no. 8, pp. 444-452, 2007.

[30] T. Kenny, The nuts and bolts of implantable device therapy: pacemakers, Chichester: John Wiley & Sons Inc, 1954.

[31] S. Waltzman and T. Roland, Cochlear implants, New York: Thieme, 2006.

[32] P. Plaha and S. Gill, "Bilateral deep brain stimulation of the pedunculopontine nucleus for Parkinson's disease," *NeuroReport,* vol. 16, no. 17, pp. 1883-1887, 2005.

[33] K. Woeppela, Q. Yang and X. Cui, "Recent advances in neural electrode–tissue interfaces," *Biomedical Engineering,* 2017.

[34] J. Barrese, N. Rao, K. Paroo, C. Triebwasser, C. Irwin, L. Franquemont and J. Donoghue, "Failure mode analysis of silicon-based intracortical microelectrode arrays in non-human primates," *Neural Engineering,* vol. 10, no. 6, p. 66014, 2013.

[35] A. Prasad, Q. Xue, R. Dieme, V. Sankar, R. Mayrand, T. Nishida, W. Streit and J. Sanchez, "Abiotic-biotic characterization of Pt/Ir microelectrode arrays in chronic implants," *Front Neuroengineering,* vol. 7, no. 2, pp. 1-15, 2014.

[36] A. Prasad, Q. Xue, V. Sankar, T. Nishida, G. Shaw, W. Streit and J. Sanchez, "Comprehensive characterization and failure modes of tungsten microwire arrays in chronic neural implants," *Neural Engineering,* vol. 9, no. 5, p. 056015, 2012.

[37] R. Barker and F. Cicchetti, Neuroanatomy and Neuroscience at a Glance, Cambridge: John Wiley & Sons, Incorporated, 2012.

[38] D. Merrill, M. Bikson and J. Jeffery, "Electrical stimulation of excitable tissue: design of efficacious and safe protocols," *Journal of Neuroscience Methods,* vol. 141, no. 2, pp. 171-198, 2005.

[39] N. Elgrishi, K. Rountree, B. McCarthy, E. Rountree, T. Eisenhart and J. Dempsey, "A Practical Beginner’s Guide to Cyclic Voltammetry," *Chemical Education,* vol. 95, pp. 197-206, 2018.

[40] D. Crow, Principles and Applications of Electrochemistry, London: Chapman & Hall, 1988.

[41] S. Oyoma, The Chemistry of Transition Metal Nitrides and Carbides, Glasgow: Blackie Academic, 1996.

[42] F. Nita, C. Mastail and G. Abadias, "Three-dimensional kinetic Monte Carlo simulations of cubic transition metal nitride thin film growth," *Physical reveiw B,* vol. 93, pp. 64-107, 2016.

[43] L. Fieandt, M. Fallqvist, T. Larsson, E. Lindahl and M. Boman, "Tribological properties of highly oriented Ti(C,N) deposited by chemical vapor deposition," *Tribology International ,* vol. 119, p. 593–599, 2018.

[44] J. Lim, H. Park, T. Park, J. Lee and J. Joo, "Mechanical properties of titanium nitride coatings deposited by inductively coupled plasma assisted direct current magnetron sputtering," *Vacuum Science and Technology A,* vol. 18, p. 524, 2000.

[45] D. Choi and P. Kumta, "Nanocrystalline TiN Derived by a Two-Step Halide Approach for Electrochemical Capacitors," *Electrochemical society,* vol. 153, no. 12, pp. 2298-2303, 2006.

[46] M. Rizz, A. Benedictis, G. Messina, R. Cordella, D. Marchesi, R. Messina, F. Penner, A. Franzini and C. Marras, "Comparative Analysis of Explanted DBS Electrodes," *Acta Neurochir,* vol. 157, pp. 2135-2141, 2015.

[47] M. Reichert William, Indwelling Neural Implants: Strategies for Contending with the In Vivo Environment, North Carolina: CRC Press, 2008.

[48] B. Morrison, K. Satman, D. Meaney and T. Mclntosh, "In Vitro Central Nervous System Models Of Mechanically Induced Trauma: A Review," *Neurotrauma,* vol. 15, no. 11, pp. 911-928, 1998.

[49] S. Baek, R. Green and L. Poole-Warren, "Effects of dopants on the biomechanical properties of conducting polymer films on platinum electrodes," *Biomedical Material Research A,* vol. 102, pp. 2743-52, 2014.

[50] L. Jeffery and Hendricks, Bioactive Conducting Polymer Coatings for Implantable Neural and Cochlear, Michigan: Proquest, Umi Dissertation Publishing, 2008.

[51] S. Baek, R. Green, A. Granville, P. Martens and L. Poole-Warren, "Thin film hydrophilic electro active polymer coatings for bioelectrodes," *Materials Chemistry B,* vol. 1, no. 13, pp. 3803-3810, 2013.

[52] X. Cui and D. Zhou, "Poly (3, 4-Ethylenedioxythiophene) for Chronic Neural Stimulation," *IEEE transactions on neural systems and rehabilitation engineering,* vol. 15, pp. 92-102, 2007.

[53] R. T. Hassarati, H. Marcal, L. John, R. Foster and R. Green, "Biofunctionalization of Conductive Hydrogel Coatings to Support Olfactory Ensheathing Cells at Implantable Electrode Interfaces," *Biomedical Materials Research Part B: Applied Biomaterials,* vol. 104, pp. 712-722, 2016.

[54] R. A. Green, P. Matteucci, R. Hassarati and B. Giraud,, "Performance of conducting polymer electrodes for stimulating neuroprosthetics," *Neural Engineering,* vol. 10, p. 016009, 2013.

[55] K. Wang, H. Fishman, H. Dai and J. Harris, "Neural Stimulation with a Carbon Nanotube Microelectrode Array," *American Chemical Society,* vol. 6, no. 9, p. 2043–2048, 2006.

[56] Norlin, J. Pan and C. Leygraf, "Investigation of Electrochemical Behavior of Stimulating/Sensing Materials for Pacemaker Electrode Application," *Electrochemical Society,* vol. 152, pp. 85-92, 2005.

[57] M. Humayun, J. Weiland a, G. Fujii, R. Greenberg, R. Williamson, J. Little, B. Mech, C. Cimmarusti, G. Boemel, G. Dagnelie and E. de Juan Jr, "Visual perception in a blind subject with a chronic microelectronic retinal prosthesis," *Vision research,* vol. 43, p. 2573–2581, 2003.

[58] D. Zhou and R. Greenberg, "Electrochemical Characterization of Titanium Nitride Microelectrode Arrays for Charge-Injection Applications," *Proceedings of the 2Sb Annual International Conference of the IEEE EMBS,* pp. 17-21, 2003.

[59] M. E. Null, "Temperature effects on the potential window of water and acetonitrile and heterogeneous electron transfer rates of outer sphere redox probes," Iowa Research Online, Iowa, 2014.

[60] N. Pour Aryan and K. Hans, Stimulation And Recording Electrodes For Neural Prostheses., New York: SpringerBriefs, 2016.

[61] S. Cogan, "Neural Stimulation and Recording Electrodes," *Annual Review of Biomedical Engineering,* vol. 10, pp. 275-309, 2008.

[62] A. Norlin, J. Pan and C. Leygraf, "Investigation of interfacial capacitance of Pt, Ti and TiN coated electrodes by electrochemical impedance spectroscopy," *Biomolecular Engineering,* vol. 19, pp. 67-71, 2002.

[63] J. Weltand, D. Anderson and M. Humayun, "In vitro electrical properties for iridium oxide versus titanium nitride stimulating electrodes.," *IEEE Trans Biomed Eng,* vol. 49, pp. 1574-9, 2002.

[64] R. Gerwig, K. Fuchsberger , B. Schroeppel, G. Link, G. Heusel, u. Kraushaar, w. Schuhmann, a. Stett and M. Stelzle, "PEDOT–CNT composite microelectrodes for recording and electrostimulation applications: fabrication, morphology, and electrical properties," *Fronties in neuroengineering,* 2012.

[65] T. Nyberg, A. Shimada and K. Torimitsu, "Ion conducting polymer microelectrodes for interfacing with neural networks," *Neuroscience Methods,* vol. 160, pp. 16 - 25, 2007.

[66] M. K. Patan, "Titanium nitride as an electrode material for high charge density application," India, 2007.

[67] N. Kumar and S. Kumbhat, Essentials in Nanoscience & Nanotechnology, Canada: Jhon Wiley & Sons., 2016.

[68] D. Depla, S. Mahieu and J. Greene, "Sputter deposition processes," Ghent Univeristy , Belgium, 2008.

[69] M. Petrich, "Creating amorphous films," *Chemtech,* vol. 12, pp. 740-745, 1989.

[70] R. Cross, "Low temperature (<150 C) hydrogenated amorphous silicon grown by PECVD source gas heating," Thesis, UK, March 2005.

[71] S. Droes, T. Kodas and M. Hampden-Smith, "Plasma enhanced chemical vapor deposition (PECVD)," in *Carbide, Nitride and Boride Materials Synthesis and Processing; PECVD*, London, Chapman & Hall, 1997, pp. 579-600.

[72] H. Xiao, Introduction to semiconductor technology, Bellingham: Society of Photo-Optical Instrumentation Engineers (SPIE), 2012.

[73] J. Buha, "Nonaqueous Syntheses of Metal Oxide and Metal Nitride Nanoparticles," Max-Planck Institut, Postdam, 2008.

[74] Bae and H. Chang, "Sol–Gel Synthesis Of Sub-50Nm Zno Nanowires On Pulse Laser Deposited Zno Thin Films," *Applied Surface Science ,* vol. 253, pp. 1758-1761, 2006.

[75] N. Sharipah, H. Uda and A. Tijjani, "Hydrothermal Growth of Titanium Dioxide Nanowires on Different Seed," *2014 Fifth International Conference on Intelligent Systems, Modelling and Simulation,* pp. 159-162, 2014.

[76] Z. Wei, R. Li, T. Huang and A. Yy, "Fabrication of morphology controllable rutile TiO2 nanowire arrays by solvothermal route for dye-sensitized solar cells," *Electrochimica Acta,* vol. 56, no. 22, pp. 7696-7702, 2011.

[77] G. Cao and D. Liu, "Template-based synthesis of nanorod, nanowire, and nanotube arrays," *Advances in Colloid and Interface Science,* vol. 136, no. 1-2, pp. 45-64, 2008.

[78] J. Yahiro, Y. Oaki and H. Imai, "Biomimetic Synthesis of Wurtzite ZnO Nanowires Possessing a Mosaic Structure," *Small,* vol. 2, no. 10, pp. 1183-1187, 2006.

[79] B. Feuerbacher, "Phase Formation Metastable solidification of metals," *Materials science reports,* vol. 4, pp. 1-40, 1989.

[80] A. Kempen, "Solid State Phase Transformation Kinetics," Universität Stuttgart, PhD thesis., 2001.

[81] J. Kar, S. Das, S. Lee, M. Ham, J. Choi and J. Myoung, "Surface Modification of hydrothermally grown ZnO nanostructures with process parameteres," *Chemical Engineering Communications,* vol. 196, no. 9, pp. 1130-1138, 2014.

[82] A. Rahm, M. Lorenz, T. Nobis, G. Zimmermann, M. Grundmann, B. Fuhrmann and F. Syrowatka, "Pulsed-laser deposition and characterization of ZnO nanowires with regular lateral arrangement," *Applied Phyiscs A: Materials Science & Processing,* vol. 88, pp. 31-34, 2007.

[83] L. Zhigilei, "Nucleation and growth kinetics," 2010. [Online]. Available: http://people.virginia.edu/~lz2n/mse305/notes/Nucleation.pdf. [Accessed 12 11 2017].

[84] S. Puttaswamy, Q. Shi, A. Bandla, S. Kim, N. Thakor and C. Lee, "Nanowire Electrodes Integrated on Tip of Microwire for Peripheral Nerve Stimulation," *Microelectromechanical systems,* vol. 26, no. 4, pp. 1057-7157, 2016.

[85] G. Kim, K. Kim, E. Lee, T. An, W. Choi, G. Lim and J. Shin, "Recent Progress on Microelectrodes in Neural Interfaces," *Materials (Basel),* vol. 11, no. 10, 2018.

[86] J. Ferguson, C. Boldt, J. Puhl, T. Stigen, J. Jackson, K. Crisp, K. Mesce, T. Netoff and A. Redish, "Nanowires precisely grown on the ends of microwire electrodes permit the recording of intracellular action potentials within deeper neural structures," *Nanomedicine,* vol. 7, no. 6, pp. 847-853, 2012.

[87] B. Motlagh, M. Choueib, A. Mesgar, M. Hasanuzzaman and M. Sawan, "Direct Growth of Carbon Nanotubes on New High-Density 3D Pyramid-Shaped

Microelectrode Arrays for Brain-Machine Interfaces," *Micromachines,* vol. 7, no. 9, p. 163, 2016.

[88] A. Mercanzini, K. Cheung, D. Buhl, M. Boers, A. Maillard, P. Colin, J. Bensadoun, A. Bertsch and P. Renaud, "Demonstration of cortical recording using novel flexible polymer neural probes," *Sensors and Actuators A: Physical,* vol. 143, no. 1, pp. 90-96, 2008.

[89] V. Castagnola, "Implantable microelectrodes on soft substrate with nanostructured active surface for stimulation and recording of brain activities," Micro and nanotechnologies/Microelectronics. University of Toulouse III Paul Sabatier, Toulouse , 2014.

[90] D. Schroder, Semiconductor material and device characterization, Canada: Wilsy Interscience, 2006.

[91] N. Singh, "Investigation on transport properties and structural characterization of some nanomaterials for fabrication of hybrid supercapacitors," Chhattisgarh Swami Vivekanand Technical University , India, Thesis report, 2014.

[92] D. Vollath, Nanomaterials: an introduction to synthesis, properties and applications, Germany: Wiley-VCH, 2013.

[93] S. Nazarpour, Thin Films and Coatings in Biology, vol. 1, Springer, 2013, pp. 310-312.

[94] Chemistry LibreTexts, "Electrolysis of Water," Chemistry LibreTexts, 3 June 2019. [Online]. Available:

https://chem.libretexts.org/Under_Construction/Purgatory/Core_Construction/Chemistry_30/Electrochemistry/3.3_Electrolysis_of_Water. [Accessed 10 June 2019].

[95] A. Zia and C. Mukhopadhyay, Electrochemical Sensing: Carcinogens in Beverages, Switzerland: Springer, 2016.

[96] M. Orazem and B. Tribollet, Eletrochemical Impedance Spectroscopy, Canada: John Wiley & Sons, Inc, 2008.

[97] V. Kumar, N. Sharma and S. Maitra, "In vitro and in vivo toxicity assessment of nanoparticles," *International Nano Letters,* vol. 7, pp. 243-256, 2017.

[98] M. Govers and J. Brown, "Study of titanium–nitrogen films deposited in an electron beam evaporation unit," *Vacuum science & Technology,* vol. 13, no. 5, pp. 2328-2335, 1995.

[99] R. Krishnan, R. Ramaseshan, T. Mathews, R. Nithya, S. Dash, A. Tyagi and B. Raj, "Synthesis of nanostructured titanium nitride films by PLD through reactive processing," *Surface Engineering,* vol. 25, no. 3, pp. 218-222, 2009.

[100] Y. Krockenberger, S. Karimoto, H. Yamamoto and K. Semba, "Coherent growth of superconducting TiN thin films by plasma enhanced molecular beam epitaxy," *Applied Physics,* vol. 112, pp. 83-92, 2012.

[101] H. Kim and J. Park, "Effects of nitrogen flow rate on titanium nitride films deposition by DC facing target sputtering method," *Korean Journal of Chemical Engineering,* vol. 29, no. 5, pp. 676-679, 2012.

[102] R. Sait and R. Cross, "Synthesis and characterization of sputtered titanium nitride as a nucleation layer for novel neural electrode coatings," *Applied surface science,* vol. 424, pp. 290-298, 2017.

[103] S. Ju, C. Weng, J. Chang and C. Hwang, "A molecular dynamics study of deposition rate dependence of film morphology in the sputtering process," *Surface and Coatings Technology,* vol. 149, no. 2, pp. 135-142, 2002.

[104] K. Chan and B. Teo, "Sputtering power and deposition pressure effects on the electrical and structural properties of copper thin films," *Journal of Materials Science,* vol. 40, no. 22, pp. 5971-5981, 2005.

[105] N. Marechal, E. Quesnel and Y. Pauleau, "Silver thin films deposited by magnetron sputtering," *Thin Solid Films,* vol. 241, no. 1-2, pp. 34-38, 1994.

[106] M. Le, y. Sohn, J. Lim and G. Choi, "Effect of Sputtering Power on the Nucleation and Growth of Cu Films Deposited by Magnetron Sputtering," *MATERIALS TRANSACTIONS,* vol. 51, no. 1, pp. 116-122, 2010.

[107] X. Pang, L. Zhang, H. Yang, K. Gao and A. Volinsky, "Residual Stress and Surface Energy of Sputtered TiN Films," *Materi Eng and Perform,* vol. 24, no. 3, pp. 1185-1191, 2015.

[108] B. Avasarala and P. Haldar, "Electrochemical oxidation behavior of titanium nitride based electrocatalysts under PEM fuel cell conditions," *Electrochimica Acta,* vol. 55, no. 28, pp. 9024-9034, 2010.

[109] U. C. Oh and Jung Ho Je, "Effects of strain energy on the preferred orientation of TiN thin films," *Applied physics,* vol. 74, pp. 1692-1696, 1993.

[110] J. Zhao, X. Wang, Z. Chen, S. Yang, T. Shi and X. Liu, "Overall energy model for preferred growth of TiN films during filtered arc deposition," *Journal of physics D: Applied physics,* vol. 30, no. 5, 1997.

[111] X. Chen and C. Burda, "Photoelectron Spectroscopic Investigation of Nitrogen-Doped Titania Nanoparticles," *physics chemistry,* vol. 108, pp. 15446-15449, 2004.

[112] J. Yoo, H. Yoo, J. H, K. H, S. Bang, J. Choia and H. Suh, "Titanium oxynitride microspheres with the rock-salt structure for visible-light photocatalysts," *Materials chemistry A,* no. 3, pp. 869-876, 2015.

[113] E. Filatova, A. Konashuk, S. Sakhonenkov, A. Sokolov and V. Afanas'ev, "Re-distribution of oxygen at the interface between γ-Al2O3 and TiN," *Physics Chemistry C,* vol. 119, p. 20755–20761, 2017.

[114] G. Greczynski, and L. Hultman, "In-situ observation of self-cleansing phenomena during ultra-high vacuum anneal of transition metal nitride thin films: Prospects for non-destructive photoelectron spectroscopy," *Applied Physices Letter,* vol. 109, no. 21, p. 211602, 2016.

[115] S. Meija, "Electrochemical Properties of Titanium Nitride Nerve Stimulation Electrodes: An In Vitro and In Vivo Study," *Front Neuroscience,* vol. 9, no. 268, pp. 1-11, 2015.

[116] V. Chawla, R. Jayaganthan, A. Chawla and R. Chandra, "Microstructural characterizations of magnetron sputtered Ti films on glass substrate," *Materials Processing Technology,* vol. 209, no. 7, pp. 3444-3451, 2009.

[117] T. Kwon, K. Kim, S. Park, A. Annamalia and M. Lee, "[15]T. Kwon, K. Kim, S. Park, A. Annamalai and M. Lee, "Effect of seed particle size and ammonia concentration on the growth of ZnO nanowire arrays and their photoconversion efficiency",

International Journal of Nanotechnology, vol. 10, no. 89, p. 68," *International journal of Nanotechnology,* vol. 10, no. 89, p. 681, 2013.

[118] H. Du and Y. Xie, "Electrochemical capacitance of polypyrrole–titanium nitride and polypyrrole–titania nanotube hybrids," *New Journal of Chemistry,* vol. 38, no. 3, p. 1284, 2014.

[119] M. Aliofkhazraei, N. Ali, W. Mile, C. Ozkan, S. Mitura and J. Gervasoni, Graphene science handbook, New York: CRC Press , 2016.

[120] A. Morel, Y. Piron, R. Porto, T. Brousse and D. B´elan, "Suitable Conditions for the Use of Vanadium Nitride as an Electrode for Electrochemical Capacitor," *Electrochemical society,* vol. 163, no. 6, pp. 1077-1082, 2016.

[121] A. Achour, M. Chaker, H. Achour, A. Arman, M. Islam, M. Mardani, m. Boujtita, L. Brizoual, M. Djouadi and T. Brousse, "Role of nitrogen doping at the surface of titanium nitride thin films towards capacitive charge storage enhancement," *Power sources,* vol. 359, pp. 349-354, 2017.

[122] B. Siemensmeyer, K. Bade and J. Schultze, "XPS and Electrochemical Studies of Thin TiN Layers," *Physics chemistry,* vol. 11, no. 95, pp. 1461-1469, 1991.

[123] R. Sait, S. Govindarajan and R. Cross, "Nitridation of optimised TiO2 nanorods through PECVD towards neural electrode application," *Materialia,* vol. 4, pp. 127-138, 2018.

[124] S. Venkatachalam, H. Hayashi, T. Ebina and H. Nanjo, "Preparation and Characterization of Nanostructured TiO2 Thin Films by Hydrothermal and Anodization Methods," *Optoelectronics - Advanced Materials and Devices, InTech,* pp. 115-133, 2013.

[125] G. Lawrence, A. V. Baskar, M. El-Newehy and W. Cha, "Quick high-temperature hydrothermal synthesis of mesoporous materials with 3D cubic structure for the adsorption of lysozyme," *Science and Technology of Advanced Materials,* vol. 16, pp. 1-11, 2015.

[126] T. A. N. Peiris, H. Alessa, J. Sagu, I. Bhatti, P. Isherwood and K. G. U. Wijayantha, "Effect of ZnO seed layer thickness on hierarchical ZnO nanorod growth on flexible substrates for application in dye-sensitised solar cells," *J Nanopart Res,* vol. 15, p. 2115, 2013.

[127] C. Y. Kunga, S. L. Young, M. C. Kao, . H. Z. Chen, . J. H. Linc, . H. H. Lin, L. H. Horng and Y. T. Shih, "Thickness Effect of Sputtered ZnO Seed Layer on the Electrical Properties of Li-doped ZnO Nanorods and Application on the UV Photodetector," *Proceedings of the 2013 IEEE 5th International Conference,* pp. 417-420, 2013.

[128] B. Liu and E. Aydil, "Growth of Oriented Single-Crystalline Rutile TiO2 Nanorods on Transparent Conducting Substrates for Dye-Sensitized Solar Cells," *The American Chemical Society,* vol. 131, pp. 3985-3990, 2008.

[129] M. Yusoff, M. Mamat, M. Malek, A. Ismail and S. Saidi, "Fabrication of Titanium Dioxide Nanorod Arrays-Based UV Photosensor From Low-Concentration of Titanium (IV) Butoxide with Hydrochloric Acid," *IEEE Student Conference on Research and Development (SCOReD),* 2016.

[130] M. Yusoff, M. Mamat, M. Malek, A. Suriani, A. Mohamed, M. Ahmad, S. Alrokayan, H. Khan and M. Rusop, "Growth of titanium dioxide nanorod arrays through the aqueous chemical route under a novel and facile low-cost method," *Materials Letters,* vol. 164, pp. 294-298, 2016.

[131] Y. Lu, Y. Tseng, J. Lee and W. Lee, "lateral-to-vertical growth transition of tio2 nanorods grown on FTO-glass substrate by hydrothermal method," *Nanomaterials and Biostrucutres,* vol. 11, no. 2, pp. 507-515, 2016.

[132] Z. Li, J. Song and G. Mantin, "Quantifying the Traction Force of a Single Cell by Aligned Silicon Nanowire Array," *Nano Letters,* vol. 9, no. 10, pp. 3575-3580, 2009.

[133] W. J and B. Li, "Application of cell traction force microscopy for cell biology research," *Methods in Molecular Biology,* vol. 10, p. 586, 2009.

[134] L. Gallentoft, L. Pettersson, N. Danielsen, J. Schouenborg, C. Prinz and . C. Linsmeier , "Size-dependent long-term tissue response to biostable nanowires in the brain," *Biomaterials,* vol. 42, pp. 172-183, 2015.

[135] S. Bidier, . M. R. Hashim, A. AL-Diabat and M. Bououdina, "Effect of growth time on Ti-doped ZnO nanorods prepared by low-temperature chemical bath deposition," *Physica E: Low-dimensional Systems and Nanostructures,* vol. 88, pp. 169-173, 2017.

[136] J. Hao, T. Xu and W. Liu, "Effect of deposition pressure on microstructure and properties of hydrogenated carbon nitride films prepared by DC-RF-PECVD," *Non-crystalline solids,* vol. 351, pp. 3671-3676, 2005.

[137] J. Jauberteau, I. Jauberteau and J. Aubreton, "NH3 and NHx<3 radicals synthesis downstream a microwave discharge sustained in an Ar–N2–H2 gas mixture. Study of surface reactive processes and determination of rate constants," *Physics D: Applied physics,* vol. 35, p. 665–674, 2002.

[138] J. Houmes and H. Loye, "Plasma Nitridation of Metal Oxides," *Chemistry Material,* vol. 8, pp. 2551-2553, 1996.

[139] D. Douglass, S. B and S. M, "The kinetics and mechanism of the conversion of titanium dioxide to titanium nitride," Ohio State University , Ohio, Thesis, 1958.

[140] R. Aghababazadeh, A. Mirhabibi, B. Rand, S. Banijamali , J. Pourasad and M. Ghahari, "Synthesis and characterization of nanocrystalline titanium nitride powder from rutile and anatase as precursors," *Surface science,* vol. 601, p. 2881–2885, 2007.

[141] I. Morozov, O. Belousova, O. Belyakov, L. Parkinc, S. Sathasivam and M. Kuznetcov, "Titanium nitride room-temperature ferromagnetic nanoparticles," *Alloys and Compounds,* vol. 675, pp. 266-276, 2016.

[142] Y. Loraine, . L. Arnaud, R. Stéphanie, B. Joëlle, Z. Mirvat and R. Vincent, "Optimization of N-doped TiO2 multifunctional thin layers by low frequency PECVD process," *European Ceramic Society,* vol. 37, no. 16, pp. 5289-5303, 2017.

[143] P. Romero-Gómez, V. Rico, J. Espinós, . A. R. González-Elipe, R. Palgrave and R. Egdell , "Nitridation of nanocrystalline TiO2 thin films by treatment with ammonia," *Thin Solid films,* vol. 519, p. 3587–3595, 2011.

[144] Z. Zhang, . J. Goodall, . D. Morgan, . S. Brown, . R. Clark, J. Knowles, ,. N. Mordan , J. R. Evans, A. Carley, M. Bowker and J. Darr, "Photocatalytic activities of N-doped nano-titanias and titanium nitride," *the European Ceramic Society,* vol. 29, p. 2343–2353, 2009.

[145] J. Lynch, C. Giannini, J. Cooper, A. Loiudice, I. Sharp and R. Buonsanti, "Substitutional or Interstitial Site-Selective Nitrogen Doping in TiO2 Nanostructures," *Physical Chemistry,* vol. 119, no. 13, p. 7443–7452, 2015.

[146] D. Jaeger and J. Patscheider, "A complete and self-consistent evaluation of XPS spectra of TiN," *Electron Spectroscopy and Related Phenomena,* vol. 185, p. 523–534, 2012.

[147] Z. XU and F. Xiong, "Plasma Nitriding," Plasma surface Mettalurgy, 2017.

[148] I. Berti, M. Mohai, J. Sullivan and S. Saied, "Surface characterisation of plasma-nitrided titanium: an XPS study," *Applied surface science,* vol. 84, pp. 357-371, 1995.

[149] H. Shi, H. Zhang, Z. Chen, T. Wang, L. Wang, W. Zenga, G. Zhang and H. Duan, "Synthesis of TiN nanostructures by Mg-assisted nitriding TiO2 in N2 for lithium ion storage," *Chemical Engineering,* vol. 336, pp. 12-19, 2018.

[150] D. Guan, J. Li, X. Gao and C. Yuan, "Effects of amorphous and crystalline MoO3 coatings on the Li-ion insertion behavior of a TiO2 nanotube anode for lithium ion batteries," *RSC advances,* vol. 4, p. 4055–4062 | , 2014.

[151] J. Kang, "Fabrication and characterization of nano carbon based electrochemical double-layer capacitors," University of Waterloo, Canada, 2015.

[152] A. Bolz, R. Frohlich, K. Schmidt and M. Schaldach, "Effect of smooth, porous and fractal surface structure on the properties of an inteface," *Material science: Materilas in Medicine ,* vol. 6, pp. 844-848, 1995.

[153] G. Cai, X. Wang, D. Zhou, J. Zhang, Q. Xiong, C. Gu and J. Tu, "Hierarchical structure Ti-doped WO3 film with improved electrochromism in visible-infrared region," *Royal Society of Chemistry Advances,* no. 19, 2013.

[154] H. Xia, Y. Wang, J. Lin and L. Lu, "Hydrothermal synthesis of MnO2/CNT nanocomposite with a CNT core/porous MnO2 sheath hierarchy architecture for supercapacitors," *Nanoscale research letters,* vol. 7, no. 33, pp. 1-10, 2012.

Germany Instruemnt, "Basics of Electrochemical Impedance Spectroscopy," 2005.
155] [Online]. Available: https://www.gamry.com/application-notes/EIS/basics-of-electrochemical-impedance-spectroscopy/. [Accessed 30 09 2018].

R. Farma, M. Deraman, I. Talib, R. Omar, J. Manjunatha, M. Ishak, N. Basri and B.
156] Dolah, "Physical and Electrochemical Properties of Supercapacitor Electrodes Derived from Carbon Nanotube and Biomass Carbon," *International journal of Electrochemical Science,* vol. 8, pp. 257-273, 2013.

. R. G. Compton and C. E. Banks, Understanding Voltammetry - second edition,
157] Oxford: Imperical College Press, 2011.

H. Cesiulis, N. Tsyntsaru, A. Ramanavicius and G. Ragoisha, "The Study of Thin
158] Films by electrochemical impedance spectroscopy Nanostructures and Thin Films for Multifunctional Applications," Switzerland, Springer, 2016.

A. Meland, D. Bedeaux and S. Kjelstrup, "A Gerischer Phase Element in the
159] Impedance Diagram of the Polymer Electrolyte Membrane Fuel Cell Anode," *Physical chemistry B,* vol. 109, pp. 21380-21388, 2005.

J. Bisquert, "Theory of the Impedance of Electron Diffusion and Recombination in a
160] Thin Layer," *Physical Chemistry,* vol. 106, pp. 325-333, 2002.

J. Nielsen and J. Hjelm, "Impedance of SOFC electrodes: A review and a
161] comprehensive case study on the impedance of LSM:YSZ cathodes," *Electrochimica Acta,* vol. 115, pp. 31-45, 2014.

BioLogic Science Instruments, "EC-Lab Softweare user's Manual; BT-Lab & EC-Lab
162] Data Analysis and Processes," Biologic schenice instruments, 2015.

[163] S. Erol, "Electrochemical impedance spectroscopy analysis and modeling of lithium cobalt oxide/carbon batteries," University of Florida, Florida, 2015.

[164] S. Park, J. Park, S. Sim, M. Sung, K. Kim, B. Hong and S. Hong, "Enhanced Differentiation of Human Neural Stem Cells into Neurons on Graphene," *Advanced Healthcare Materials,* vol. 23, pp. 263-267, 2011.

[165] G. Piret, M. T. Perez and C. N. Prinz, "Neurite outgrowth and synaptophysin expression of postnatal CNS neurons on GaP nanowire arrays in long-term retinal cell culture," *Biomaterials,* vol. 34, pp. 875-887, 2013.

[166] T. Berthing, S. Bonde, C. B. Sorensen, P. Utko, J. Nygard and K. L. Martinez, "Intact mammalian cell function on semiconductor nanowire arrays: new perspectives for cell-based biosensing," *new perspectives for,* vol. 7, pp. 640-647, 2011.

[167] W. Hallstrom, T. Mårtensson, C. Prinz, P. Gustavsson, L. Montelius, L. Samuelson and M. Kanje, "Gallium phosphide nanowires as a substrate for cultured neurons," *Nano letter,* vol. 7, pp. 2960-2965, 2007.

[168] G. Piret, M. T. Prinz and C. N. Prinz, "Substrate porosity induces phenotypic alterations in retinal cells cultured on silicon nanowires," *RSC Advances,* vol. 4, pp. 27888-97, 2014.

[169] L. Cyster, K. Parker, T. Parker and D. Grant, "The effect of surface chemistry and nanotopography of titanium nitride (TiN) films on primary hippocampal neurones," *Biomaterials,* vol. 25, no. 1, pp. 97-107, 2004.

[170] L. Duta, G. Stan, A. C. Popa, M. Husanu, S. Moga, M. Socol, I. Zgura, F. Miculescu, I. Urzica, A. Popescu and I. Mihailescu, "Thickness Influence on In Vitro Biocompatibility of Titanium Nitride Thin Films Synthesized by Pulsed Laser Deposition," *Materials,* vol. 9, no. 38, 2016.

[171] Y. Tamura, A. Yokoyama and F. Watari, "Surface Properties and Biocompatibility of Nitrided Titanium for Abrasion Resistant Implant Materials," *Dental Materials,* vol. 21, no. 4, pp. 355-372, 2002.

[172] I. Khan, S. Baeesa, M. Bangash, H. Schulten, F. Alghamdi, H. Qashqari, N. Madkhali, A. Carracedo, M. Saka, A. Jamal, J. Al-Maghrabi, M. AlQahtani3, S. Al-Karim, G. Damanhouri1, K. Saini, A. Chaudhary3, A. Abuzenadah and D. Hussein, "Pleomorphism and drug resistant cancer stem cells are characteristic of aggressive primary meningioma cell lines," *Cancer Cell International ,* vol. 17, no. 72, p. 441, 2017.

[173] S. Hagvall, C. Choi, J. Dunn, S. Heydarkhan, K. Layland, W. Maclellan and R. Beygui, "Influence of Systematically Varied Nano-Scale Topography on Cell Morphology and Adhesion," *Cell Communication and Adhesion,* vol. 14, p. 181–194, 2007.

[174] I. Chung, C. W. Li and G. J. Wang, "The influence of different nanostructured scaffolds on fibroblast growth," *Science technology advance material,* vol. 14, no. 4, p. 044401, 2013.

[175] L. Andolfi, M. Murello, D. Cassese, J. Ban, S. D. Zilio and M. Lazzarino, "High aspect ratio silicon nanowires control fibroblast adhesion and cytoskeleton organization," *Nanotechnology,* vol. 28, no. 15, p. 155102, 2017.

[176] S. Bonde, T. Berthing, M. Madsen, T. Andersen, Buch-Månson, L. Guo, X. Li, F. Badique, K. Anselme, J. Nygård and K. Martinez, "Tuning InAs nanowire density for HEK293 cell viability, adhesion, and morphology: Perspectives for nanowire-based biosensors," *ACS Applied material % interfaces,* vol. 5, pp. 10510-10519, 2013.

[177] J. Diard, L. Gorrec and C. Montella, "Hnadbook of Electrochemical Impedance Spectroscopy: Diffusion Impedances," Bio-Logic, Montella, 2017.

7.3 Future work

Further optimisation of the nitridation process to fully convert the oxide into nitride would be one of the future work of this research. A fully nitrided material could impart further improvement to the electrochemical performance, in particularly, the electrochemical stability. In addition, there are few areas in this research that can be done to further optimise the material properties. For example, studying the effect of TiN-NWs density, aspect ratio, crystal orientation on the electrochemical behaviour of the material which could bring further improvement to the neural-electrode interface.

This work has tested the cycling stability of TiN film and NWs through cycling over 200 cycles (2 hours period) as an initial electrochemical test. However, Since electrodes are used chronically or at least for 5 to 10 years, further cycling test can be done by increasing the number of CV cycles, and study the oxidation behaviour of the electrode if any.

A one significant future work is to study the behaviour of cultured neurons in vitro on the synthesised TiN-NWs and compare their behaviour to that on TiN films. Glioblastomas are cancerous cells in which they might be behaving differently from neuron cells. Neuron cells behaviour have not been studied previously on TiN nanostructure and so this could be a significant future work. The biocompatibility of TiN-NWs can be studied more in details by studying the effect of surface composition and NWs densities on the viability of cells. The viability of cells can be tested using the 3-(4, 5-dimethylthiazolyl-2)-2,5-diphenyltetrazolium bromide (MTT) colorimetric assay. In addition, since cells prefer hydrophobic surfaces, it would be worth doing a contact angle measurement to better understand cells adhesion and behaviour.

A next major step of the work is test the ability of the nanowires to deliver charges to a cultured-neural cell *in vivo* and measure the neural response (action potential propagation) by electrophysiological tool, such as patch clamp. Since the electrochemical properties of implanted electrodes significantly differ from those electrodes in inorganic saline, e.g. the smaller charge injection *in vivo* compared to *in vitro*, it would be of an importance to test the electrochemical behaviour of TiN-NWs *in vivo,* as a future work.

7.4 Appendix

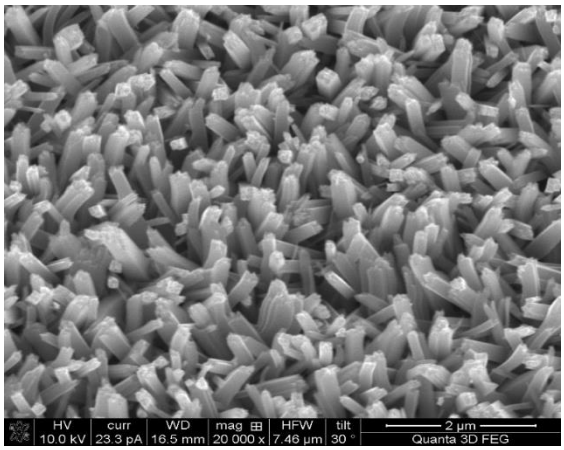

Figure B1: SEM image of TiO_2-NWs after nitridation (R_{12}) showing no morphological change.

Table A1: experimental runs done towards PECVD parameters optimisation.

Runs	**Temperature (°C)**	**Power (Watt)**	**Time (hours)**	**Pressure (mTorr)**
11	600	50	2	500
12	600	100	1	500
13	600	100	0.5	500
14	600	100	3	500
15	600	150	1	500
16	600	100	1	900
17	600	100	1	1400
18	600	100	1.5	500
19	600	100	1	300
20	750	100	1	500